A numerical model for aeolian sand transport and the concatenated dust emission

Inaugural-Dissertation
zur
Erlangung des Doktorgrades
Dr. rer. nat.
der Mathematisch-Naturwissenschaftlichen Fakultät
der Universität zu Köln

vorgelegt von
Sandesh Haleangady Kamath
aus Mangaluru, Indien

Köln | 2024

Berichterstatter:	Prof. Dr. Yaping Shao (Universität zu Köln) Prof. Dr. Gerhard Wurm (Universität Duisburg-Essen) Dr. Eric J. R. Parteli (Universität Duisburg-Essen)
Tag der mündlichen Prüfung:	28.10.2024

Abstract

Dust is emitted, transported and deposited throughout the year, mainly from the vast sand seas on Earth affecting the weather, climate ecosystems and other cycles of the biosphere. It influences the various feedback mechanisms, and causes the largest uncertainties in the future climate projections. A particle-based 3D numerical model to study the dust aerosol emission is presented in this work. The model was validated using the well characterized sand saltation process which is one of the major mechanisms through which dust is entrained.

Using a scalable Discrete Element Method (DEM) model, which is coupled with the fluid dynamics of the turbulent wind, we confirm the existence of a quadratic scaling for the sand mass flux Q with the wind friction velocity u_*. The impact threshold (minimal u_* for sustained transport) and fluid threshold (minimal u_* for grain entrainment) values for $d = 200$ μm sand grains which are key parameters in examining the grain initiation were found to be $u_{*,\mathrm{it}} \approx 0.165$ m/s and $u_{*,\mathrm{ft}} \approx 0.27$ m/s. Previous numerical studies never considered the sparsely-covered soils, and thus we developed a scheme to characterize this problem of low-sand availability and showed that $Q = a \cdot [1 + b \cdot (u_*/u_{*,\mathrm{it}} - 1)] \cdot \sqrt{d/g} \cdot \rho_\mathrm{a} \cdot \left(u_*^2 - u_{*,\mathrm{it}}^2\right)$, where, d is particle size, g is gravity and ρ_a is air density, while $u_{*,\mathrm{it}}$ and the empirical parameters a and b depend on the sand cover thickness. Thus we observe a transition from the quadratic scaling in the conventional erodible cases ($b = 0$), to a cubic scaling over rigid surfaces. The universality of the model was also tested for varying fluid conditions, due to the comprehensive depiction of the viscous

layer close to the bed surface.
To simulate mixed sand-dust systems, the model was extended by including the crucial aspect of cohesion, which is modeled using the van der Waals interaction. The rolling resistance, lift force, as well as the stochastic turbulent fluctuations provided the means to verify the grain-size dependency in monodisperse systems on $u_{*,\mathrm{ft}}$ which reaffirms the Shao and Lu [2000] equation, $u_{*,\mathrm{ft}} \propto \sqrt{(\sigma_\mathrm{p} gd + \gamma_\mathrm{s}/\left(gd\right))}$. Here σ_p is the grain-to-fluid density ratio, γ_s is the parameter describing the strength of cohesive forces (surface energy density in our model). The stochastic nature of cohesion [Shao and Klose, 2016] further lowers the threshold values in the presence of turbulent fluctuations, thus stressing on the need to include it in future models. The direct numerical simulations for the first time allow to study the dust emission mechanisms - direct entrainment, saltation bombardment and aggregate disintegration at the micro-scale, as the grain clusters which form and break is captured. In bi-disperse sand-dust beds $d_{10}d_{200}$ (10 μm grains dispersed over 200 μm sand grains), under limited supply of dust, we observe the lowering of fluid thresholds as a result of direct aerodynamic entrainment at nominal wind speeds below the saltation threshold. This is due to the fact that, the dust grains, unlike in a monodiperse system are exposed to higher winds because of the roughness elements (sand grains). We observe a quartic scaling for the vertical dust flux F_d with u_*, as $F_\mathrm{d} \propto u_*^4 \left(1 - (u_{*,\mathrm{ft}}/u_*)\right)$, with the scaling exponent having direct implications on the empirical relations in climate models. Finally, we conclude that in size regimes of $d = 5\ \mu\mathrm{m}, d = 2.5\ \mu\mathrm{m}$ grains, they are not easily entrained due to cohesion, but dust is usually present as either mostly coated on sand, or as dust clusters, thus saltation bombardment and cluster disintegration to a certain extent are the dominating mechanisms for emission as predicted before.

Contents

List of Figures

To see a world in a grain of sand
and a heaven in a wild flower,
hold infinity in the palm of your hand
and eternity in an hour.

- William Blake

Chapter 1

Introduction

Sand and dust transport is a phenomenon that occurs on both cosmic and terrestrial scales. It is usually classified as the process of sediment transport, that takes place due to the action of wind, water, and ice. The wind-blown transport also known as the Aeolian processes create the aesthetic sand ripples and dunes, bring havoc through sand and dust storms, while on a much larger time-scale, shape the very surface of our planet. This thesis although is limited to the study of aeolian erosion, where the sand is mobilized resulting in the emission of dust. The dust cycle is an integral part of the global ecosystem, it interacts with the atmosphere responsible for local fluctuations in temperature, precipitation and acts as a huge uncertainty in climate models [Shao, 2008, Kok et al., 2012]. This is an attempt to study the phenomenon more closely and provide a framework for better empirical analysis in future climate models.

At the focal point of this work lies the numerical framework of a Discrete Element Method (DEM) model, which can track individual grains in the system, subject to turbulent flow conditions. This includes the consideration of a coupling between the discrete elements and the hydrodynamics of the fluid, the contact mechanics and interparticle forces. As this is a computationally expensive methodology, it was significant to build an efficient parallelizable software/tool to also incorporate and simulate large polydisperse systems. We would from here-on interchangeably use the terms *particles*, *grains*, *aerosols*. Below, I describe briefly the structure of the thesis.

In the following section, I begin with the general motivation behind this study and then discuss the underlying Physics behind the transport in Chapter (2). Chapter (3) is dedicated to introduce the particle-based DEM methodology and the contact mechanics involved. In Chapter (4), the various scaling laws for aeolian saltation are explored, and is followed with a novel scaling law for simulating transport under low-sand availability conditions. Chapter (5) forms the basis for validation of the model for dust regime, where the model was further extended to include some essential features, and threshold conditions for transport were compared with experimental/field measurements. The results for the simulations of dust emission are discussed in Chapter (6), finally concluding with some outlook and scope for future work in Chapter (7).

1.1 Motivation

The sources of atmospheric aerosols are of anthropogenic origin (industries, vehicles and other biogenic aerosols), and of natural origin emitted in abundance from deserts, volcanic eruption, forest fires and sea salt [Prospero et al., 2002]. Off them all, the major source for atmospheric dust are indeed the vast deserts, mainly the Sahara, the Arabian and the Gobi. The Sahara Desert is often highlighted as one of the largest sources of mineral dust globally, around $400 - 700 \times 10^6$ tons/year [Middleton and Goudie, 2001] and thus is often the geographical area of interest for climate scientists and geologists. Figure (1.1) shows a large dust plume on its way crossing the Atlantic sometimes reaching as far as parts of both the North/South American continent most of which occurs during May to June. It is also believed that these mineral nutrients from the Sahara have been feeding the Amazon rainforest [Yu et al., 2019]. Some studies suggest that Saharan dust storms may suppress hurricane formation and intensity, and the dry and stable air associated with

the dust can create unfavourable conditions for the development of tropical cyclones over the Atlantic [Dunion and Velden, 2004]. The dust from Sahara can also makes its way northwards towards Europe during summer months, due to development of low-pressure systems over the Mediterranean [Pey et al., 2013, Wang et al., 2020].
Sediment transport, particularly from aeolian (wind-driven) erosion, can have significant implications for various environmental, ecological, and human-related aspects. Here are some general implications:

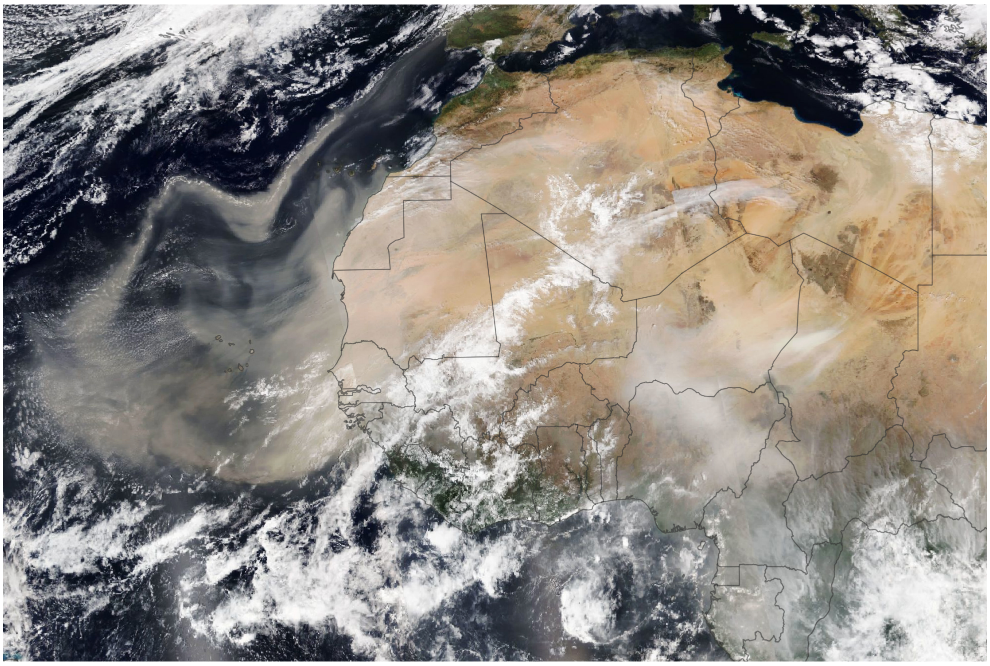

Figure 1.1: Dust transport from the Sahara desert across the Atlantic ocean due to prevailing wind conditions, and sometimes makes northward journey to Europe [NASA (https://earthobservatory.nasa.gov/images)].

- *Desertification* - Persistent aeolian erosion can contribute to the expansion of desert areas and the process of desertification. This poses a threat to ecosystems, biodiversity, and the livelihoods of people living in affected regions. Recent detailed reports [UNCCD, 2017] suggest desertification now directly affects over 2 billion humans and countless flora and fauna, which could trigger mass migrations.

Figure 1.2: Desertification is an immediate crisis affected by moving deserts and growing arid lands [https://unsplash.com/@tokeller]

- *Soil degradation* - Aeolian erosion can lead to the removal of fertile topsoil, contributing to soil degradation. This process reduces soil quality, nutrient content, and overall productivity, impacting agricultural lands and ecosystems. Various methods are proposed to combat this, which are a matter of debate, but with more and more research pointing towards no-till farming, agricultural practises to increase organic content in the soil, tree-based farming methods [Jose, 2009]. It has also been show how soil degradation, which affects the soil microbial health [Van Der Heijden et al., 2008], thereby indirectly affecting the nutrient content in the produce raising concerns over sustainability. The strong feedback loop arising from both desertification and soil degradation is showcased in Fig. (1.3).

- *Erosion of Landscapes* - Aeolian erosion can shape and modify landscapes, leading to the formation of features such as sand dunes, yardangs, and deflation basins. The large-scale erosion events from these areas alter the geomorphology of regions and can impact local ecosystems.

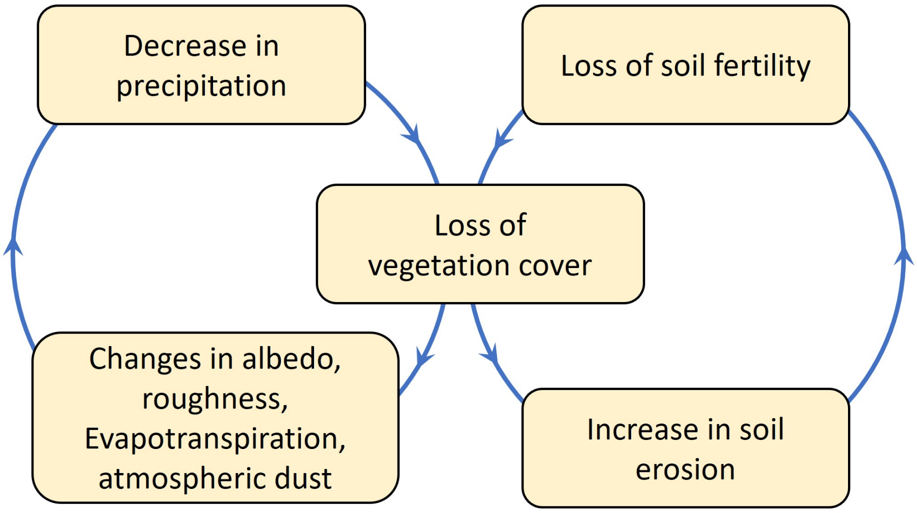

Figure 1.3: The climate feedback illustrating the effect of erosion on vegetation which is amplified by other effects. Top loop - vegetation-atmosphere, bottom loop - erosion-vegetation; image extracted from [D'Odorico et al., 2013]

- *Air Quality and Respiratory Health* - The suspension of fine particles in the air during aeolian erosion events can degrade air quality. Inhalation of airborne dust particles can have adverse effects on respiratory health, especially for individuals with pre-existing conditions [Goudie, 2009].

- *Changes in Surface Albedo* - The deposition of wind-blown sediments can alter the reflective properties of surfaces. For example, the presence of dust or sand on snow and ice surfaces reduces their albedo, accelerating melting and influencing the local climate [Painter et al., 2012].

- *Nutrient Redistribution* - Transported aeolian sediments may contain mineral nutrients, including essential elements like phosphorus, potassium and nitrogen. The redistribution of these nutrients can impact nutrient cycles, soil fertility, and ecosystem dynamics [Okin et al., 2004].

- *Transport of micro-organisms* - Aeolian transport can carry micro-organisms, including bacteria and fungi, which are usually dispersed on the surface of sand and dust, over large distances [Griffin, 2007, Erkorkmaz et al., 2023]. This has implications for the distribution of microbial life, potentially influencing ecological dynamics, human health, and biogeochemical cycles.

- *Impact on Human Infrastructure* - Aeolian transport can result in the abrasion of surfaces, leading to the erosion of buildings, infrastructure, and transportation systems. Wind-blown sand and dust can also pose challenges for maintaining and operating machinery and equipment.

- *Feedback to Climate Change* - Aeolian erosion contributes to the release of mineral dust into the atmosphere. These airborne particles can travel over long distances, influencing atmospheric composition, radiative forcing, and climate dynamics. These processes are part of complex feedback loops in the Earth's climate system. Changes in land use, vegetation cover, or climate conditions can influence aeolian erosion, contributing to feedback mechanisms that impact regional and global climate dynamics [Kok et al., 2018].

1.2 A meteorological perspective - Climate Change

The last point described above in the generic implications, points to Climate change. We are at a juncture in time, where Climate Change has become a topic of discussion in all aspects of life. We have acknowledged the phenomenon of global warming due to greenhouse gas emissions, and addressed the complexity arising due to the various feedbacks in the Physical Climatology. However it is important to define *Climate Change* from a historic perspective as well.

The energy received from Sun is not received uniformly, and thus is the major force driving wind patterns, atmospheric circulations, etc. Earth's

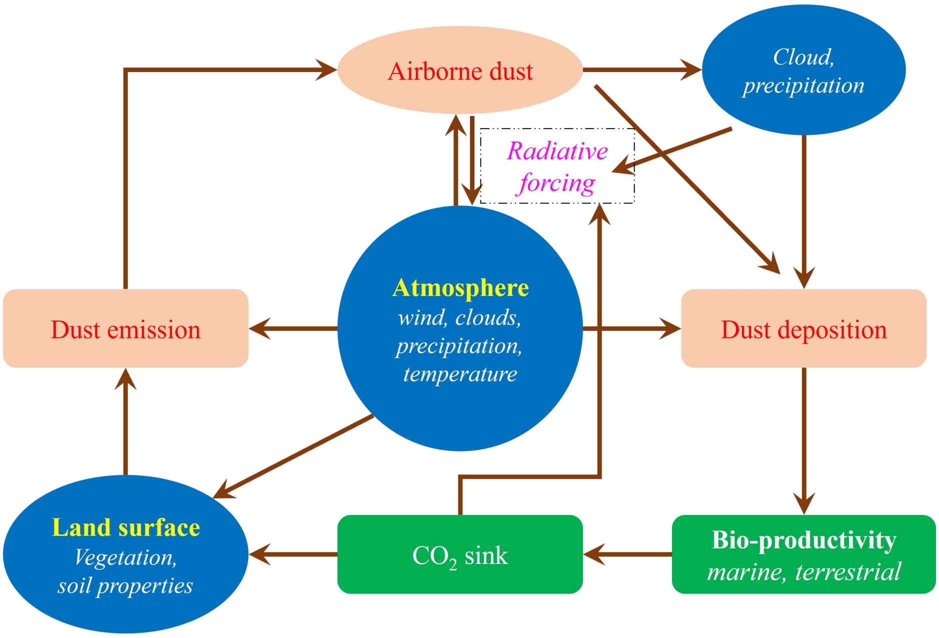

Figure 1.4: Dust aerosols interact and provide feedback to various climate systems (idea extracted from [Shao et al., 2011])

climate has been changing on a scale of thousands of years, mainly attributed to what is known as the Milankovitch cycles. The variations in Earth's eccentricity around the Sun, axial tilt and precession angles create cyclical changes to how much Solar energy is received on the planet. This resulted in glacial periods throughout history, and is thus precisely considered in Climate models. Due to human intervention and with the predictions for CO_2 concentrations, the next scheduled glacial period might be postponed for another 100,000 years [Ganopolski 2016]. The industrial revolution in the last 100 years has created a spike in the atmospheric CO_2 concentrations, the effects of which has clearly caused global warming which has resulted in global fluctuations to the Climate. It is beyond doubt we can say that, we need to hurry to address our carbon emissions quota, also addressing other problems attached to providing sustainable solutions to the global population.

Where do sand and dust fit in this story? As pointed out earlier, the solar energy is essentially absorbed and reflected by clouds and atmospheric aerosols, resulting in a negative radiative forcing. Aerosols affect the cloud formation

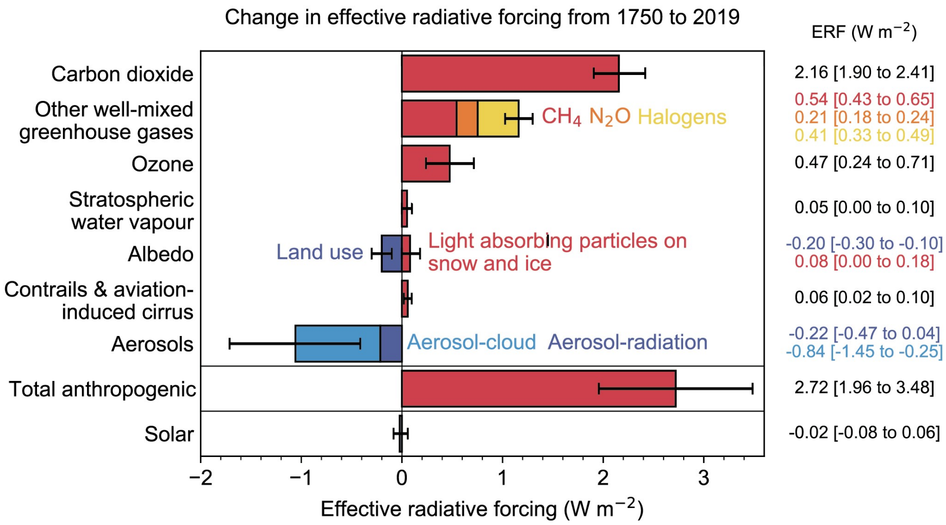

Figure 1.5: Positive radiative forcing arising from greenhouse gases, while a negative forcing from the aerosols [IPCC, 2021].

by providing a surface for the process of nucleation [Twomey, 1977], and is not in the scope of this thesis but is a direct effect of aerosols on regional precipitation. The concentration of aerosols is generally believed to be a negative radiative forcing term which means they provide a *cooling effect* [Kok et al., 2023]. However, some studies [Bauer et al., 2007] have noted the effect of sulfate/nitrate coated dust can increase the radiative forcing due to difference in optical properties. It is clear of the existence of huge uncertainties in the Aerosol Optical Depth (AOD) in the atmosphere, and is essentially one of the largest contributor to the uncertainty in our climate predictions as is shown in Fig. (1.6).

1.3 Need for particle-based models

This brings us to the need for better understanding of the process of sand and dust transport to validate macroscopic observations like the horizontal sand flux, and the vertical dust fluxes as functions of the wind speed. To this end, particle-based models are indispensable on a microscopic scale due

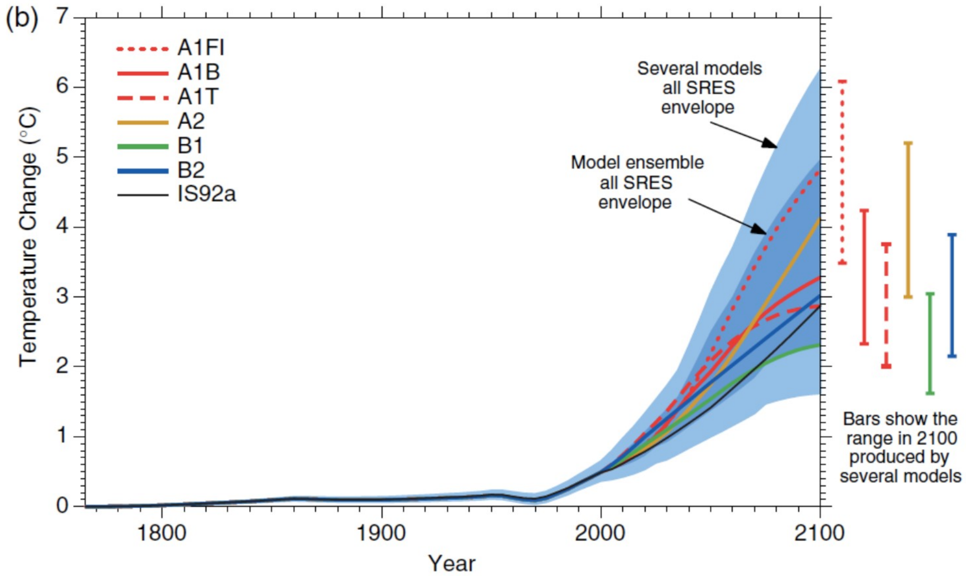

Figure 1.6: Climate projection uncertainties from various climate models [IPCC, 2001].

to the intricate interplay of numerous factors influencing these processes. By incorporating particle interactions, collisions, and entrainment mechanisms, these models can capture the complex dynamics of aeolian transport more accurately than continuum-based approaches. Additionally, they facilitate the study of phenomena like saltation, creep, and suspension, essential for predicting sediment transport rates and patterns in diverse landscapes. This has been successfully demonstrated in the past [Carneiro et al., 2011, Durán et al., 2014, Pähtz et al., 2012, Comola et al., 2019] in studying mainly the saltation dynamics of sand grains, but this thesis is a fresh attempt in simulating direct numerical simulations at the scale of microscopic dust. We start first by building the model, followed by validating key outputs like the sand flux, entrainment thresholds, dust flux rates, etc. This software is intended towards providing better empirical relations for global climate models, as well as aiding in environmental management, dust emission mitigation, and desertification control efforts.

Chapter 2

Physics of Aeolian transport

The term *Aeolian/Eolian*, originates from *Aeolus*, the ancient Greek god of the winds. In the context of geomorphology and geophysics, *aeolian* pertains to processes involving wind-driven erosion, transport and deposition of sediments. This phenomenon is not just limited to desert environments, but also in regions devoid of soil moisture, sparse vegetation and a consistent supply of sediments. Brigadier Ralph Alger Bagnold, a British engineer and soldier during his expeditions through the Libyan desert, conducted groundbreaking research during and after World War II, and his seminal work laid the foundation for the modern understanding of aeolian processes [Bagnold, 1937].

2.1 Transport modes

Aeolian transport is broadly classified into 3 major modes: Creep, Saltation and Suspension [Bagnold, 1941, Shao, 2008]. This classification fundamentally arises from the particle size and the strength of wind, however here it is based on the general wind intensity observed on Earth as illustrated in Fig. (2.1). The competing gravitational, lift, cohesive and turbulent drag forces make the movement of grains hard or easy, depending on the direction of action.

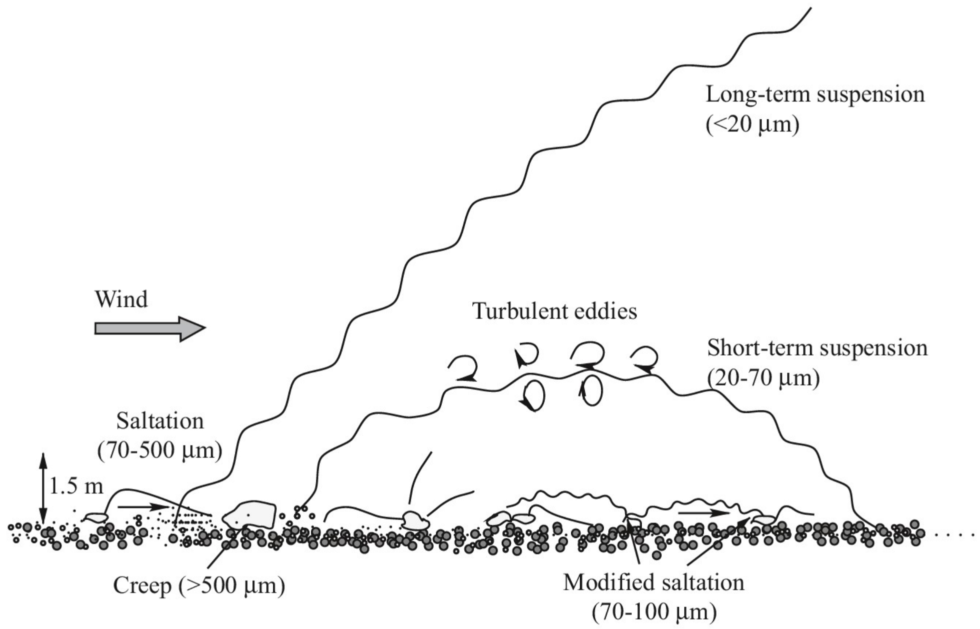

Figure 2.1: Aeolian transport modes of sand and dust (extracted from [Shao, 2008]).

Creep/Reptation is the movement of large grains ($\gtrapprox 500\ \mu$m) which are hardly lifted and would just move along the surface due to wind shear or could be slightly lifted because of other colliding grains [Bagnold, 1941, Ungar and Haff, 1987, Namikas, 2003]. The discrete nature of the elements in the current model allows us to model creeping motion.

Saltation, with it's Latin origin *saltare* means to *jump/leap/hop.* This hopping motion of grains is commonly observed for diameters ranging $\approx 70 - 500\ \mu$m, while in above threshold conditions, the lifted grains are accelerated by the wind as they ascend, and eventually returned to the surface by gravity [Bagnold, 1941]. Statistically, the ejected particles have a higher lift-off angle ($\approx 55°$), while the impacting grains touchdown at a lower angle ($\approx 10°$) [Shao, 2008]. This proceeds with a domino effect, where the particle bombardments could lead to *splash* more grains into motion. Initially there is an exponential increase in the grains which are triggered into saltation, which ends up in a steady state process which is attributed to the *"negative feedback effect"* which I describe later in Section (2.4) [Anderson and Haff, 1991, Durán et al., 2012]. This particular mode is further subdivided for smaller grains ($\approx 70 - 100$ μm) as modified saltation, wherein the particle trajectories are not exactly deterministic, but affected by turbulent fluctuations [Einstein and El-Samni, 1949]. Saltation is often considered as the significant mode of the three, resulting in the emergence of macroscopic patterns such as ripples and dunes. The detailed study of saltation, has led to modeling and modern understanding of evolving desert dunes [Sauermann et al., 2001, Parteli et al., 2007].

Suspension Suspension refers to the transport of fine grains, more commonly categorized to as dust ($\lessapprox 70$ μm). The low terminal/settling velocity of the grain allows for its longer residence time while suspended in the air. The turbulent wind can then disperse the particles higher into the atmosphere, where large-scale atmospheric circulations can further drive them away to long distances. A further subdivision is made to distinguish between long-term suspension ($\approx 20 - 70$ μm) and long-term suspension ($\lessapprox 20$ μm) [Shao, 2008]. Dust is believed to be not entrained easily because of dominant cohesive forces [Shao and Lu, 2000], and is usually emitted by either saltating grains splashing dust or a larger dust agglomerate disintegration. The turbulent eddies are also what drives these stochastic trajectories for the dust grains, and thus these last two points are elaborately discussed in Chapter (6). Modeling these ejection mechanisms has gained attention in the last three decades with its relevance to climate change as discussed in Section (1.1).

2.2 Fluid initiation problem

A particle at rest on the bed (Fig. (2.2)), is influenced by the gravitational force ($\mathbf{F}^{\mathrm{g}}$), the inter-particle force ($\mathbf{F}^{\mathrm{c}}$), the electric force ($\mathbf{F}^{\mathrm{e}}$) due to the electrostatic build-up on the grains [Schmidt et al., 1998], and the aerodynamic drag and lift forces ($\mathbf{F}^{\mathrm{d}}$) and ($\mathbf{F}^{\mathrm{l}}$) respectively. The Magnus force [White and Schulz, 1977] ($\mathbf{F}^{\mathrm{m}}$) is left out from the model for the sake of simplification, and it's minor effect on the overall dynamics [Kok et al., 2012]. The electric force is also opted out but it essentially carries huge scope for future research, particularly insightful is the triboelectric charging of grains [Lacks and Shinbrot, 2019].

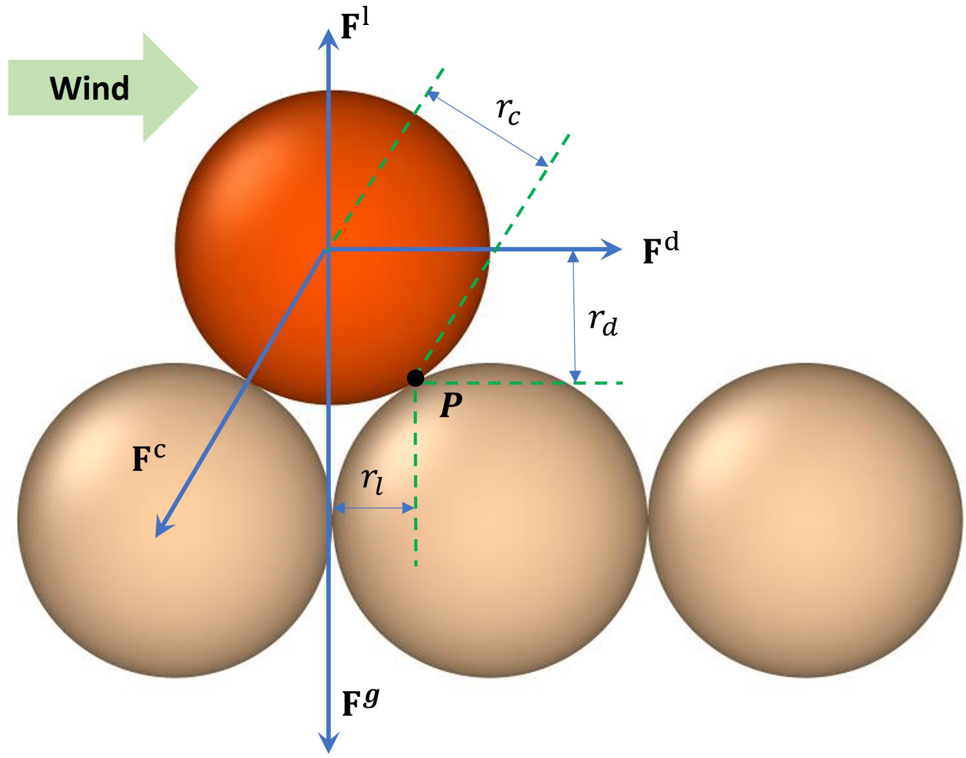

Figure 2.2: The particle forces at balance, but rolling ensues if the wind drag exceeds the inhibition from the underlying forces on the grain. This minimal velocity is called the fluid threshold $u_{*,\mathrm{ft}}$ (modified from [Kok et al., 2012]).

At the fluid threshold, the balancing forces or the equivalent moment induced makes the particle pivot at $\boldsymbol{P}$:

$$r_d\mathbf{F}^{\mathrm{d}} + r_l\left(\mathbf{F}^{\mathrm{l}} - \mathbf{F}^{\mathrm{g}}\right) - r_c\mathbf{F}^{\mathrm{c}} = 0 \tag{2.1}$$

where the length of the moments are given by r_d, r_l and r_c for the respective $\mathbf{F}^{\mathrm{d}}, \mathbf{F}^{\mathrm{l}}$ and $\mathbf{F}^{\mathrm{c}}$ forces. Further, [Bagnold, 1941] suggested a simple formula by neglecting the effect from the inter-particle and lift forces.

$$r_d\mathbf{F}^{\mathrm{d}} - r_l\mathbf{F}^{\mathrm{g}} = 0 \tag{2.2}$$

If d is the particle diamter, ρ_{p} the particle density ($= 2650$ kg/m^3), ρ_{a} the air density ($= 1.225$ kg/m^3), g the acceleration due to gravity, the gravitational force $\mathbf{F}^{\mathrm{g}}$ is simply put as,

$$\mathbf{F}^{\mathrm{g}} = \frac{\pi}{6}\rho_{\mathrm{p}} g d^3 \tag{2.3}$$

while the aerodynamic drag $\mathbf{F}^{\mathrm{d}}$ is expressed as,

$$\mathbf{F}^{\mathrm{d}} = \frac{1}{2}\rho_{\mathrm{a}} C^{\mathrm{d}} A (U^{\mathrm{s}})^2 \tag{2.4}$$

where, C^{d} is the drag coefficient, A is the surface area ($= \pi d^2/4$) of the exposed grain, and U_{s} is the mean flow speed at a reference point. We hereby note the difficulty in describing the quantities C^{d} and U^{s} close to the bed surface, and allow for a reasonable approximation [Bagnold, 1941, Shao, 2008].

Also, the fluid shear stress (τ^{f}) relates to the friction velocity (u_*) which by definition is a parameter to indicate the momentum flux over the surface. Hence, U_{s} is written as a proportionality to u_*.

$$\tau^{\mathrm{f}} = \rho_{\mathrm{a}} u_*^2 \tag{2.5}$$

Eqns. (2.2,2.3,2.4) simplify to arrive at the fluid threshold $u_{*,\mathrm{ft}}$,

$$u_{*,\mathrm{ft}} = A_\tau \sqrt{\frac{\rho_\mathrm{p}}{\rho_\mathrm{a}} g d} \tag{2.6}$$

Here, A_τ encodes the information about the drag coefficient, which has a dependency on the particle Reynolds number (Re). Bagnold fit a value of $A_\tau \approx 0.1$, which is a good estimate of the threshold for high Re > 3.5 [Shao, 2008]. Here, note the Reynolds number definition where the friction velocity u_* is part of, based on the same assumption that the relative velocity between the fluid and particle is of the order of u_*.

$$\mathrm{Re} = \frac{u_* d}{\nu} \tag{2.7}$$

ν is the kinematic viscosity. For smaller Reynolds number, Re $<< 3.5$, Bagnold noticed the increase in the $u_{*,\mathrm{ft}}$, and associated it with the *smooth* surface, where the surface roughness is smaller. Of course, we now are aware of this *smooth-surface effect* which could slightly increase the threshold, but this is not the vital factor which causes the threshold increase for finer grains as we discuss later in Section (5.3).

[Greeley and Iversen, 1987] first propagated the idea of the inter-particle cohesion causing the increase in threshold for small grains. They proposed an empirically motivated set of dependency for A_τ in Eqn. (2.6) as follows -

$$A_\tau = A_1 F(\mathrm{Re})\, G(d) \tag{2.8}$$

where $F(\mathrm{Re})$ and $G(d)$ are functions describing the dependency on Re and cohesion respectively, while A_1 is a constant slightly varying with Re.

Re	A_1	$F(\mathrm{Re})$
$0.03 \leq \mathrm{Re} \leq 0.3$	0.20	$(1 + 2.5\mathrm{Re})^{-1/2}$
$0.3 \leq \mathrm{Re} \leq 10$	0.13	$\left(1.928\mathrm{Re}^0.092 - 1\right)^{-1/2}$
$\mathrm{Re} \geq 10$	0.12	$1 - 0.0858\exp\left[-0.0617\left(\mathrm{Re} - 10\right)\right]$

The function $G(d)$ incorporating the cohesive effects was described as,

$$G(d) = \left[1 + \frac{0.006}{\rho_{\mathrm{a}} g d^{2.5}}\right]^{1/2} \tag{2.9}$$

[Shao and Lu, 2000] provides a simpler expression with a physical explanation when considering cohesion. The cohesive force is specified as a proportionality to the particle diameter,

$$\mathbf{F}^{\mathrm{c}} = \beta_c d \tag{2.10}$$

We can then rewrite Eqn. (2.2) to include the inter-particle cohesion from Eqn. (2.10),

$$r_d \mathbf{F}^{\mathrm{d}} - r_l \mathbf{F}^{\mathrm{g}} = r_c \mathbf{F}^{\mathrm{c}} \tag{2.11}$$

The final form of the equation that captures the behavior of fluid threshold through the different regimes is given as,

$$u_{*,\mathrm{ft}} = 0.11\sqrt{\frac{\rho_{\mathrm{p}}}{\rho_{\mathrm{a}}} g d + \frac{\gamma_{\mathrm{shao}}}{\rho_{\mathrm{a}} d}} \tag{2.12}$$

where

$$\gamma_{\mathrm{shao}} = \frac{6}{\pi}\frac{r_c}{r_l}\beta_c \tag{2.13}$$

γ_{shao} varies in a range of 1.65×10^{-4} kg/s^2 and 5×10^{-4} kg/s^2. In the limit of $d \to \infty$, $u_{*,\mathrm{ft}} \propto d^{1/2}$, while in the lower limit of $d \to 0$, $u_{*,\mathrm{ft}} \propto d^{-1/2}$. I would revisit this equation later in Section (5.3), as a source of validation for my model.

2.3 Forces on the airborne grain

The forces on an airborne particle is proposed just like for the resting particle, but now with more emphasis on the aerodynamic forces. The Discrete-Element nature of the model allows for a descriptive methodology of considering the influence of external forces on all particles in the system. This would also mean the inter-particle collisions and attractions due to the presence of cohesive forces. The trajectory of every particle is thus predicted through small time-steps by computing the acceleration induced by the force fields, and the velocity and positions are updated. The numerical methodology of the collision detections and computations using the DEM framework are outlined in Chapter (3). The ideal scenario of a mid-air collision could capture all these phenomena as illustrated in Fig. (2.3).

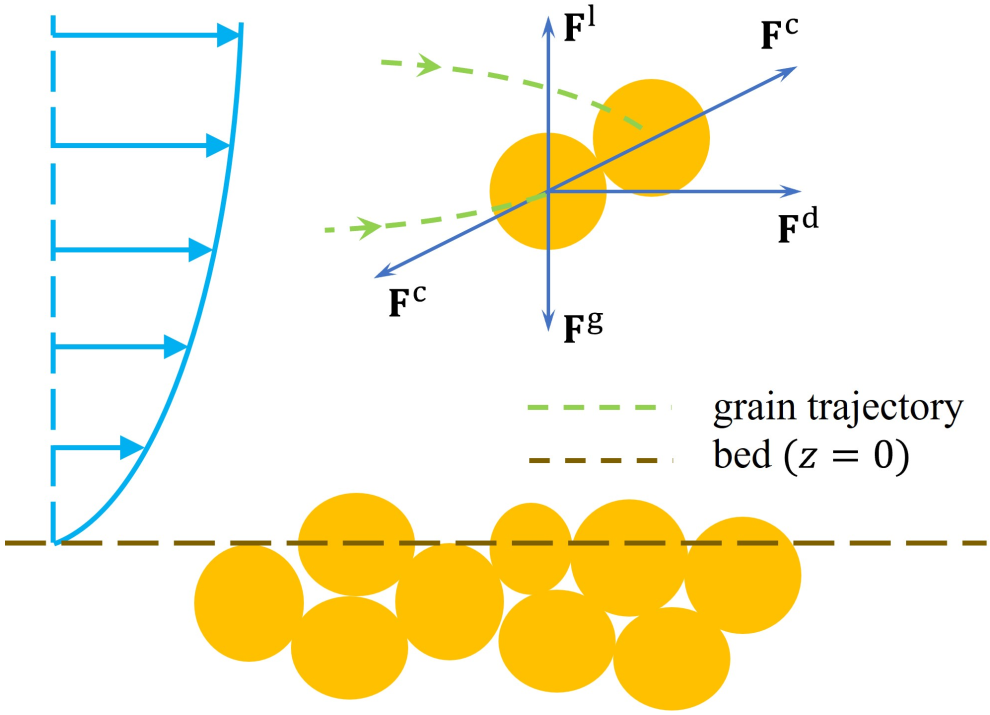

Figure 2.3: Full scale trajectory of two colliding particles and the influence of various forces involved with the turbulent wind.

$$\frac{d\mathbf{v}_i}{dt} = \frac{1}{m_i}\left(\mathbf{F}_i^{\mathrm{g}} + \mathbf{F}_i^{\mathrm{d}} + \mathbf{F}_i^{\mathrm{l}} + \mathbf{F}_i^{\mathrm{c}} + \mathbf{F}_i^{ip}\right) \tag{2.14}$$

where the indices $\mathrm{g}, \mathrm{d}, \mathrm{l}, \mathrm{ip}, \mathrm{c}$ refer to the gravitational, drag, lift, contact and cohesive forces (here cohesion is modelled as a pure intermolecular van der Waals attraction) respectively.

The gravitational component $\mathbf{F}_i^{\mathrm{g}}$ acting only in the negative z,

$$\mathbf{F}_i^{\mathrm{g}} = \frac{\pi}{6}\rho_{\mathrm{p}} g d^3 \tag{2.15}$$

The aerodynamic drag force $\mathbf{F}_i^{d}$,

$$\mathbf{F}_i^{\mathrm{d}} = \frac{\pi}{8}\rho_{\mathrm{a}} d^2 C^{\mathrm{d}}\left(\mathrm{Re}\right) v^{\mathrm{r}}\mathbf{v}^{\mathrm{r}} \tag{2.16}$$

where C^{d} is the drag coefficient as a function of the particle Reynolds number Re given by [Cheng, 1997] described below. $\mathbf{v}^{\mathrm{r}} = \mathbf{u} - \mathbf{v}$ is the relative velocity between the wind and the particle, while v^{r} is the absolute magnitude of the relative velocity, $|\mathbf{v}^{\mathrm{r}}| = |\mathbf{u} - \mathbf{v}|$.

$$C^{\mathrm{d}} = \left[\left(\frac{32}{\mathrm{Re}}\right)^{2/3} + 1\right]^{3/2} \tag{2.17}$$

where Re is expressed as,

$$Re_p = \frac{v^{\mathrm{r}} d}{\nu} \tag{2.18}$$

Here ν is the kinematic viscosity [kg/ (m.s)] defined as the ratio of the dynamic viscosity $(\mu^{\mathrm{f}}) = 1.8702 \times 10^{-5}$ m^2/s to the density of the fluid $(\rho_{\mathrm{a}}) = 1.225$ kg/m^3.

The choice of Eqn. (2.17) is ideal as we model perfectly spherical particles, as this definition of C^{d} encapsulates the drag effect on irregular shapes found in nature [Cheng, 1997]. That is, in the turbulent limit $\mathrm{Re} \to \infty, C^{\mathrm{d}} \to 1$, instead of $C^{\mathrm{d}} \to 0.4$ for spheres [Ferguson and Church, 2004]. Also, in the laminar limit usually termed as the *Stokes regime* where $\mathrm{Re} \to 0, C^{\mathrm{d}} \to 32/\mathrm{Re}$, is also slightly higher than the Stokes limiting law $C^{\mathrm{d}} = 24/\mathrm{Re}$.

The aerodynamic lift force $\mathbf{F}_i^{l}$ is a direct application from the Bernoulli principle [Shao, 2008],

$$\mathbf{F}_i^{\mathrm{l}} = \frac{\pi}{8}\rho_{\mathrm{a}} d^3 C^{\mathrm{l}}\left(\nabla|\mathbf{u}|^2\right) \tag{2.19}$$

2.3.1 Modeling cohesion

The attractive force of cohesion is modelled using only the van der Waals interaction, which arise from the electrodynamic fluctuations at the quantum scale [Dzyaloshinskii et al., 1961]. Although most commonly used in molecular dynamics, the van der Waals forces is also innately present in macroscopic matter [Hamaker, 1937] and is a significant part of the *dust* story. As a result, it can get really sticky when dust and sand get together, making it difficult for individual dust grains to be lifted off by the wind and would be revisited later in Section (5.3). The grains in nature are also exposed to other cohesive forces like electrostatic interactions and liquid-bridges, but are excluded from the scope of this thesis. The model equations/parameters here are taken from previous usages [Hamaker, 1937, Parteli et al., 2014b] and is given for a particle pair i, j as a conditional function of their overlap distance $\delta_{ij,\mathrm{n}}$ describing a weak short-ranged force -

$$\mathbf{F}^{\mathrm{c}}_{ij} = \begin{cases} \dfrac{A_{\mathrm{H}} d_{\mathrm{eff}}}{12 D^2_{\mathrm{min}}} \cdot \mathbf{e}_{ij,\mathrm{n}} & \text{if } \delta_{ij,\mathrm{n}} > 0 \\ \dfrac{A_{\mathrm{H}} d_{\mathrm{eff}}}{12(\delta_{ij,\mathrm{n}} - D^2_{\mathrm{min}})} & \text{if } -D_{\mathrm{max}} \leq \delta_{ij,\mathrm{n}} \leq 0 \\ 0 & \text{if } \delta_{ij,\mathrm{n}} < -D_{\mathrm{max}} \end{cases} \tag{2.20}$$

where the overlap distance $\delta_{ij,\mathrm{n}}$ is given by,

$$\delta_{ij,\mathrm{n}} = R_i + R_j - |\vec{\mathbf{r}}_i - \vec{\mathbf{r}}_j| \tag{2.21}$$

Here a positive value implies that the particles overlap, while a negative value would mean they are separated, with the force vanishing at a distance greater than the cutoff $D_{\mathrm{max}} = 1\ \mu\mathrm{m}$. A_{H} is the Hamaker constant and is related to the surface energy density (γ_{s}) as [Götzinger and Peukert, 2003],

$$A_{\mathrm{H}} = 24\pi D^2_{\mathrm{min}} \gamma_{\mathrm{s}} \tag{2.22}$$

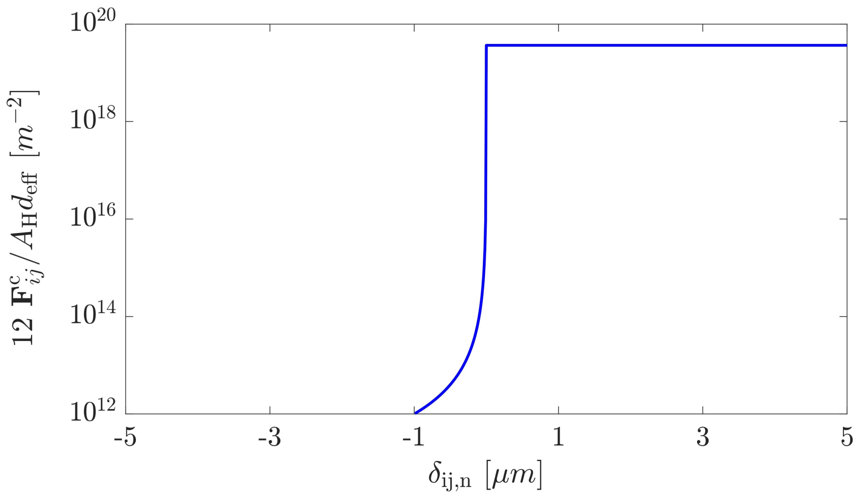

Figure 2.4: The van der Waals force is held constant through the contact process, while it vanishes quickly within a interaction cutoff distance $D_{\mathrm{max}} = 1\ \mu$m.

D_{min} is just a parameter used to avoid the singularity condition in Eqn. (2.20) when $\delta_{ij,\mathrm{n}} = 0$. It can also be thought of as a minimum distance occurring because of the surface roughness at the point of contact [Krupp, 1967, Israelachvili, 1998] and a value of $D_{\mathrm{min}} = 1.65$ Å is considered.

The experimental investigations of these dispersive surface interactions were performed by [Götzinger and Peukert, 2003], thereby providing with some direct measurements of the Hamaker constant using an atomic force microscope (AFM). The value of surface energy density ($\gamma_{\mathrm{s}} = 0.05$ J/m^2) used as a derivative of these experiments in [Parteli et al., 2014b], resulted in good validations in packing behavior of glass powders when compared to experiments.

2.4 Fluid dynamics

The hydrodynamics describing the mean fluid field is described by the Reynolds Averaged Navier-Stokes (RANS) equation [Durán et al., 2011] (note in the conventional notation below, that the suffices i, j represent x, y, z directions and not the the particle index),

$$\rho_a \left(\frac{\partial \mathbf{u}_i}{\partial t} + \mathbf{u}_j \frac{\partial \mathbf{u}_i}{\partial j} \right) = \left(-\frac{\partial p^{\mathrm{f}}}{\partial i} + \rho_{\mathrm{a}} g_i + \frac{\partial \tau_{ij}^{\mathrm{f}}}{\partial j} \right) \tag{2.23}$$

In the presence of particles, we now consider the particle volume fraction (ϕ) to describe the remaining fluid fraction ($1-\phi$), and an additional term which we previously noted as the negative feedback force ($\mathcal{F}_i$) exerted by the grains to the flow -

$$\rho_{\mathrm{a}} (1-\phi) \left(\frac{\partial \mathbf{u}_i}{\partial t} + \mathbf{u}_j \frac{\partial \mathbf{u}_i}{\partial j} \right) = (1-\phi) \left(-\frac{\partial p^{\mathrm{f}}}{\partial i} + \rho_{\mathrm{a}} g_i + \frac{\partial \tau_{ij}^{\mathrm{f}}}{\partial j} \right) - \mathcal{F}_i \tag{2.24}$$

where u is the mean wind velocity, (thus LHS term is the fluid inertia), ∂p^{f} the pressure gradient, term $\rho_{\mathrm{a}} g_i$ the gravitational effect and τ_{ij}^{f} the total fluid borne shear stress.

A steady homogeneous transport model, with a uni-directional wind in x, with no pressure gradient leads to,

$$\frac{\partial \tau_{xz}^{\mathrm{f}}}{\partial z} = \frac{\mathcal{F}_x (z)}{(1-\phi(z))} \tag{2.25}$$

τ from here-on would mean τ_{xz}, the horizontal shear stress transferred in the vertical direction.

As more grains are put into the transport layer, the total available stress for shearing is partitioned into the contributions from the fluid and the grains. That is,

$$\tau^{\mathrm{t}}(z) = \tau^{\mathrm{f}}(z) + \tau^{\mathrm{g}}(z) \tag{2.26}$$

where $\tau^{\mathrm{g}}(z)$ is the grain borne shear stress at a height z, which has a physical context in the horizontal momentum exchange from the upward and downward moving grains -

$$\tau^{\mathrm{g}}(z) = \int_z^\infty \frac{\mathcal{F}_x(z')}{1-\phi\,(z')}\,dz' \tag{2.27}$$

The computation of $\tau^{\mathrm{g}}(z)$, or the grain-shear stress profile is of importance, as it serves as the *negative feedback* to the fluid flow from grains, or,

$$\tau^{\mathrm{f}}(z) = \rho_{\mathrm{a}} u_*^2 - \tau^{\mathrm{g}}(z) \tag{2.28}$$

The fluid borne shear stress (τ^{f}) again comprises of the viscous stress (τ_ν^{f}) and the turbulent Reynolds stress (τ_R^{f}) as,

$$\tau^{\mathrm{f}} = \tau_\nu^{\mathrm{f}} + \tau_R^{\mathrm{f}} \tag{2.29}$$

Viscous shear stress (τ_ν^{f}) is the force per unit horizontal area that arises due to the internal friction between adjacent layers of a fluid as they move relative to each other. This phenomenon is inherently a result of fluid viscosity, that describes its resistance to deformation and flow and is well produced by the Newton's law of viscosity. The

$$\tau_\nu^{\mathrm{f}} = \rho_{\mathrm{a}} \nu \frac{\partial u}{\partial z} \tag{2.30}$$

The Reynolds shear stress τ_R^f is given by,

$$\tau_R^{\mathrm{f}} = -\rho_{\mathrm{a}} \widehat{u'w'} \tag{2.31}$$

where u' and w' are the temporal fluctuations in the horizontal and vertical wind velocity. By using a Prandtl-like turbulent closure [Prandtl, 1925], a characteristic length-scale called as the *mixing length* l_{m} is introduced. Conceptually, l_{m} is a measure of the distance over which a fluid parcel (or eddy) retains its original properties (like velocity and momentum) before being significantly affected by the surrounding fluid, that is the momentum is exchanged with the surrounding eddies/parcels.

$$\tau_R^{\mathrm{f}} = \rho_{\mathrm{a}} l_{\mathrm{m}}^2 \frac{\partial u}{\partial z} \left| \frac{\partial u}{\partial z} \right| \tag{2.32}$$

The total fluid borne shear stress is then,

$$\tau^{\mathrm{f}} = \rho_{\mathrm{a}} \left(\nu + l_{\mathrm{m}}^2 \left| \frac{\partial u}{\partial z} \right| \right) \frac{\partial u}{\partial z} \tag{2.33}$$

The asymptotic behavior arising from this equation, when the viscosity effects are dominant close to the surface and when the turbulence serves prominence at higher heights can be explored using Eqn. (2.5), with a simple assumption for $l_{\mathrm{m}} = \kappa z$, (where $\kappa = 0.41$ is the von Kármán constant) and the no-slip boundary condition usually valid for smooth surfaces, $u(z = 0) = 0$. The transition is shown in Fig. (2.4).

Close to the surface, usually $z < 5\nu/u_*, \tau^{\mathrm{f}} \approx \tau_\nu^{\mathrm{f}}$, and the horizontal wind velocity $u\,(z)$ exhibits a linear wind profile [Rijn, 1990],

$$u(z) = z\frac{u_*^2}{\nu} \tag{2.34}$$

and at a higher height, usually $z > 30\nu/u_*, \tau^{\mathrm{f}} \approx \tau_R^{\mathrm{f}}$, and the horizontal wind velocity $u\,(z)$ exhibits the classic logarithmic wind profile [Rijn, 1990],

$$u(z) = \frac{u_*}{\kappa} \ln\left(\frac{z}{z_0}\right) \tag{2.35}$$

respectively.

where z_0 is the aerodynamic roughness length, that meaningfully represents the height from the surface at which the *extrapolated* turbulent log-profile diminishes. If for a fixed wind speed u, a higher z_0 would mean a larger u_*, hence z_0 describes the capacity of the surface to absorb fluid momentum. As a general rule for larger grains or at high Re, it has been shown that z_0 converges to a value of $\approx d_{\mathrm{m}}/30$ [Bagnold, 1941], where d_{m} is the mean grain diameter. This is a simpler approach, of considering a purely turbulent layer

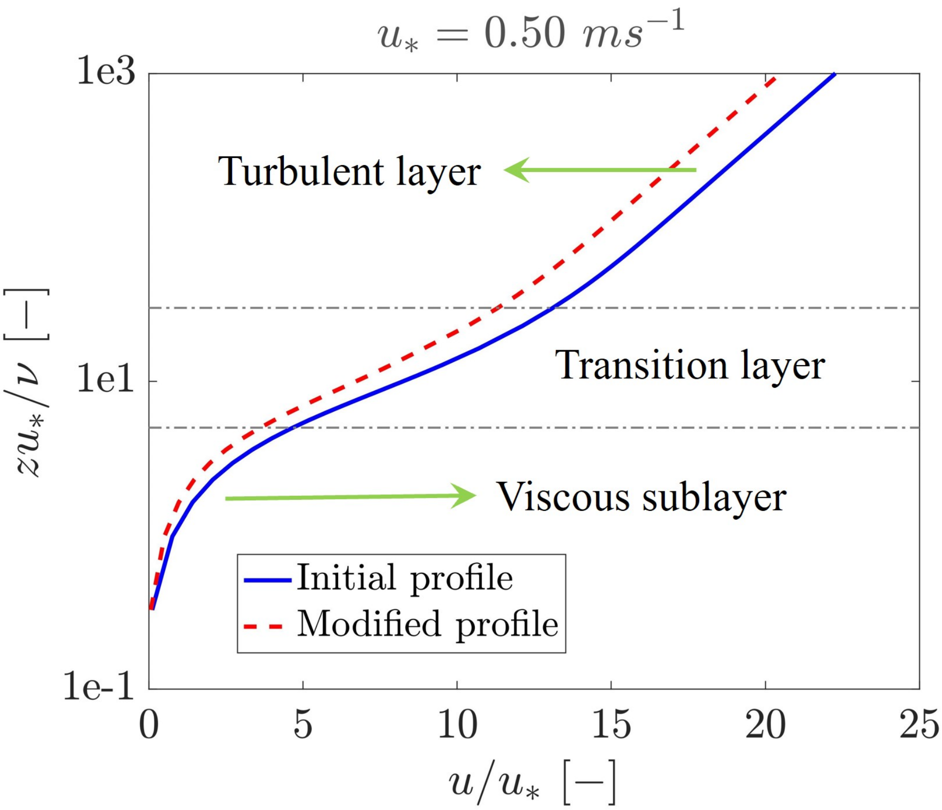

Figure 2.5: The wind profile over a smooth layer, transitions from a viscous to turbulent layer.

with this definition of z_0 previously explored for saltation dynamics [Carneiro et al., 2011, Pähtz et al., 2015, Kamath et al., 2022].

The full scale equation realized to achieve the wind velocity profile using Eqns. (2.25, 2.27, 2.28, 2.33) is then a differential equation of the form,

$$\rho_{\mathrm{a}} \left(l_{\mathrm{m}}^2 \left| \frac{\partial u}{\partial z} \right| + \nu \right) \frac{\partial u}{\partial z} = \rho_{\mathrm{a}} u_*^2 - \int_z^\infty \frac{\mathcal{F}_x(z')}{1 - \phi\,(z')}\, dz' \tag{2.36}$$

To incorporate the roughness element as a natural result of the fluid model, and to avoid the discrepancies due to the definitions of "*where/what exactly is the bed surface?*", [Durán et al., 2012, Chiodi et al., 2014] proposed the following methodology -

2.4.1 Fluid solver

The wind profile is computed by simultaneously solving a set of partial differential equations, the first one being Eqn. (2.36).

The mixing length approximation previously suggested $l_\mathrm{m} = \kappa z$. Here, a differential equation for l_m is introduced to have a continuum from inside the granular bed and transitioning above it.

$$\frac{\partial l_\mathrm{m}}{\partial z} = \kappa \left[1 - \exp\left(- \sqrt{\frac{1}{R_\mathrm{c}} \left(\frac{u l_\mathrm{m}}{\nu} \right)} \right) \right] \tag{2.37}$$

where $R_\mathrm{c} = 7$ is a constant fit from measurements.

The reference height of the static bed h_0 (or $z = 0$) is defined as the height at which the particle volume fraction drops to half of the bed fraction, $\phi(z = 0) = \phi_\mathrm{b}/2$. The computation using the granular packing fraction inside the bed is illustrated in Appendix A.

To achieve the asymptotic velocity profile inside the bed, [Durán et al., 2012] showed,s $\mathcal{F}_x(z)$ is approximated as a pure viscous drag force per unit volume given by the Stokes law as $18\rho_a \nu u\,(z)\,/d^2$, then from Eqn. (2.25),

$$\frac{\partial^2 u}{\partial z^2} = \frac{\phi_\mathrm{b}}{1 - \phi_\mathrm{b}} \frac{18}{d^2} u\,(z) \tag{2.38}$$

The solution lies in the exponential decay of velocity for $z < 0$, with a parameter λ_b,

$$\lambda_\mathrm{b} = d\sqrt{(1 - \phi_\mathrm{b})\,/\,(18\phi_\mathrm{b})} \tag{2.39}$$

That is, for example using $\phi_\mathrm{b} \approx 0.60$, $\lambda_\mathrm{b} = 0.2d$. The solution for the above exponential function is,

$$u(z) = u_\mathrm{s} \exp\left((z - z_\mathrm{s})\,/\lambda_\mathrm{b} \right) \tag{2.40}$$

where u_s is iteratively converged, by starting the integration at $(h_0 - 5d)$.

Similarly for the asymptotic mixing length profile inside the bed is,

$$l_{\mathrm{m}}(z) = \frac{\kappa^2 \lambda_{\mathrm{b}}^2}{\nu R_{\mathrm{c}}} u(z) \tag{2.41}$$

The wind profile is then achieved at every time-step, by solving the Eqns. (2.36 & 2.37) using a fourth order Runge-Kutta method, which is described along with the equations in Appendix B. For the purpose of integration, we produce equal fine horizontal grids inside the bed and close to the surface (dz) determined by the minimum of either λ_{b} or the viscous length ν/u_*,

$$dz = \frac{1}{2} \min \left[0.2d, \frac{\nu}{u_*} \right] \tag{2.42}$$

2.5 Turbulence

Turbulence is one of the most important unsolved classical problem, and is often realized by Reynolds approximation of the Navier-Stokes equation. Fig. (2.6) shows the smoke transition from laminar to turbulent flow. This transition is roughly understood with the help of Reynolds number, it is not abrupt and can be influenced by various factors. Even minute disturbances can grow exponentially if they reach a critical amplitude, leading to the onset of turbulence. Although a very important problem in Engineering in today's world, it plays a significant role in the emission and transport of dust and thus adding the turbulent fluctuations to the mean wind field is necessary, which is also later revisited in Section (5.2.5). [Einstein and El-Samni, 1949, Mollinger and Nieuwstadt, 1996] and recently a review by [Pähtz et al., 2020] have made it clear, that the fluctuations arising in the wind close to the surface can enhance grain entrainment [Zhang et al., 2022].
Turbulence in the Atmospheric Boundary Layer (ABL) arises from the interaction between the Earth's surface and the overlying atmospheric air. Factors that usually drive turbulence are uneven heating, topographical features, and surface roughness contribute to the development of turbulent flows [Stull, 2012]. The eddies generated in this process are of varying size, with

Figure 2.6: What is the origin of the onset of turbulence? Where does it transition from laminar to turbulence? This has been an age-old problem and characterising it in models is an ongoing field of debate [https://unsplash.com/@shocking57].

the largest eddies deriving their kinetic energy from the mean flow, and it is important to study the turbulent kinetic energy ($\overline{e}$) in the length scale close to the bed.

$$\overline{e} = \frac{1}{2}\left(\overline{u'^2} + \overline{v'^2} + \overline{w'^2}\right) \tag{2.43}$$

where u', v', w' are the fluctuating velocity components in each direction.

$$\frac{\partial \overline{e}}{\partial t} + \overline{u_j}\frac{\partial \overline{e}}{\partial x_j} = \delta_{i3}\frac{g}{\overline{\theta_\nu}}\overline{u_i'\theta_\nu'} - \overline{u_i'u_j'}\frac{\partial \overline{u_i}}{\partial x_j} - \frac{\partial \overline{u_i'e}}{\partial x_j} - \frac{1}{\overline{\rho}}\frac{\partial \overline{u_i'p'}}{\partial x_i} - \epsilon \tag{2.44}$$

Here, the energy is injected into the flow at the large-scale eddies due to the mechanical wind shear indicated by the production term,

$$\overline{u_i'u_j'}\frac{\partial \overline{u_i}}{\partial x_j} \tag{2.45}$$

The transport of the turbulent kinetic energy into smaller size eddies and is represented by the term,

$$\frac{\partial \overline{u_i' e}}{\partial x_j} \tag{2.46}$$

At the smallest scale, dissipation term occurs due to the viscous effects near the surface and is given as,

$$\epsilon = \nu \overline{\frac{\partial u_i'}{x_j}\frac{\partial u_i'}{x_j}} \tag{2.47}$$

The energy that is mechanically produced as turbulence is lost from the mean flow.

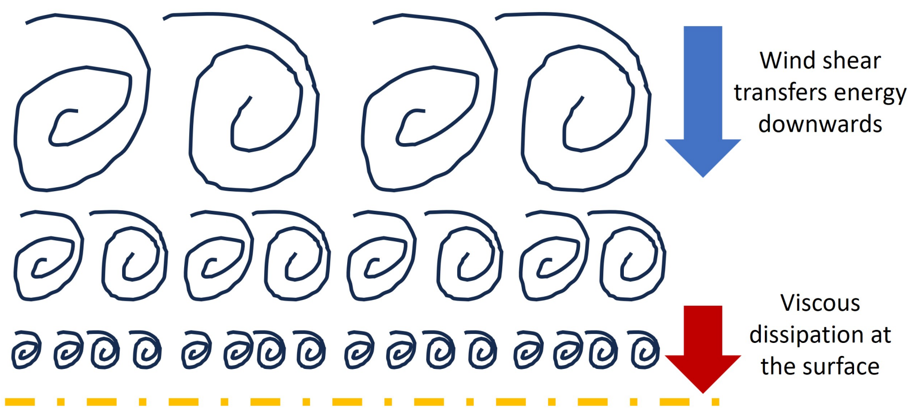

Figure 2.7: The general energy dissipation scheme in turbulent flow where larger eddies transfer energy into smaller ones in cascading manner until it is dissipated at the bed surface.

This *cascade* behavior (Fig. (2.7)) was first proposed by [Richardson, 1922] and later formalized by the Kolmogorov in his seminal theory [Kolmogorov, 1941] which provides insights into the length scales involved in the turbulent flow. Kolmogorov hypothesized a length scale on the smallest scales, referred to as the Komogorov length scale η given by,

$$\eta = \left(\frac{\nu^3}{\epsilon}\right)^{1/4} \tag{2.48}$$

where ν is the kinematic viscosity and ϵ is the energy dissipation rate. This length scale represents the size of the smallest eddy in the turbulent cascade. Kolmogorov's theory also provides expressions for the energy spectrum in the inertial subrange (range of scales between large and small),

$$E(k) = C_k \epsilon^{2/3} k^{-5/3} \tag{2.49}$$

where C_k is the Kolmogorov constant.
The Kolmogorov timescale τ_η is,

$$\tau_\eta = \left(\frac{\nu}{\epsilon}\right)^{1/2} \tag{2.50}$$

In addition to the Kolmogorov length scale, a Taylor microscale T_L describes the spatial structures and interactions between eddies at different scales within the turbulent boundary layer.

$$T_L = \sqrt{\frac{15\nu}{\epsilon}} \tag{2.51}$$

Stochastic description of Lagrangian turbulence

With the DEM model, coupling turbulence into mean field is best achieved by a *stochastic Lagrangian* scheme [Sawford, 1991]. The information of the wind fluctuation is carried by the discrete particles, and a random-walk path is computed for each grain at subsequent time-steps (later described in detail in Section (5.2.5) as turbulent fluctuations are more relevant at the dust scale.

Chapter 3

Numerical methodology

The numerical implementation is achieved using an open-source software package, LAMMPS [Thompson et al., 2022] widely used in the molecular dynamics community. It is short for Large-scale Atomic/Molecular Massively Parallel Simulator, with a scalable design to model large systems easily. The early 21st century has had a significant advancement in computing resources, allowing us to implement complex systems such as the aeolian sand transport using discrete element methods. Fig. (3.1) describes the overview of the entire numerical set-up, at every iterative timestep. The initial positions/velocities are fed into the DEM module, which compute the inter-particle forces as well as the force the wind comes from the CFD module. As discussed in Section (2.4), this momentum exchange results in a negative feedback to the wind, essentially slowing it down. The particle positions/velocities and the modified wind profile is thus available as the feed for the next step of iteration.

3.1 Discrete Element Method (DEM)

DEM is a close relative of Molecular Dynamics (MD) simulations which is a computational technique to model atomic/molecular systems. The familiarity is with computing the forces/interatomic potentials to update the po-

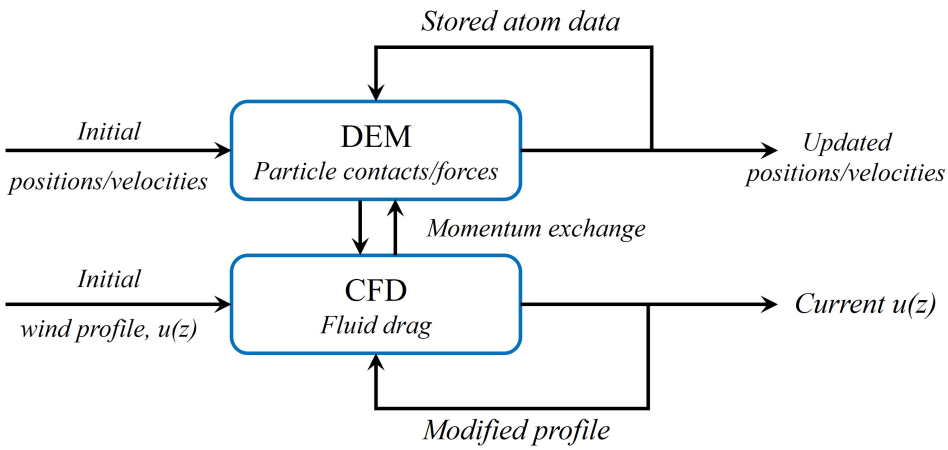

Figure 3.1: A schematic diagram describing the general work-flow of the numerical implementation. The DEM-CFD coupling along with the feedback loops of data involving the particle or wind.

sitions or velocities of particles, while the stark difference lies in the rigorous use of distinct particles and their contact mechanics in the case of DEM simulations. It is generally employed to model granular systems like soil, food grains, pharmaceutical powders, and a variety of different scientific/engineering applications. The interactions are usually modeled using the first principles of contact mechanics and numerically integrated by solving the Newton's equations of motion [Cundall and Strack, 1979]. Here in particular, in contrast to the various numerical models for soil erosion [Anderson and Haff, 1988, Almeida et al., 2008, Kok and Renno, 2009], DEM models do not rely on splash functions to describe the particle ejection from the bed. They are directly computed as a result of the numerical computation of the individual particle-particle interactions in the bed and above (Fig. (3.2)). This means that the mid-air collisions are not neglected, which have a significant impact on the transport flux [Carneiro et al., 2013] and can be easily employed to simulate chaotic systems. In a set-up such as this, a particle can make an impact into the granular bed, redistribute energy and lose momentum and gain it back again from the wind, agglomerates can form and break all in a split-micro second and the DEM simulations can perfectly capture all these features involved with aeolian sand transport.

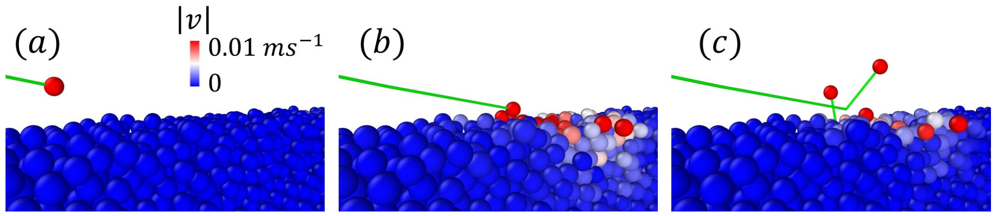

Figure 3.2: A granular bed impact process visualized through DEM simulations. An incident particle in (a) on impact in (b) redistributes the kinetic energy to eject a particle in the process (c)

This chapter provides an overview into the following major aspects -

1. Solving the Newton's equations of motion and the algorithm involved
2. Contact mechanics
3. Neighborhood lists for computing inter-particle forces
4. Parallel computing and the communication interface

3.1.1 Equations of motion

The Newton's equation of translational motion for a particle of mass m_i at position $\mathbf{r}_i$ reads,

$$m_i \ddot{\mathbf{r}}_i = \mathbf{F}_i^{\mathrm{d}} + \mathbf{F}_i^{\mathrm{l}} + m_i \mathbf{g} + \sum_{\substack{1 \le j \le N_{\mathrm{p}} \\ j \ne i}} (\mathbf{F}_{ij}^{\mathrm{ip}} + \mathbf{F}_{ij}^{\mathrm{c}}) \tag{3.1}$$

where $\mathbf{F}_i^{\mathrm{d}}$ and $\mathbf{F}_i^{\mathrm{l}}$ the drag and lift forces the action of wind applies on particle i, described in Section (2.3), $\mathbf{g}$ is the gravitational acceleration, N_{p} is the total number of particles in the system, j denotes the index of a neighbouring particle that is in contact with particle i, $\mathbf{F}_{ij}^{\mathrm{ip}}$ denotes the inter-particle contact force and $\mathbf{F}_{ij}^{\mathrm{c}}$ is the cohesive interaction expressed as van der Waals force exerted by particle j on i (with $\mathbf{F}_{ij}^{\mathrm{ip}} = -\mathbf{F}_{ji}^{\mathrm{ip}}$ and $\mathbf{F}_{ij}^{\mathrm{c}} = -\mathbf{F}_{ji}^{\mathrm{c}}$).

The equation of rotational motion for particle i reads

$$I_i \boldsymbol{\omega}_i = \sum_{\substack{1 \le j \le N_\mathrm{p} \\ j \ne i}} \mathbf{M}_{ij} \tag{3.2}$$

with $I_i = m_i d_i^2/10$ and $\boldsymbol{\omega}_i$ denoting the moment of inertia and the angular velocity of particle i, respectively, and $\mathbf{M}_{ij}$ corresponding to the torque on particle i associated with $\mathbf{F}^\mathrm{c}_{ij,\mathrm{t}}$.

3.1.1.1 Velocity-Verlet integration

The Eqn. (3.1) is iteratively solved to obtain updated positions and velocities and can be rewritten as,

$$m_i \ddot{\mathbf{r}}_i = \mathbf{F}_i \tag{3.3}$$

where $\mathbf{F}_i$ is the total force on i, the velocity-verlet algorithm [Martys and Mountain, 1999] which can be derived from the Taylor series expansion, can then be used for an efficient numerical integration. The algorithm applied on a typical iteration step n, given the particle i's known position $(\mathbf{r}_i^n)$, velocity $(\mathbf{v}_i^n)$ and acceleration $(\mathbf{a}_i^n)$ is as follows -

$$\mathbf{v}_i^{n+\frac{1}{2}} = \mathbf{v}_i^n + \frac{1}{2}\mathbf{a}_i^n \Delta t \tag{3.4}$$

which computes the velocity at half the time-step using current velocities and accelerations.

$$\mathbf{x}_i^{n+1} = \mathbf{x}_i^n + \mathbf{v}_i^{n+\frac{1}{2}} \Delta t \tag{3.5}$$

Eqn. (3.4) in (3.5) gives,

$$\mathbf{x}_i^{n+1} = \mathbf{x}_i^n + \mathbf{v}_i^n \Delta t + \frac{1}{2}\mathbf{a}_i^n \Delta t^2 \tag{3.6}$$

From the updated position $\mathbf{x}_i^{n+1}$, the acceleration information can be gained from the force computations at step $(n+1)$,

$$\mathbf{a}_i^{n+1} = f(\mathbf{x}_i^{n+1}) \tag{3.7}$$

Finally the velocities are calculated from the known $\mathbf{a}_i^{n+1}$,

$$\mathbf{v}_i^{n+1} = \mathbf{v}_i^n + \frac{1}{2}(\mathbf{a}_i^n + \mathbf{a}_i^{n+1})\Delta t \tag{3.8}$$

Modeling the forces involved

The equations for motion as prescribed by Eqn. (3.1) are explored in this section. We describe the elastic inter-particle contact forces ($\mathbf{F}_{ij}^{\mathrm{ip}}$) here, while cohesive interaction modeled by the van der Waals force ($\mathbf{F}_{ij}^{\mathrm{c}}$), the drag force applied by wind ($\mathbf{F}_i^{\mathrm{d}}$) and finally the lift forces ($\mathbf{F}_i^{\mathrm{l}}$) were briefly described in Section (2.3).

3.1.2 Contact mechanics

Contact between particles j and i occurs with their center-to-center distance is smaller than the sum of their radii, i.e., the contact force acts only if the particles overlap. The overlap distance is defined as,

$$\delta_{ij,\mathrm{n}} = \max\left\{0, \frac{1}{2}\left[d_i + d_j\right] - (\mathbf{r}_i - \mathbf{r}_j)\cdot \mathbf{e}_{ij,\mathrm{n}}\right\} \tag{3.9}$$

where d_i and d_j are the diameters of particles i and j, respectively, $\mathbf{r}_{ij} = \mathbf{r}_i - \mathbf{r}_j$, with $\boldsymbol{r}_j$ standing for the position of particle j, and $\mathbf{e}_{ij,\mathrm{n}} = \mathbf{r}_{ij}/r_{ij}$ denotes the normal unit vector pointing from the center of particle j to the center of particle i, with $r_{ij} = |\mathbf{r}_{ij}|$. All the particles in this work are assumed to be spherical, and do not fragment during the transport. When in contact they allow for an overlap as shown in Fig. (3.3).

There are various contact force models for application in DEM simulations, and the modelling of these forces is still an active matter of research [Cundall and Strack, 1979, Shäfer et al., 1996, Brilliantov et al., 1996, Silbert et al., 2001, Di Renzo and Di Maio, 2004, Pöschel and Schwager, 2005, Kruggel-Emden et al., 2007, Luding, 2008, Machado et al., 2012, Parteli et al., 2014b, Fan et al., 2017, Schmidt et al., 2020, Santos et al., 2020]. In my simulations, the linear spring-dashpot model is adopted, as this model has been employed

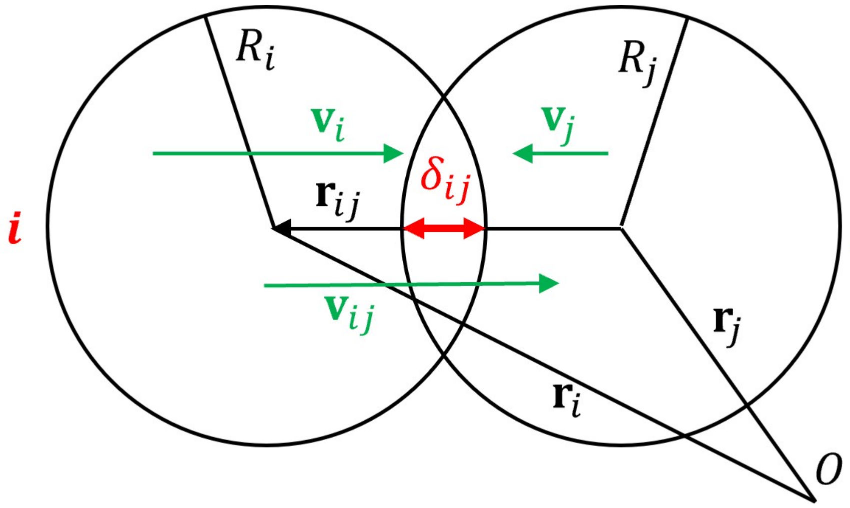

Figure 3.3: The particles overlap over a short distance which depends on the approach velocity and also the elastic and damping constants (indirectly on the restitution coefficient) in the normal direction

in previous simulations of wind-blown sand that reproduced the scaling laws associated with Aeolian transport over fully erodible sand beds [Carneiro et al., 2011, 2013, Durán et al., 2012, Comola et al., 2019]. The linear law is based on Hooke's law, and is the simplest model for elastic contacts, which states that the repulsive contact force scales linearly with the overlap distance defined by Eq. (3.9). On the contrary, it should be noted that more accurate non-linear contact models like Hertz-Mindlin [Parteli et al., 2014b] was not explored in this aspect because of the additional computational expense, and could be explored in the future.

Specifically, $\mathbf{F}_{ij}^{\mathrm{ip}}$ can be described as the sum of a normal component, $\mathbf{F}_{ij,\mathrm{n}}^{\mathrm{ip}}$, and a tangential component, $\mathbf{F}_{ij,\mathrm{t}}^{\mathrm{ip}}$, where the spring-like behavior is depicted in Fig. (3.4). Each of these components encodes an elastic term and a dissipative term, while the magnitude of the tangential force is bounded by the Coulomb friction criterion. The equations for $\mathbf{F}_{ij,\mathrm{n}}^{\mathrm{c}}$ and $\mathbf{F}_{ij,\mathrm{t}}^{\mathrm{c}}$ read [Cundall and Strack, 1979, Silbert et al., 2001, Santos et al., 2020]

$$\mathbf{F}_{ij,\mathrm{n}}^{\mathrm{ip}} = k_{\mathrm{n}}\delta_{ij,\mathrm{n}}\mathbf{e}_{ij,\mathrm{n}} - \gamma_{\mathrm{n}} m_{\mathrm{eff}}\mathbf{v}_{ij,\mathrm{n}} \tag{3.10}$$

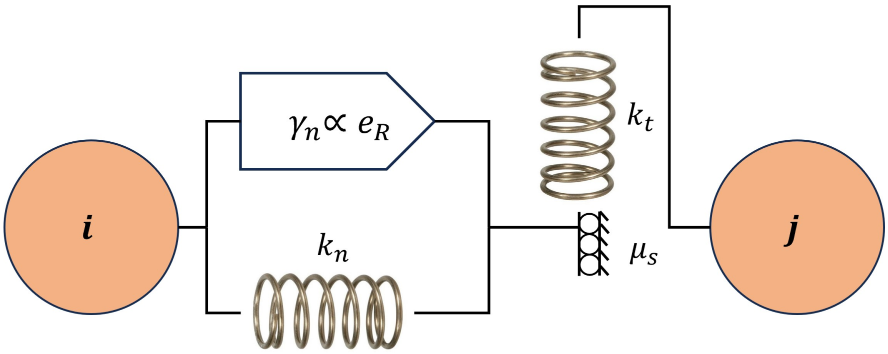

Figure 3.4: The elastic contact depicted as a spring, comprising of a normal component and a tangential component, following a Coulomb friction criterion. Figure modified from [Kneib et al., 2015]

$$\mathbf{F}^{\text{ip}}_{ij,\text{t}} = -\min\Big\{\mu_\text{s}|\mathbf{F}^{\text{ip}}_{ij,\text{n}}|, k_\text{t}\xi_{ij,\text{t}} + \gamma_\text{t} m_\text{eff}|\mathbf{v}_{ij,\text{t}}|\Big\}\frac{\mathbf{v}_{ij,\text{t}}}{|\mathbf{v}_{ij,\text{t}}|} \tag{3.11}$$

where $m_\text{eff} = m_i m_j/(m_i + m_j)$, with m_i and m_j denoting the masses of particles i and j, respectively, k_n, k_t, γ_n, γ_t and μ_s are model parameters, discussed in Section (3.2) below, while the relative normal velocity $\mathbf{v}_{ij,\text{n}}$ and the relative tangential velocity $\mathbf{v}_{ij,\text{t}}$ between particles i and j are computed via

$$\mathbf{v}_{ij,\text{n}} = (\mathbf{v}_{ij} \cdot \mathbf{e}_{ij,\text{n}})\mathbf{e}_{ij,\text{n}} \tag{3.12}$$

$$\mathbf{v}_{ij,\text{t}} = \mathbf{v}_{ij} - \mathbf{v}_{ij,\text{n}} - \frac{1}{2}(\boldsymbol{\omega}_i + \boldsymbol{\omega}_j) \times (\mathbf{d}_i - \mathbf{d}_j) \tag{3.13}$$

with $\mathbf{v}_{ij} = \mathbf{v}_i - \mathbf{v}_j$ denoting the difference between the velocities of particles i and j ($\mathbf{v}_i$ and $\mathbf{v}_j$, respectively), and $\boldsymbol{\omega}_i$ and $\boldsymbol{\omega}_j$ standing for their respective rotational velocities. Moreover, in Eq. (3.11), $\xi_{ij,\text{t}}$ is the tangential displacement accumulated as the particles are in contact. The displacement is set as zero at initiation of the contact and is computed in the reference frame of the rotating particle pair to compensate for the effect of rigid body rotations, as described in detail in previous work [Silbert et al., 2001, Santos et al., 2020].

3.1.3 Neighbor/verlet lists

As can be inferred from the Section (3.1.2), the force computations take up a significant fraction of the computation time. With no long-range interactions in the system, it makes no sense to compute force potentials between all the pairs ($\mathcal{O}(N_\mathrm{p}^2)$). It is then reasonable to perform force computations for particles within a specified cutoff distance, which greatly brings down the computational overhead to $\mathcal{O}(N_\mathrm{p}N_\mathrm{m})$. Here m is the mean number of particles in a neighbor list, and typically $N_\mathrm{m} << N_\mathrm{p}$. For each particle i, we build so called neighborhood lists which at any given iteration stores information about the immediate neighbors (Fig. 3.5). If R_f is the largest force cutoff distance and Δ_s is the so called "skin" distance, which conducts the frequency of building neighbor lists, then we define the neighbor cutoff distance as,

$$R_\mathrm{n} = R_\mathrm{f} + \Delta_\mathrm{s} \tag{3.14}$$

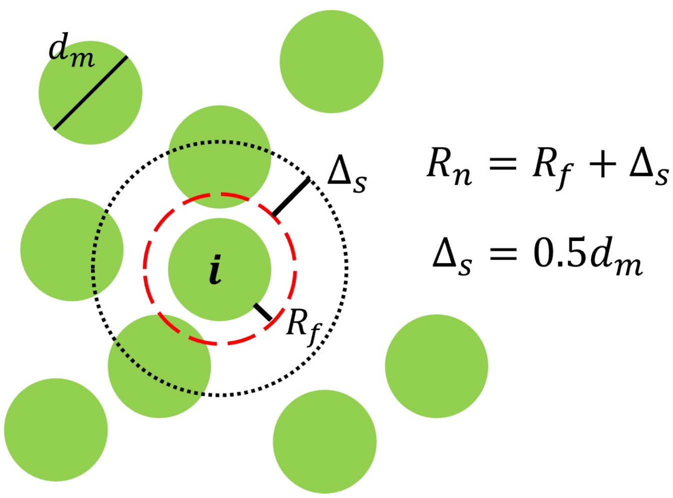

Figure 3.5: Every particle has its own neighbor list built to keep track of the potential neighbors to compute force interactions.

In the present work, R_f is the one imposed for the van der Waals interaction which is set at a particle surface-to-surface distance of $1\mu m$. Owing to the small timesteps, the particles do not move large distance in between iterations. The skin distance allows us to dictate a protocol, which triggers the rebuilding of the list if any particle has moved half the skin distance since the time a list was built for that particle. While a large Δ_{s} builds the lists less often, but would increase the potential pairs to be checked for every iteration. On the other hand, with a small Δ_{s}, only a few pairs need to be checked for potential interactions but this would drastically increase the burden of building lists more frequently. For the case of slightly polydisperse systems like the one used in our sand tranport simulations, ($\Delta_{\mathrm{s}} = 0.5d_{\mathrm{max}}$), where d_{max} is the largest diameter in the simulation.

3.1.4 Linked-cell lists

The linked-cell method adds a further layer of optimization to build the neighbor lists. The list information is stored in data structures which can be efficiently used to both access and update the lists. In this method, the entire domain is divided into bins of equal volume ($R_{\mathrm{f}} \times R_{\mathrm{f}} \times R_{\mathrm{f}}$) as shown in a 2D simplified representation in Fig. (3.6). Each of the bin has a pointer stored with information of the particles present in the bin shown in Fig. (3.6a), which is updated as the particles move from one bin to another as described in Fig. (3.6b).

Using the linked-cell method along with the neighbor/verlet list method depicted in Section (3.1.3), i.e., using the linked-cell lists to build the neighbor lists and only performing force computations for particles inside the cutoff (R_{n}) in subsequent non-build steps. This combination significantly speeds up the neighbor build process, which as we understand is one of the major bottlenecks in DEM simulations.

3.1.5 Multi-grid method for polydisperse systems

In the classic linked-cell method described above, the cell size was determined based on the largest grain in the system domain. This leads to a considerably higher computational effort for highly polydisperse dense granular media.

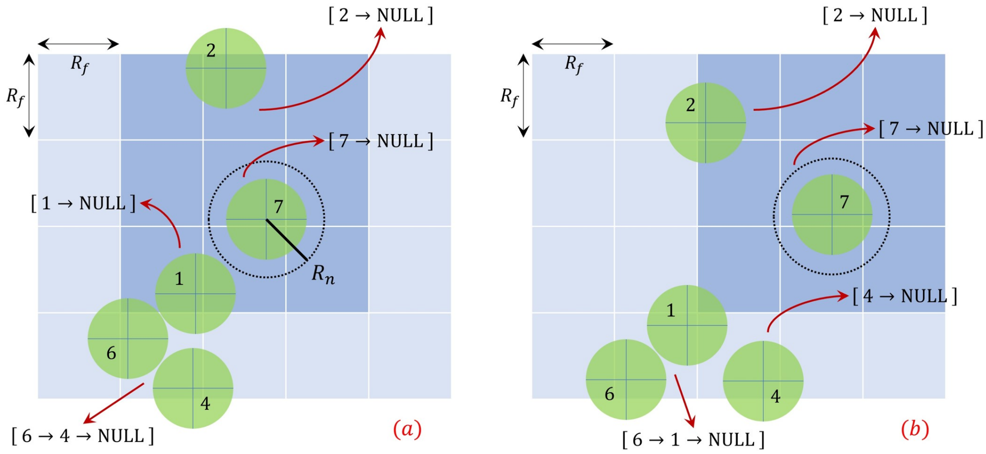

Figure 3.6: The system is divided into equal sized 3D bins, and as the lists are built the linked-cell algorithm updates the pointers atached to each bin. Only the shaded bins which are adjacent to the particle of interest are considered.

The multi-grid method is based on one of the most recent algorithms to improve building neighbor lists for highly polydisperse systems [Shire et al., 2021]. This kind of an approach has been previously proposed by [Ogarko and Luding, 2012, Weinhart et al., 2020], while [Shire et al., 2021] was the first attempt at integrating it into LAMMPS. In Fig. (3.7a), it can be seen as to how the previous method of building equal size bins for linked-cell method could lead to extreme increase in the build pairs owing to high size-ratios. Instead of choosing the largest particle diameter as the bin size, we could define multi-layered bin sizes for various collections of particle sizes.

This hierarchical approach can be seen as a multi-level contact method [Weinhart et al., 2020] as shown in Fig. (3.7b). It can be interpreted as an overlay of bins, which have an added communication interface to pass information on the particle location. The algorithm approaches the neighborhood search in 2 stages -

(i) Mapping - This hierarchical grid (H_h) is made of L levels, h $\in$ [1,L]. $\omega = r_{max}/r_{min}$ is the extreme size ratio used to optimally set the levels depending on the particle size distribution.

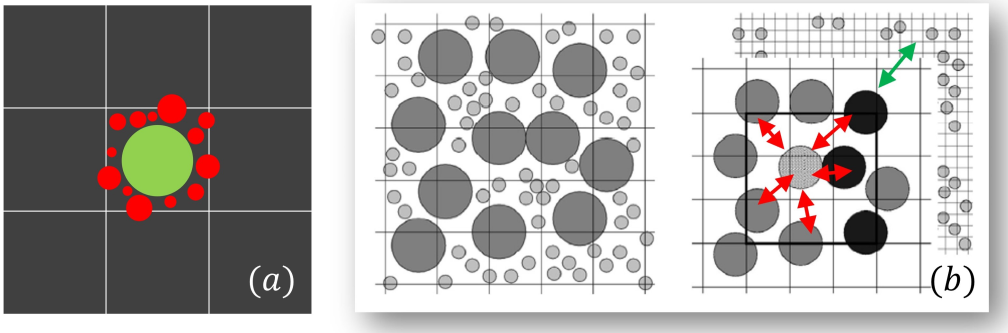

Figure 3.7: (a) The largest grain determining the cell size in the linked-cell method, this is at a disadvantage for polydisperse systems, (b) The multi-level contact method tackles this by mapping and contact searching across the levels (extracted from [Weinhart et al., 2020]).

Cell sizes in each levels (s_h) are thus set as a function of the size distribution as follows:

$$\begin{aligned}(s_{h,min}, s_{h_max}) &= (2r_{min}, 2r_{max}) \\ h\,(p) &= \min_{1 \leq h < L} h : s_h \geq 2r_p\end{aligned} \tag{3.15}$$

(ii) Contact detection - This is realized in the following way:

(a) At the level of insertion : This is similar to the classical linked-cell method, for the particles placed at the same level shown by the red arrows in Fig. (3.7b).

(b) Cross-level check : The contact detection search is now across levels (green arrow Fig. (3.7b)), but only the levels hierarchically below the current level are considered. In the representative figure in Fig. (3.8) this means that only particles smaller than 'B' are searched. The cells are chosen at all lower hierarchical levels defining a search box,

$$(x, y, z)_B \pm (r_p + 0.5s_h) \tag{3.16}$$

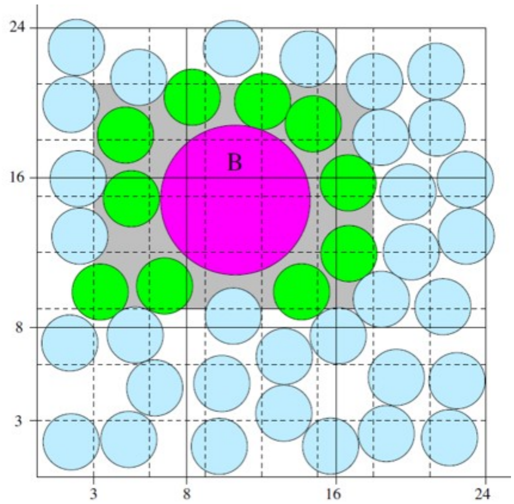

Figure 3.8: The contact detection in the multi-grid method. The search around grain B (pink) across the level for blue grains, would detect green grains according to the algorithm (extracted from [Ogarko and Luding, 2012].

3.2 Parameter estimation

For a spherical particle with diameter d_{m}, density ρ_{p} and a Young's modulus value of $Y = 1\,\mathrm{MPa}$, which was chosen based on previous DEM models for aeolian sand transport [Carneiro et al., 2011, Comola et al., 2019]. Choosing a low stiffness parameter, has it's own advantage with lower computation times. However, it is to be noted that this might allow for slight discrepancies, while modeling dust grains. But we believe that the qualitative result would not defer much since we take care of the reduced effect of cohesion (as a correction for soft-DEM approach) which we explain in Section (5.2.1).

For small stress/strains, and with a linear elastic assumption, Young's modulus acts as a proportional quantity for the strain (ε) felt with an applied stress (σ).

$$Y = \frac{\sigma}{\varepsilon} = \frac{\text{Force/Area}}{\Delta L / L_0} \tag{3.17}$$

For simplification, if we assume only the normal elastic force applied over the cross-sectional area of the particle with a characteristic length, $L_0 = d_{\mathrm{m}}$, causing a deformation of δ (which is the overlap distance), the normal elastic constant, k_{n} can be given as,

$$k_{\mathrm{n}} = \frac{\pi d_{\mathrm{m}} Y}{4} \tag{3.18}$$

where d_{m} is the mean diameter of the particles in contact. This is particularly valid for slight polydispersity in the system. However with polydisperse systems, we perform the similar computations, while using a effective value for diameter and mass as a Harmonic mean of the quantities, $d_{\mathrm{eff}} = (d_i d_j)/(d_i + d_j)$ and $m_{\mathrm{eff}} = (m_i m_j)/(m_i + m_j)$

The tangential elastic constant (k_{t}) chosen as a fraction of k_{n} reads,

$$k_{\mathrm{t}} = \frac{k_{\mathrm{n}}}{3} \tag{3.19}$$

As for the damping parameters, we fix the energy dissipation using the coefficient of restitution (e_{r}) which is essentially the ratio between the velocities before and after the collision. By describing the contact process as a damped harmonic oscillator, we could make use of the half-time-period to compute both the damping constants and the time for collision (t_{c}) as follows [Luding, 1998, 2008] –

A typical half-period of the vibration, which is the collision time is given as,

$$t_{\mathrm{c}} = \frac{\pi}{\omega}, \text{ with } \omega = \sqrt{\left(\frac{k_{\mathrm{n}}}{m_{\mathrm{eff}}}\right) - \left(\frac{\gamma_{\mathrm{n}}}{2}\right)^2} \tag{3.20}$$

The coefficient of restitution (e_{r}) as a function of the contact time (t_{c}) and the normal damping constant (γ_{n}) can be expressed as,

$$e_{\mathrm{r}} = \exp\left(\frac{-t_{\mathrm{c}}\gamma_{\mathrm{n}}}{2}\right) \tag{3.21}$$

Eqns. (3.20 & 3.21) can be simultaneously solved to end up with expressions for $\gamma_{\rm n}$ and $t_{\rm c}$ as just a function of known parameters.

$$\gamma_{\rm n} = \sqrt{\frac{4k_{\rm n}}{m_{\rm eff}\left[1+\left(\frac{\pi}{\ln e_{\rm r}}\right)^2\right]}} \tag{3.22}$$

Note that the normal damping constants for the particle-particle and the particle-wall interaction would differ due to the way $m_{\rm eff}$ is defined. That is $m_{\rm eff} = m_i/2$ for the former, while $m_{\rm eff} = m_i$ for the latter (the wall is treated as an infinite mass). The tangential damping constant ($\gamma_{\rm t}$) in Eqn. (3.11) is equal to the respective normal damping components.

To compute the timestep (Δt) for the simulations, it is sufficient to take it as $\Delta t = t_{\rm c}/20$. Eqn. (3.20) then implies,

$$\Delta t = \frac{\pi}{20}\left[\left(\frac{k_{\rm n}}{m_{\rm eff}}\right) - \left(\frac{\gamma_{\rm n}}{2}\right)^2\right]^{(-1/2)} \tag{3.23}$$

When computing the time-step during the simulations, the $m_{\rm eff}$ is the effective mass considered for the contact between the smallest particles in the system. These parameters are validated in subsequent Chapters (4 and 5).

3.3 Speed-up scheme and performance

A two-way speed-up of the numerical model is explored in this section; comprising of a horizontal x-level parallelization and a vertical z-level grid coarsening. This section is taken from the proceedings paper [Kamath and Parteli, 2021].

3.3.1 Parallelization

The spatial decomposition of only the x-domain can be easily achieved in LAMMPS. The underlying MPI (Message Passing Interface) code is modified to accommodate the wind coupling as to have a more robust bed evolution. Fig. (3.9) shows the similar behavior for a run with a single processor and that

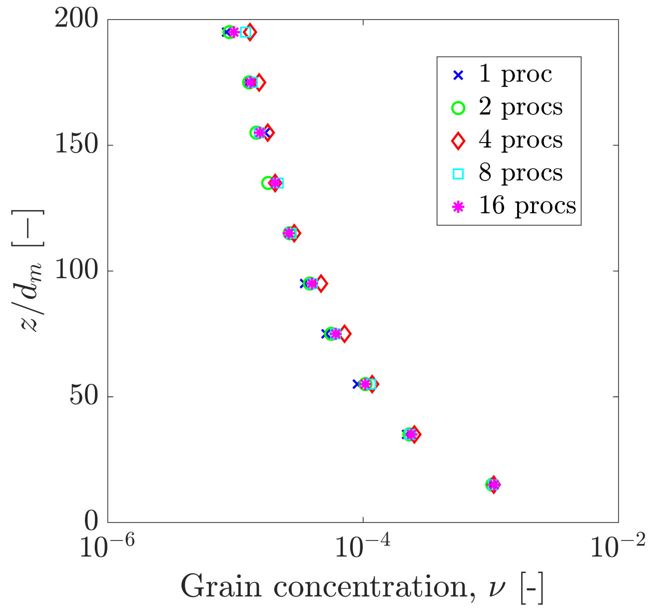

Figure 3.9: Sand flux profile over the bed height plotted for varying number of processors used

for parallel runs, and shows the validity of the model with just an acceptable loss in accuracy. The computation time is greatly reduced with more number of processors, although with an increase in communication times as well.

3.3.2 Grid coarsening

The vertical z-level coarsening is implemented with the previous z-grid thickness of the mean particle diameter (d_m) is increased gradually over z. The grain concentration is known to be exponentially decreasing with height away from the bed [Creyssels et al., 2009].

We propose a quadratic sequence for the increase in the grid spacing. Previously, the grid height was given by:

$$z_n = h_0 + (n - 1)d_m \tag{3.24}$$

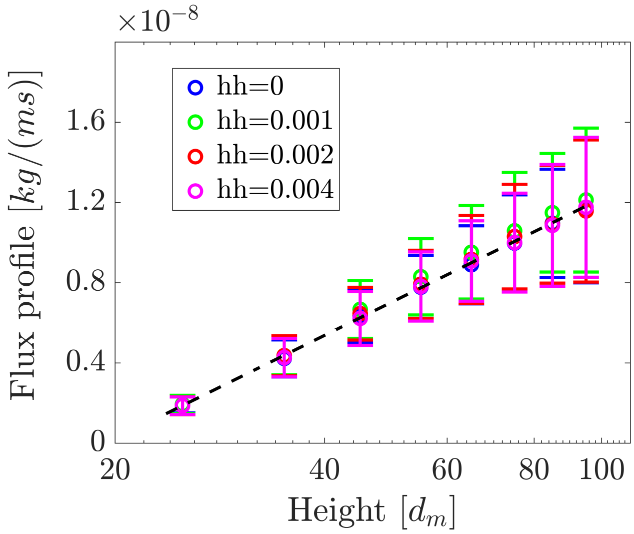

Figure 3.10: Sand flux profile plotted for varying grid spacing

In the new scheme,

$$z_n = h_0 + An^2 + Bn \tag{3.25}$$

where, $A = hh/2$ and $B = (1 - hh/2)$, with $hh = \Delta z - d_m$ The validity of this coarsened model is checked using the sand flux profiles over height (Fig. (3.10)).

The computational aspect of both the parallelized and coarsening scheme is summarized in Fig. (3.11) and indicates the reduced computational cost in the speed-up model.

The developed tool is equipped with efficient parallelization schemes for the existing aeolian transport models. Although prevalent in granular research, our wind-coupled DEM model in LAMMPS, packed with extensive features is new to aeolian/sediment transport applications. After careful validations with experiments, we provided new additions to the model with a horizontal grid parallelization to accommodate large systems and a vertical grid coarsening method. This grid coarsening away from the bed height finds application for dust transport as the small particles are usually suspended and carried to great heights and would need additional computational effort to model huge vertical systems. The same holds if we intend to model the

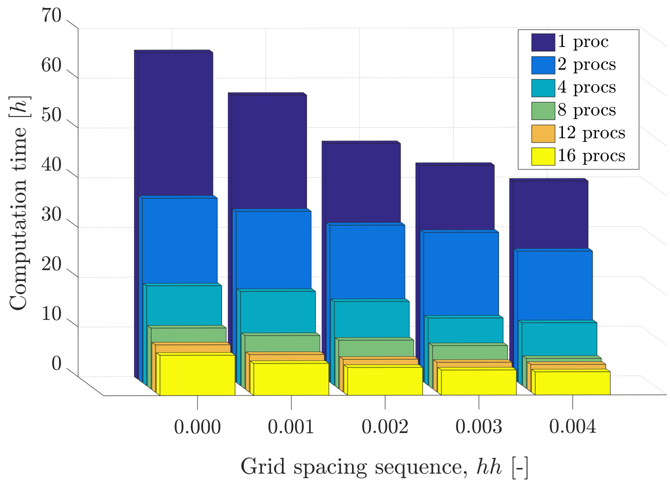

Figure 3.11: Computation time comparison for parallel runs and grid coarsening simulations

transport for low gravity environments like Mars or Pluto.

Since, the above section was just a preliminary analysis to study the effects of grid coarsening on the particle dynamics, I now describe the actual vertical grid schemes used in the subsequent chapters. In Chapter (4), where sand grains of mean diameter, d_m were simulated, I use equal sized grids of size $dz = d_\mathrm{m}$ starting from the bed height. In the later Chapters (5-6) while encountering the dust regime for both monodisperse and bidisperse sand-dust systems, we use the scheme previously prescribed in 2.4.1. That is inside the bed and very close above the surface, dz is held constant at $\min\{\nu/u_*, d_\mathrm{m}\sqrt{1-\phi_\mathrm{b}/\left(18\phi_\mathrm{b}\right)}\}$ and an exponential dz is used from above $h_0 + 5d_1$, where h_0 is the bed height and d_1 is the largest grain diameter in the system.

Chapter 4

Scaling laws in aeolian sand transport

The first part of this chapter is dedicated to discuss the scaling behavior of the sand transport flux with varying atmospheric conditions, specifically the wind intensity. We shed light on the evolution of the scaling equations which began with Bagnold in the 1940s, to recent observations owing to numerical and experimental advancements. In the later, half I present an extrapolation of the study for low sand-availability conditions which is taken from *Kamath, S. et al., 2022. Scaling laws in Aeolian sand transport under low sand availability. Geophysical Research Letters, 49(11)* [Kamath et al., 2022].

4.1 Aeolian saltation

Aeolian saltation as described before in Section (2.1), is a fundamental process in geomorphology, significantly impacting the transport of sediment and the development of various landforms in arid and semi-arid environments. This process begins when the wind reaches a critical velocity ("Fluid threshold", $u_{*,\mathrm{ft}}$) that can overcome the gravitational and other inter-particle forces holding sand-sized particles on the ground, causing them to be lifted into

the air. These particles then follow a series of short, hopping trajectories, bouncing along the surface in a motion that can dislodge other grains upon impact, leading to a cascading transport effect [Bagnold, 1941]. Once initiated through fluid drag or a few impact splashes, the grain concentration in the saltation layer initially increases exponentially, and is sustained above what is referred as the "dynamic/impact threshold $u_{*,\mathrm{it}}$". Note the two distinct definitions of the transport thresholds, and on Earth $u_{*,\mathrm{it}} < u_{*,\mathrm{ft}}$ as the transfer of momentum is efficient by splash mechanisms than the wind [Kok et al., 2012].
Aeolian saltation is not only a major driver in the formation of dunes and ripples but also plays a crucial role in dust storm formation, desertification, and the global sedimentary cycle [Nickling and Neuman, 2009, Kok et al., 2012]. The study of this process is essential for understanding how wind-driven sediment dynamics influence ecological systems, agricultural productivity, and human infrastructure, particularly in regions prone to desertification and dust emission events [Shao, 2008, Bullard et al., 2016]. By examining the mechanics and impacts of aeolian saltation, researchers can develop more effective strategies for land management and erosion control, which are increasingly important in the context of climate change and expanding desert areas [Parteli, 2022b].

4.2 Sand flux - wind dependency

[Bagnold, 1941] derived the mass flux of grains from the momentum balance between the grains and the fluid, and assuming an average lift-off and impact velocity, ended up with the following equation -

$$Q = c_0 \frac{\rho_f}{g} u_*^3 \tag{4.1}$$

Since Bagnold, over the last few decades, numerous theoretical and experimental studies have been presented to achieve accurate transport scaling. It was largely accepted that the horizontal sand flux follows a cubic scaling

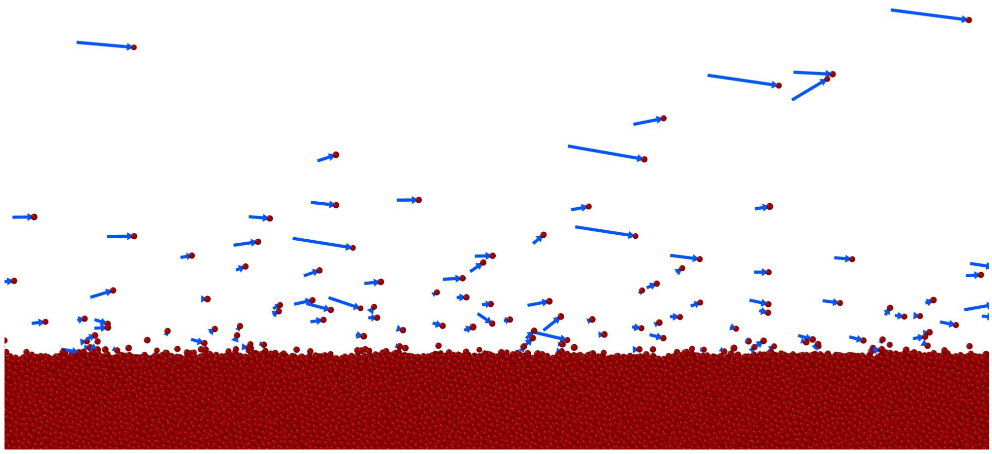

Figure 4.1: A DEM simulation snapshot showing the saltation phenomenon with the arrows symbolizing the grain velocities, indicating the grains achieve higher speeds as they rise and decelerate as they fall

with the u_* as is summarized in Table. (4.1).

However in recent times, it has been shown from extensive experiments as well as theory that, for nominal wind speeds it is a quadratic scaling, while this transitions into a quartic scaling for higher wind speeds. [Ungar and Haff, 1987] first speculated the quadratic scaling, by noting that the wind speed close to the bed is affected by the saltating particles resulting in a negative feedback to the wind. [Anderson and Haff, 1988, 1991] first used the DEM simulations to include this feedback mechanism, also realizing the grain collisions during the splash process.

[Beladjine et al., 2007, Oger et al., 2008] conducted splash experiments which helped improve the splash functions describing the particle impact/ejection velocities and various rebound characteristics like the restitution coefficient. [Creyssels 2009] provided some influential observations in their experiments bringing the scope of particle image/tracking velocimetry [PIV, PTV] which confirmed the non-dependency of the mean wind speeds on the impacting/ejecting grain velocities, that is attributed to the reduction in the wind profile due to the momentum feedback.

This observation marks the difference between the older models with the

Study	Equation for sand mass flux	Parameters
[Bagnold, 1941]	$Q_{\mathrm{B}} = C_{\mathrm{B}} \left(d_{\mathrm{m}}/d_{250} \right)^{0.5} \rho_{\mathrm{a}} u_*^3/g$	Row 1, $C_{\mathrm{B}} = 1.5 - 2.8$ depending on the soil
[Kawamura, 1951]	$Q_{\mathrm{K}} = C_{\mathrm{K}} \rho_{\mathrm{a}} u_*^3/g \left(1 - u_{*,\mathrm{it}}^2/u_*^2\right) \left(1 + u_{*,\mathrm{it}}/u_*\right)$	$C_{\mathrm{K}} = 2.78$ or 2.61 [White 1979]
[Owen, 1964]	$Q_{\mathrm{O}} = \rho_{\mathrm{a}} u_*^3/g \left(0.25 + v_{\mathrm{t}}/(3u_*)\right) \left(1 - u_{*,\mathrm{it}}^2/u_*^2\right)$	v_{t} is the terminal velocity
[Lettau, 1978]	$Q_{\mathrm{L}} = C_{\mathrm{L}} \left(d_{\mathrm{m}}/d_{250} \right)^{0.5} \rho_{\mathrm{a}} u_*^3/g \left(1 - u_{*,\mathrm{it}}/u_*\right)$	$C_{\mathrm{L}} = 6.7$
[Ungar and Haff, 1987]	$Q_{\mathrm{U}} = C_{\mathrm{U}} \rho_{\mathrm{a}} \left(D_{\mathrm{P}}/g \right)^{0.5} u_*^2 \left(1 - u_{*,\mathrm{it}}^2/u_*^2\right)$	C_{U} unavailable
[Sørensen, 2004]	$Q_{\mathrm{S}} = \rho_{\mathrm{a}} u_*^3/g \left(1 - u_{*,\mathrm{it}}^2/u_*^2\right) \left(\alpha + \gamma u_{*,\mathrm{it}}/u_* + \beta u_{*,\mathrm{it}}^2/u_*^2\right)$	α, β, γ are the parameters describing the saltation hop.
[Durán et al., 2011]	$Q_{\mathrm{D}} = c_{\mathrm{D}} \rho_a u_{*,\mathrm{it}}/g u_*^2 \left(1 - u_{*,\mathrm{it}}^2/u_*^2\right)$	$C_{\mathrm{D}} \approx 5$
Kamath et al. [2022]	$Q = a \left[1 + b \left(u_*/u_{*,\mathrm{it}} - 1\right)\right] \left(d/g\right)^{0.5} \rho_{\mathrm{a}} \left(u_*^2 - u_{*,\mathrm{it}}^2\right)$	a, b depend on the sand thickness

Table 4.1: Evolution of the scaling relations for the sand flux Q and the wind friction velocity u_*. This comparison is extracted from [Kok Parteli 2012], with the addition of the scaling presented in this chapter.

cubic scaling [Kawamura, 1951, Owen, 1964, White, 1979] and that of the ones with the quadratic scaling [Ungar and Haff, 1987, Andreotti, 2004, Durán et al., 2012, Valance et al., 2015]. The recent models follow a splash-dominated saltation models as confirmed by experiments [Ho et al., 2011, Martin and Kok, 2017] and the invariancy of the wind to the saltation heights imply a quadratic scaling of the saltation flux with u_* or a linear scaling with the Shield's number (Θ) which we also obtain in our model validation in the next section. Apart from the particle-based approaches, [Kok et al., 2012, Parteli, 2022a] provide a good overview of the various continuum model approaches towards modeling aeolian dune morphology which would help in large-scale studies of aeolian sand movement [Parteli et al., 2014a, Yizhaq et al., 2009].

4.2.1 Model validation

The DEM implementation and the coupling with the fluid dynamics are illustrated in Chapters (2,3). As saltation is the basic process which ultimately dictates most of the global dust emission, we simulate fully erodible, cohesionless 200 μm spheres for various wind speeds ($0.15 - 0.40$ m/s) . A few grains are impacted on to the surface to begin the saltation, and awaited for the transport to reach a steady state. To verify our numerical simulations, we compare our numerical predictions for the height-integrated mass flux (Q) of wind-blown particles over a fully erodible bed with corresponding wind-tunnel observations [Creyssels et al., 2009] of this flux as a function of the wind shear velocity, u_*. We compute Q using the following equation,

$$Q = \frac{\sum_i^N m_i v_i^x}{A} \tag{4.2}$$

where N is the number of particles in the system, m_i and v_i^x denote the mass and horizontal speed of the $i-$th particle, respectively, and $A = L_x \cdot L_y$ is the horizontal area of the simulation domain. To measure this flux, we start the wind-blown transport process as described in the main document and wait until this transport achieves steady state. The typical (physical) time separating the begin of wind-blown transport from the steady state is about 2-3 seconds and independent of u_* [Carneiro et al., 2011, Durán et al., 2012, Pähtz et al., 2014a, Comola et al., 2019]. All results reported in the present work refer to the characteristics of steady-state wind-blown transport, and denote mean quantities obtained from averaging over about 5-10 seconds during steady-state transport.

Furthermore, by suitably normalizing the steady-state flux Q, we obtain the following non-dimensional quantity,

$$\hat{Q} = \frac{Q}{\rho_\mathrm{p}\sqrt{(s-1)gd_\mathrm{m}^3}}, \text{ with } s = \frac{\rho_\mathrm{p}}{\rho_\mathrm{a}}, \tag{4.3}$$

which we plot in Fig. 4.2 as a function of the Shields number,

$$\Theta = \frac{u_*^2\rho_\mathrm{f}}{(\rho_\mathrm{p}-\rho_\mathrm{a})gd_\mathrm{m}} \tag{4.4}$$

where $\rho_\mathrm{p} = 2650\,\mathrm{kg/m^3}$ and $\rho_\mathrm{a} = 1.225\,\mathrm{kg/m^3}$ denote the densities of the particles and the air, respectively, while $d_\mathrm{m} = 200\,\mu\mathrm{m}$ is the mean particle diameter and $g = 9.81\,\mathrm{m/s^2}$ is gravity.

We see in Fig. (4.2) that our numerical predictions for $\hat{Q}(\Theta)$ (circles) agree quantitatively well with observations from wind-tunnel experiments [Creyssels et al 2009], denoted by the stars. The best fit to our simulation results using $\hat{Q} = a\Theta + b$ yields $a \approx 0.5$ and $b \approx 0.0026$ (dashed line in Fig. 4.2), from which obtain the minimal threshold $\Theta_\mathrm{t} \approx 0.0052(u_* \approx 0.15$ m/s) below which no transport occurs ($\hat{Q} = 0$). However, there is a discontinuity and hence a *jump at the onset of saltation* [Carneiro et al., 2011] because of which we do not see continued saltation for wind velocity below $\approx$ 0.165 m/s. This is by definition the minimal threshold wind shear velocity for sustained transport or the impact/dynamic threshold ($u_{*,\mathrm{it}}$).

We note that the value of $u_{*,\mathrm{it}}$ predicted from our simulations is consistent with the prediction that $u_{*,\mathrm{it}}$ is about 80% of the minimal threshold wind

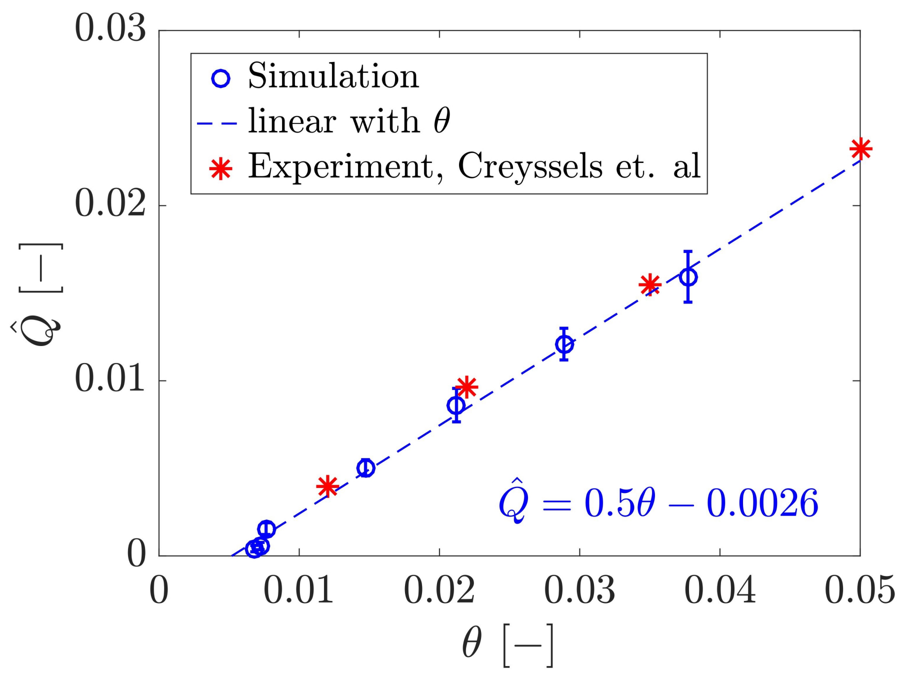

Figure 4.2: Normalized steady-state flux $\hat{Q}$ as a function of the Shields number Θ, considering a fully erodible bed ($\delta_0 \approx 15\, d_\mathrm{m}$).

shear velocity $u_{*,\mathrm{ft}}$ required to initiate transport,

$$u_{*\mathrm{ft}} = A_\mathrm{ft}\sqrt{\frac{\rho_\mathrm{p} - \rho_\mathrm{a}}{\rho_\mathrm{f}} g d_\mathrm{m}}, \tag{4.5}$$

with $A_\mathrm{ft} \approx 0.1$ [Bagnold, 1941, Shao and Lu, 2000]. Indeed, by applying the mean particle size $d_\mathrm{m} = 200\,\mu\mathrm{m}$ of our simulations in Eq. (4.5), we obtain $u_{*,\mathrm{ft}} \approx 0.206\,\mathrm{m/s}$, i.e., our model is consistent with the relation $u_{*,\mathrm{it}} \approx 0.8\, u_{*,\mathrm{ft}}$ predicted for wind-blown transport.

4.2.2 Saltation to Collision regime

[Carneiro et al., 2013] suggested the enhancement of saltation because of mid-air collisions through DEM simulations. Through theory [Durán et al., 2011, Pähtz and Durán, 2020] and experiments [Ralaiarisoa et al., 2020] that at high wind speeds, the transport regime is no more saltation dominated,

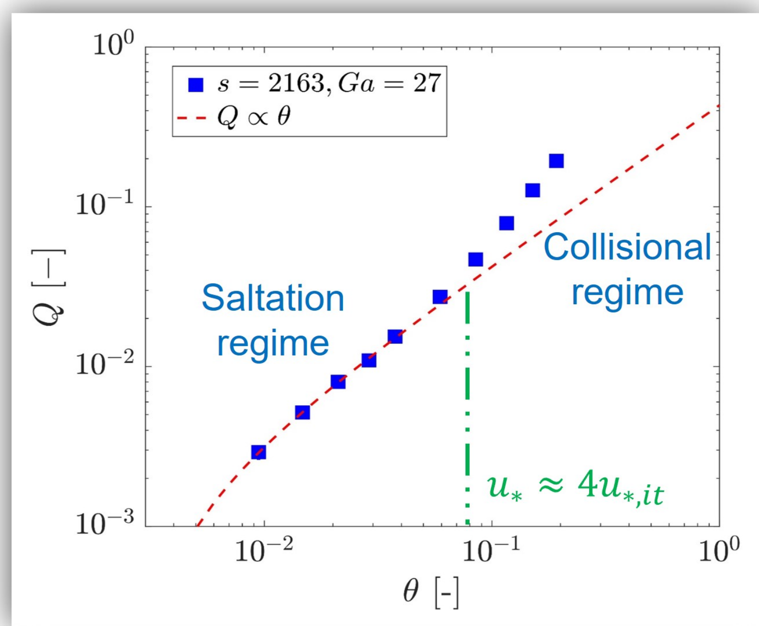

Figure 4.3: Normalized steady-state flux $\hat{Q}$ as a function of the Shields number Θ, we observe the departure of the linear (saltation dominated) to quadratic (collision dominated) scaling of $\hat{Q}$ with Θ.

but enters the collision regime. We confirm this observation using our DEM model, as can be seen in Fig. (4.3) for earth conditions with grain-to-fluid density ratio ($s = 2163$) and a Galileo number ($G = d\sqrt{sgd}/\nu = 27$). The transition occurs at wind velocities around $u_* \approx 4u_{*,\mathrm{it}}$.

[Pähtz and Durán, 2020, 2023] provided a universal scaling towards unifying the fluvial and aeolian sediment transport and provided an expression,

$$\hat{Q} = \frac{2\sqrt{\Theta_t}}{\kappa\mu_\mathrm{b}}(\Theta - \Theta_t)\left[1 + \frac{c_\mathrm{M}}{\mu_\mathrm{b}}(\Theta - \Theta_t)\right] \tag{4.6}$$

where $\mu_\mathrm{b} \approx 0.63$ (an effective coefficient of restitution) and $c_\mathrm{M} \approx 1.7$ a parameter capturing the energy dissipation ratios. [Tholen et al., 2023] further provided an empirical discovery of a third-root scaling in the particle-fluid density ratio. Our DEM simulations were used to support their analytical findings in the paper. The simulations were performed over varying environments, especially rarefied atmospheres. The DEM allowed for a switch between simulating over both fully rough (turbulent) and a complex boundary-layer described by the viscous sublayer and had reasonable fit with theoretical predictions as well as experiments. This proved the robustness of simulating sand transport simulations over Earth and other rarefied spaces. As a future scope, the field of study could benefit research over terrestrial landforms of aeolian interest such as Mars [Sullivan et al., 2005], Pluto (Icy dunes formed of methane) [Telfer et al., 2018], Venus [Sagan, 1975], Titan [Comola et al., 2022], and further exo-systems where future space missions dictate.

4.3 Modeling low-sand availability

In this section we address an important problem with the availability of sediments for transport, and it's overall implication on the transport scaling. In the numerical model for this particular study, a rough turbulent layer is chosen (no viscous sub-layer close to the bed) which was described in Section (2.4).

Previous models of wind-blown sand were designed to compute sand transport rates over a thick sand layer, such as the surface of large, active sand dunes. However, natural soils encompass a broad range of low sand availability conditions, such as crusted or bare soils. [Shen et al., 2020] conducted studies on the field site in Gobi desert, and they point out the importance of characterizing aeolian surfaces. Fig. (4.4) from their work showcases the desert pavement, the transition zone between the pavement and dune areas and the dune areas with ample sand supply. It has been a long-standing open question how wind-blown sand transport rates respond to wind velocity when the bare ground is covered by a thin layer of sand. Here in this chapter, we calculate the trajectories of wind-blown sand grains over these transitioning surfaces and find that sand transport rates increase faster with wind speed under low sand availability conditions than over sand dunes.

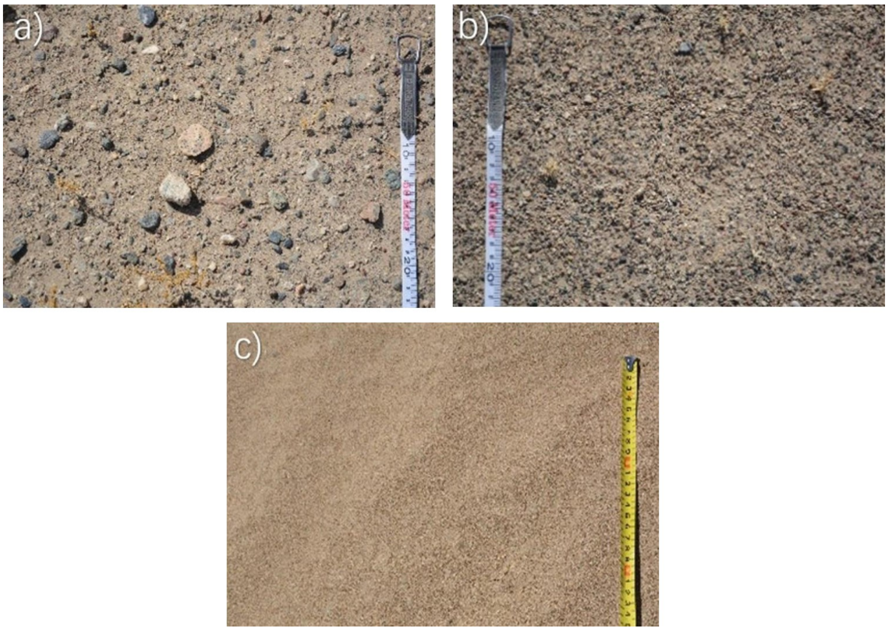

Figure 4.4: The vast expanse of the Gobi Desert is spatially heterogeneous, which creates sporadic conditions of sand availability for aeolian transport [Shen et al., 2020]

Previous models of Aeolian transport focused mainly on the transport over either fully erodible beds, such as migrating dunes and ripples [Anderson and Haff, 1988, Shao and Li, 1999, Sauermann et al., 2001, Almeida et al., 2008, Kok and Renno, 2009, Lämmel et al., 2012, Pähtz et al., 2014b, Comola et al., 2019], or rigid, fully non-erodible beds, such as consolidated dunes and bare soils [Ho et al., 2011]. These studies have shown that wind-blown transport rates follow either a quadratic or a cubic scaling with the wind shear velocity u_* - which is proportional to the mean flow velocity gradient in turbulent boundary layer flow - depending upon the bed being fully erodible or fully non-erodible, respectively [Creyssels et al., 2009, Ho et al., 2011]. Moreover, a quartic scaling of the sand flux with u_*, characterizing a collisional or intense transport regime where the saltation layer is connected to the granular bed through an intermediate granular layer of intense mid-air collisions, has been reported for fully erodible bed conditions when u_* exceeds about $4u_{*,\mathrm{it}}$, where $u_{*,\mathrm{it}}$ stands for the minimal threshold for sustained transport [Pähtz and

Durán, 2020, Ralaiarisoa et al., 2020]. However, natural Aeolian systems encompass a broad range of soil types characterized by low sand availability on the ground, including bare and crusted soils sparsely covered with mobile sediments ([Shao, 2008, Amir et al., 2014]. The characteristics of Aeolian transport over such types of soil, i.e., when the thickness of the mobile sand layer on the rigid ground is comparable to a few grain diameters, are poorly understood.

As we discuss in the subsequent sections, our DEM simulations show that the scaling of the sand flux with u_* displays considerable and yet unreported dependence on the availability of sand on the ground - characterized here through the thickness of the mobile sediment layer covering the non-erodible surface.

4.3.1 Numerical set-up

We start our simulations by pouring sand-sized spherical particles of diameter d uniformly distributed in the range $160 \leq d/\mu\mathrm{m} \leq 240$ onto a flat horizontal rigid bed at the bottom of the simulation domain — which has dimensions $(L_x \times L_y \times L_z)/d_\mathrm{m} = (200 \times 8 \times 1000)$, with $d_\mathrm{m} = 200\,\mu\mathrm{m}$ denoting the mean grain size (Fig. 4.5). In doing so, we generate a thin bed of N_p randomly poured particles on the ground, where the bed thickness δ_0 is determined by N_p. For instance, $N_\mathrm{p} = 30,000$ for $\delta_0 \approx 15\,d_\mathrm{m}$.

Furthermore, we adopt periodic boundary conditions in the along-wind (x) and cross-wind (y) directions and impose a reflective horizontal wall at the top of the simulation domain, to avoid that particles escape through crossing the upper boundary at $z = L_z$. However, we find that removing this reflective wall would allow only few particles for escaping, thus leading to a negligible change in the results of our simulations.

Once the particles come to rest and the bed has been formed, a few particles are injected into the simulation domain to impact on the ground, thus producing a splash and ejecting grains into air. The Aeolian drag force on the particles is computed with the expression,

$$\mathbf{F}_i^{\mathrm{d}} = -\frac{\pi d_i^2}{8}\rho_{\mathrm{f}} C_i^{\mathrm{d}} v_i^{\mathrm{r}} \mathbf{v}_i^{\mathrm{r}}, \tag{4.7}$$

where $\rho_{\mathrm{f}} = 1.225\,\mathrm{kg/m^3}$ is the air density and $\mathbf{v}_i^{\mathrm{r}} = \mathbf{v}_i - \mathbf{u}(z_i)$ is the difference between the velocity $\mathbf{v}_i$ of particle i and the wind velocity $\mathbf{u}(z_i)$ at the height z_i of the particle's center of mass. Furthermore, $v_i^{\mathrm{r}} = |\mathbf{v}_i^{\mathrm{r}}|$, while the drag coefficient C_i^{d} is computed through [Cheng, 1997] $C_i^{\mathrm{d}} = \left[(32/\mathrm{Re}_i)^{2/3} + 1\right]^{3/2}$, where the Reynolds number $\mathrm{Re}_i = \rho_{\mathrm{f}} v_i^{\mathrm{r}} d_i/\mu$, with $\mu = 1.8702 \times 10^{-5}\,\mathrm{kg\,m^{-1}s^{-1}}$ denoting the dynamic viscosity of the air.

The wind velocity profile is constant along x and y throughout the simulations, while the initial vertical profile of the horizontal (downstream) wind velocity, $u_x(z)$, reads,

$$u_x(z) = \frac{u_*}{\kappa} \ln \frac{z - h_0 + z_0}{z_0} \tag{4.8}$$

where u_* is the wind shear velocity, $\kappa = 0.4$ the von Kármán constant, $z_0 \approx d_{\mathrm{m}}/30$ is the roughness of the quiescent bed, and h_0 is the bed height, which is set as the uppermost height within the granular surface where the particles move with velocity smaller than $0.1\,u_*$ [Carneiro et al., 2011]. However, the acceleration of the particles owing to the action of the drag force extracts momentum from the air [Owen, 1964, Anderson and Haff, 1991], thus leading to a modification of the wind velocity profile. The modified velocity profile is obtained by numerical integration of [Carneiro et al., 2011].

$$\frac{\partial u_x}{\partial z} = \frac{u_{\tau,x}(z)}{\kappa z};\ u_{\tau,x}(z) = u_*\left[1 - \frac{\tau_{\mathrm{p}}(z)}{\rho_{\mathrm{f}} u_*^2}\right]^{1/2}, \tag{4.9}$$

where $\tau_{\mathrm{p}}(z)$ is the grain-borne shear stress and is given by

$$\tau_{\mathrm{p}}(z) \approx \sum_{j:Z_j>z} \frac{\mathcal{F}_x^{\mathrm{d}}(Z_j)}{A}, \tag{4.10}$$

with $\mathcal{F}_x^{\mathrm{d}}(Z_j)$ denoting the horizontal component of the total drag force on the particles with center of mass at Z_j, while $A = L_x \cdot L_y$ [Carneiro et al., 2011].

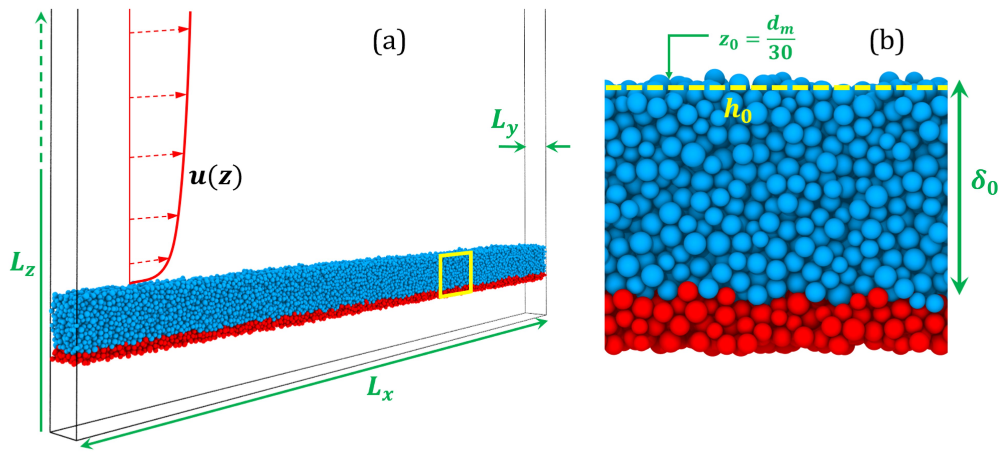

Figure 4.5: (a) Snapshot of the numerical experiment at $t = 0$, indicating the dimensions of the simulation domain and the undisturbed wind profile. (b) Side-view of an excerpt of the sediment bed, displaying a layer of mobile particles (blue) of thickness δ_0 on top of the immobile particles constituting the rough ground.

Furthermore, in order to obtain a rough rigid bed underneath the mobile sand cover, we deposit the mobile particles on top of a sheet of "*frozen*" immobile particles as displayed in Fig. 4.5. This is achieved through a module in LAMMPS, which zero out all forces and torques with the frozen grains. The interparticle interactions between the non-frozen and frozen grains are achieved, by regarding the frozen grains to be of infinite mass. In doing so, the rigid bed provides a model for a fully consolidated dune surface or bare granular surface, where the constituent immobile particles have the same diameter as the mobile grain size.

4.3.2 Results and discussion

Once transport begins, some of the grains composing the initial bed layer are entrained into flow, so that the bed layer thickness — which has initial value δ_0 at time $t = 0$ — decreases over time until transport eventually achieves steady state. At steady state, the bed layer thickness amounts to $\delta_s/d_m = \left(\delta_0/d_m - C_b u_*/\sqrt{g d_m}\right) \cdot \Theta\left(\delta_0/d_m - C_b u_*/\sqrt{g d_m}\right)$, where $C_b \approx 0.02$ is an empirical parameter and $\Theta(x)$ denotes the Heaviside function, i.e., $\Theta(x) = 1$ if $x \geq 0$ and $\Theta(x) = 0$ if $x < 0$ (Fig. 4.6). Therefore, the term $C_b u_*/(\sqrt{g d_m})$ ($\lesssim 0.5$ for all scenarios) denotes the thickness of the total eroded layer, relative to the particle size, from the beginning of transport until steady state.

4.3.2.1 Steady-state bed thickness (δ_s)

As mentioned above, once the sand transport process begins, the initial thickness of the mobile sand bed applied in the numerical simulations, δ_0, decreases toward a smaller value δ_s, which is achieved when transport conditions have reached steady state. As depicted in Fig. 4.6, δ_s and δ_0 are linearly related to each other, and the difference between both values of bed thickness displays a slight increase with u_* owing to the effect of wind shear velocity on enhancing erosion. However, we find that the scaling laws reported in the upcoming section are valid whatever value of bed thickness is chosen, while the following relation applies,

$$\frac{\delta_s}{d_m} = \left(\frac{\delta_0}{d_m} - C_b \frac{u_*}{\sqrt{g d_m}}\right) \cdot \Theta\left(\frac{\delta_0}{d_m} - C_b \frac{u_*}{\sqrt{g d_m}}\right) \tag{4.11}$$

where $C_b \approx 0.02$ is an empirical parameter and $\Theta(x)$ denotes the Heaviside function, i.e., $\Theta(x) = 1$ if $x \geq 0$ and $\Theta(x) = 0$ if $x < 0$. Therefore, the term $C_b u_*/(\sqrt{g d_m})$ denotes the thickness of the total eroded layer, relative to the particle size, from the beginning of transport until steady state (i.e., as the bed thickness evolves from δ_0 toward δ_s).

In Fig. 4.6, the filled symbols correspond to numerical simulations in which the wind is carrying the maximum possible number of particles, i.e., the flux is saturated. Starting with $\delta_0 = 15\, d_m$, for instance, and under a given value of $u_* - u_{*t}$, we observe no change in the average number of particles

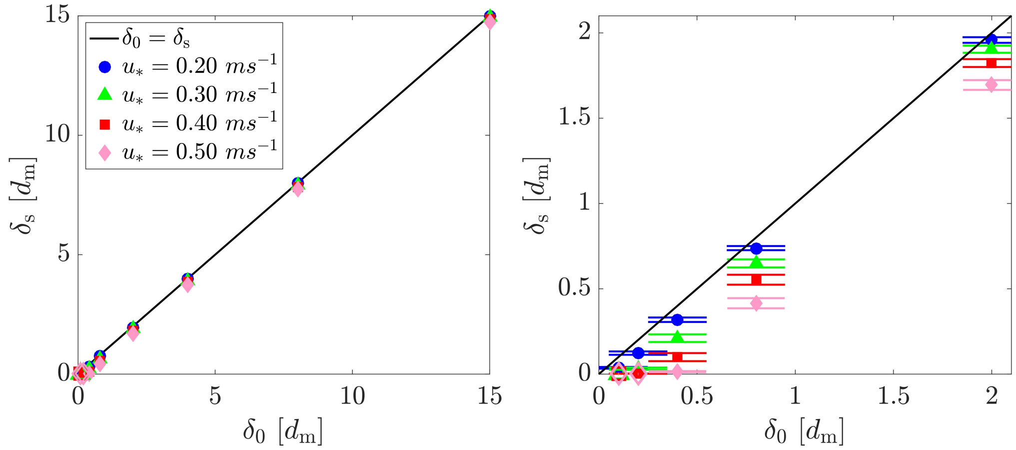

Figure 4.6: (a) Values of the bed layer thickness at steady-state transport, δ_s, plotted against the initial values of bed layer thickness, δ_0, for different values of the wind shear velocity u_*. The plot in (b) denotes a zoom into the region of bed layer thickness comparable to the particle size. Filled symbols correspond to saturated transport conditions, while empty symbols denote under-saturated scenarios (the same color code used for the filled symbols in the legend applies to specify u_* in these empty symbol scenarios).

in the Aeolian layer (or, equivalently, the mass density of dragged particles) upon a decrease in the initial bed thickness δ_0, as long as the scenarios associated with the filled symbols in Fig. 4.6 are considered. However, the empty symbols in this figure constitute scenarios where the bed thickness is so small, that the wind flow does not dispose of enough particles on the ground to drive transport toward the saturated flux. These empty symbols are associated with a value of steady-state bed thickness equal to 0 and are referred to as *under-saturated*. Specifically, for these empty symbols, the wind eroded the entire sand bed and still the amount of sand transport is not enough to saturate the sand flux (the most extreme, non-vanishing flux scenario of such under-saturated regime in our simulations would be, in particular, the case of one single grain hopping downwind).

We have thus not considered these under-saturated scenarios in our analysis of $Q(u_*)$, since we are interested here in an expression for the saturated flux that accounts for the bed erodibility. Moreover, it is a straightforward conclusion that, in the under-saturated regime, the mass density of the transport layer decreases upon a reduction of the initial bed thickness δ_0/d_m. Nevertheless, we note that under-saturated transport scenarios constitute an interesting topic to be investigated in future work. For instance, such scenarios have applications to areas that are devoid of any sand availability but subjected to an upwind flux that is under-saturated (for instance in the presence of upwind vegetation or moisture), or over inter-dune bedrock areas within fields of sparsely distributed dunes [Fryberger et al., 1984]).

We note that periodic boundary conditions are applied in our simulations (Section (4.3.1)), so that the number of particles in the system is constant over time. Indeed, the domain of our simulations may be interpreted as a small stretch of soil over which the sediment flux is in the steady state. Due to fluctuations associated with the transport dynamics, the difference between the particle mass outflux from and influx into this soil stretch varies over time, but on average, the total number of particles within the associated volume is constant over time.

4.3.2.2 Scaling relations

We begin our discussion by considering an initial bed thickness $\delta_0 = 15\,d_\mathrm{m}$, for which we observe steady-state transport conditions ($\delta_\mathrm{s} \approx 14.8\,d_\mathrm{m}$) consistent with the fully erodible bed scenario reported in previous studies. Specifically, our simulations reproduce quantitatively the height-integrated, non-suspended mass flux of transported particles, Q, as a function of u_* over fully erodible beds, and the observation that, for moderate wind conditions ($u_*/u_{*,\mathrm{it}} \lesssim 4$), Q is approximately proportional to $\tau - \tau_\mathrm{t}$, with $\tau = \rho_\mathrm{f} u_*^2$ denoting the mean shear stress of the turbulent wind flow over the surface, and $\tau_\mathrm{t} = \rho_\mathrm{f} u_{*,\mathrm{it}}^2$ corresponding to the minimal threshold τ for transport (Fig. 4.7). Furthermore, our numerical predictions match the experimental observations of the nearly exponential decay of the vertical particle concentration with the height above the ground and the value of $u_{*,\mathrm{it}} \approx 0.165\,\mathrm{m/s}$ predicted for the mean particle size in our simulations (Fig. (4.2)).

However, as we decrease the initial bed layer thickness δ_0 substantially, we observe a change in the scaling of the steady-state sediment flux with u_*. More precisely, our simulation results follow, approximately, the model,

$$
\begin{aligned}
Q &= \left\{a \cdot \left[1 + b \cdot \left(\frac{u_*}{u_{*\mathrm{t}}} - 1\right)\right]\right\} \cdot \sqrt{\frac{d}{g}} \cdot [\tau - \tau_{\mathrm{t}}], && (4.12)\\
u_{*\mathrm{t}} &= u_{*\mathrm{t},\infty} \cdot \{1 - C_{\mathrm{t}} \cdot \exp[-c_{\mathrm{t}} \cdot \delta_{\mathrm{s}}/d_{\mathrm{m}}]\} && (4.13)\\
a &= a_\infty \cdot \{1 - C_a \cdot \exp[-c_a \cdot \delta_{\mathrm{s}}/d_{\mathrm{m}}]\} && (4.14)\\
b &= b_\infty \cdot \exp\left[-c_b\sqrt{\delta_{\mathrm{s}}/d_{\mathrm{m}}}\right] && (4.15)
\end{aligned}
$$

where $u_{*\mathrm{t},\infty} \approx 0.165\,\mathrm{m/s}$, $a_\infty \approx 22.15$ and $b_\infty \approx 5.28$ denote the values of $u_{*\mathrm{t}}$ and the empirical constants a and b, respectively, associated with fully erodible bed scenario ($\delta_{\mathrm{s}}/d_{\mathrm{m}} \to \infty$), while the best fits to the simulation data in the range $\delta_{\mathrm{s}}/d_{\mathrm{m}} \leq 10$ yield $C_{\mathrm{t}} \approx 0.14$, $c_{\mathrm{t}} \approx 0.83$, $C_a \approx 0.47$, $c_a \approx 0.76$ and $c_b \approx 2.61$ (Fig. 4.7).

Wind tunnel experiments [Ho et al., 2011] revealed a cubic scaling of Q with u_* on fully rigid beds. Here, we find that sediment transport rates over a soil that is not fully rigid but contains, instead, a thin layer of mobile sediment, further depends on this layer's thickness according to Eqs. (4.12)-(4.15). Specifically, the coefficient b in Eq. (4.15) controls the transition from the cubic to the quadratic scaling of Q with u_* in Eq. (4.12) as bed conditions change from fully rigid ($\delta_{\mathrm{s}} = 0$) to fully erodible ($\delta_{\mathrm{s}} \gg d$). Moreover, while the coefficient a provides an attenuating factor for Q near the rigid bed scenario, a decrease in bed thickness reduces the minimal threshold shear velocity, $u_{*\mathrm{t}}$, as we elucidate next.

To shed light on the microscopic origin of Eq. (4.12), we note that momentum conservation yields $Q = [\ell_{\mathrm{hop}}/(u_{0\downarrow} - u_{0\uparrow})] \cdot [\tau - \tau_{\mathrm{t}}]$ [Bagnold, 1941, Sørensen, 2004, Ho et al., 2011], where ℓ_{hop} denotes the mean hop length of the saltating particles, while $u_{0\downarrow}$ and $u_{0\uparrow}$ are their mean horizontal impact and lift-off velocities, respectively. Furthermore, ℓ_{hop} and $u_{0\downarrow} - u_{0\uparrow}$ (computed as explained below) are related to the mean horizontal grain velocity $u_0 = (u_{0\downarrow} + u_{0\uparrow})/2$ (or slip velocity) through the approximate scaling expressions $\ell_{\mathrm{hop}} \propto u_0^2/g$

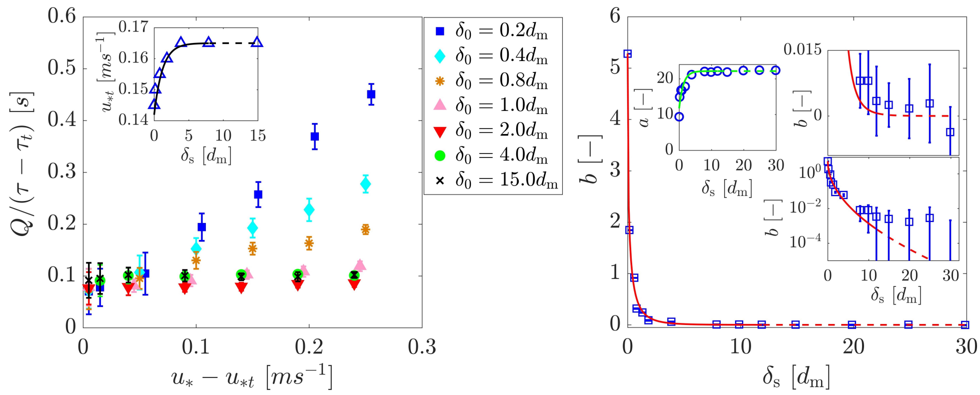

Figure 4.7: (a) Sand flux Q rescaled with the excess shear stress, $\tau-\tau_\mathrm{t}$, plotted as a function of $(u_*-u_{*\mathrm{t}})$ for different values of the initial bed thickness, δ_0; inset: the minimal threshold shear velocity for sustained transport, $u_{*\mathrm{t}}$ as a function of the steady-state bed thickness, δ_s. (b) Circles and squares denote the parameters a and b in Eq. (4.12), respectively, as obtained from the best fit to the data in (a). The continuous lines in (a) and (b) denote the best fits using Eqs. (4.13)-(4.15) in the range $\delta_\mathrm{s}/d_\mathrm{m}\leq 10$ (the continuation of these fits toward larger $\delta_\mathrm{s}/d_\mathrm{m}$ or fully erodible bed scenario is indicated by the dashed line as a guide to the eye). Error bars denote the standard deviation from averaging over 5 s within the steady state.

and $u_{0\downarrow}-u_{0\uparrow}\propto u_0$ [Ho et al., 2011], which leads to $Q\approx C_u\cdot(u_0/g)\cdot[\tau-\tau_\mathrm{t}]$, where C_u is an empirical parameter.

Computation of the mean hop length and the mean horizontal impact and lift-off velocities

To compute the mean hop length ℓ_hop and the average horizontal impact and lift-off velocities, $u_{0\downarrow}$ and $u_{0\uparrow}$, respectively, we consider only the grains with a minimum vertical lift-off velocity of $\sqrt{6gd}$, i.e., the grains that achieve a minimum height of $3\,d_\mathrm{m}$ above the bed height. The values of ℓ_hop, $u_{0\downarrow}$ and $u_{0\uparrow}$, are then averaged over a time window of 5 seconds during steady-state sand transport.

The mean horizontal grain velocity or slip velocity u_0 is then computed using

$$u_0 = (u_{0\downarrow} + u_{0\uparrow})/2. \tag{4.16}$$

Furthermore, to obtain the mean hop length, we start from the mean hop time, which is given by [Ho et al 2011],

$$t_{\mathrm{hop}} \approx \frac{2v_{0\uparrow}}{g}, \tag{4.17}$$

where $v_0 \uparrow$ is the mean ascending vertical velocity of the grains (also averaged over 5 seconds in the steady state). Furthermore, the horizontal acceleration of the grains is given by,

$$a_{\mathrm{hor}} \approx \frac{(u_{0\downarrow} - u_{0\uparrow})}{t_{\mathrm{hop}}}, \tag{4.18}$$

so that the mean hop length is approximated as,

$$\ell_{\mathrm{hop}} \approx (u_{0\downarrow} - u_{0\uparrow})\,\frac{v_{0\uparrow}}{g}. \tag{4.19}$$

An increase in u_* over a fully erodible bed leads to an enhancement of the particle concentration in the transport layer without significantly affecting u_0, so that Q scales quadratically with u_* in the fully erodible bed regime [Ho et al., 2011]. By contrast, the transport layer over the hard surface is, for a given saltation flux, much thicker than over an erodible bed because of the non-saturated feedback which keeps a larger wind velocity in the saltation layer [Ho et al 2011]. The weak coupling between the particles and the wind in the transport layer over a fully non-erodible surface results in a linear scaling of u_0 with u_*, thus yielding a cubic scaling of Q with u_* in the fully rigid bed regime [Ho et al., 2011].

Here we find that, in the presence of a thin layer of mobile sand on the hard ground, the scaling of u_0 with u_* further depends on δ_{s} (Fig. 3c). We find that

$$C_u \cdot \frac{u_0}{g} \approx a \cdot \left[1 + b \cdot \left(\frac{u_*}{u_{*\mathrm{t}}} - 1\right)\right] \sqrt{\frac{d}{g}} \tag{4.20}$$

with $C_u \approx 1.68$, where the RHS of Eq. (4.20) is the multiplicative factor of $[\tau - \tau_\mathrm{t}]$ in Eq. (4.12), i.e., including the values of $u_{*\mathrm{t}}$, a and b estimated from Fig. 2. Therefore, Eq. (4.20) elucidates the microscopic origin of Eq. (4.12). Since all scenarios (δ_0, u_*) considered here are associated with saturated transport conditions in the steady state (see Fig. (4.6)), i.e., since the total mass of particles in the transport layer under given $u_* - u_{*,\mathrm{it}}$ is the same for all values of δ_0 considered, the effect of sand availability on the scaling of $Q(u_*)$ is attributed entirely to the dependence of u_0 on this availability, encoded in the parameters on the RHS of Eq. (4.20). Our simulations further show that, as sand availability decreases and the transport layer expands, transport can be sustained at increasingly lower u_* (Fig. 4.7a and Eq. (4.13)). This finding is further consistent with the wind-tunnel observation that $u_{*,\mathrm{it}}$ over fully rigid beds is lower than over fully erodible beds [Ho et al., 2011].

To the best of our knowledge, our study is the first one to estimate sediment transport rates from direct numerical simulations of particle trajectories under intermediate soil erodibility conditions between fully erodible and fully non-erodible. We find that our results remain approximately valid when the rigid bed underneath the mobile sediment layer is a smooth flat surface. However, the immobile roughness elements on the hard ground have a crucial effect on the value of the Aeolian sand flux.

4.3.3 Anomalous splash dynamics

In the regime where saltating particles collide onto a sand bed of thickness $\lesssim 2\,d_\mathrm{m}$, and in the presence of roughness elements on the hard ground underneath, sand particles are ejected through splash events mainly *backwards*, i.e., the majority of ejecta displays negative horizontal lift-off velocity component. This result can be understood by noting that, as downwind hopping grains impact obliquely upon the thin sand layer covering the rough ground,

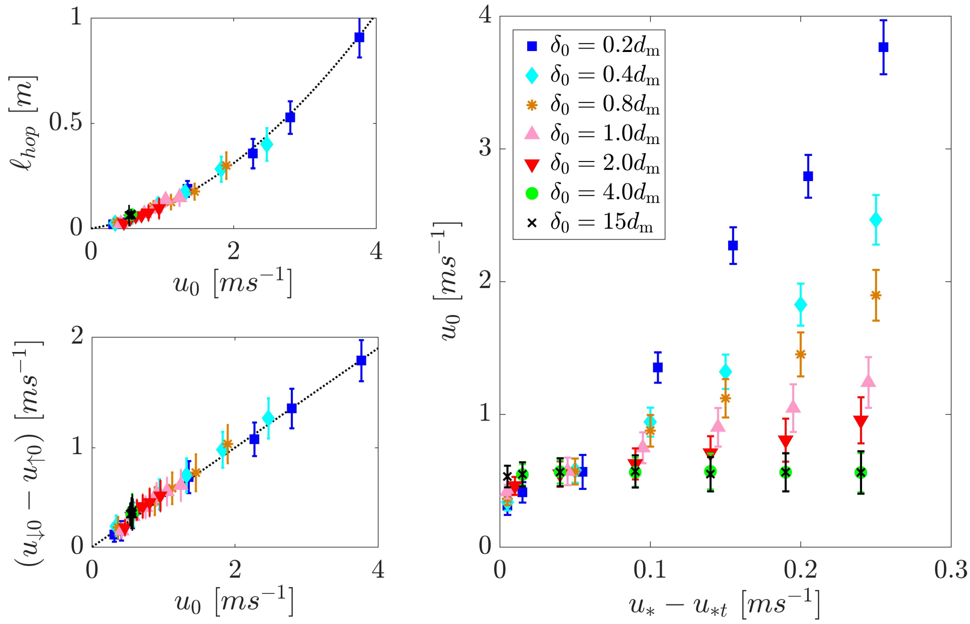

Figure 4.8: (a) Mean hop length, ℓ_{hop}, and (b) difference between the mean grain horizontal velocities at impact and lift-off, $u_{0\downarrow} - u_{0\uparrow}$, as a function of the slip velocity u_0. The dashed lines in (a) and (b) denote $\ell_{\mathrm{hop}} \approx 0.065u_0^2$ and $u_{0\downarrow} - u_{0\uparrow} \approx 0.43u_0$, respectively, obtained from the best fits to the simulation data. In (c), the slip velocity is shown as a function of $u_* - u_{*\mathrm{t}}$ for different values of δ_0. The legend in (c) applies as well to both (a) and (b).

they mobilize soil grains forward, which, however, collide with the roughness elements located in their front. Upon such collisions, the trajectories of the bed particles mobilized by grain-bed impacts are reflected backwards, as elucidated through our granular splash experiments (Fig. 4, where N_{ej} is the number of ejected grains per impact).

These dynamics, which act by attenuating Q upon exposure of the bed roughness elements, are encoded in the coefficient a in Eq. (4.12), and constitute behavior opposite to the effect of the bed thickness on b and $u_{*\mathrm{t}}$, which contribute to enhancing Q (see Eqs. (4.12)-(4.15)). These competing effects lead to an anomaly in the dependence of Q on the bed thickness, with the emergence of a minimum around $\delta_0 \approx 2\,d_{\mathrm{m}}$ (or $\delta_{\mathrm{s}} \approx 1.8\,d_{\mathrm{m}}$). This anomaly is not observed when the ground is a smooth flat surface (Fig. 5). The bed thick-

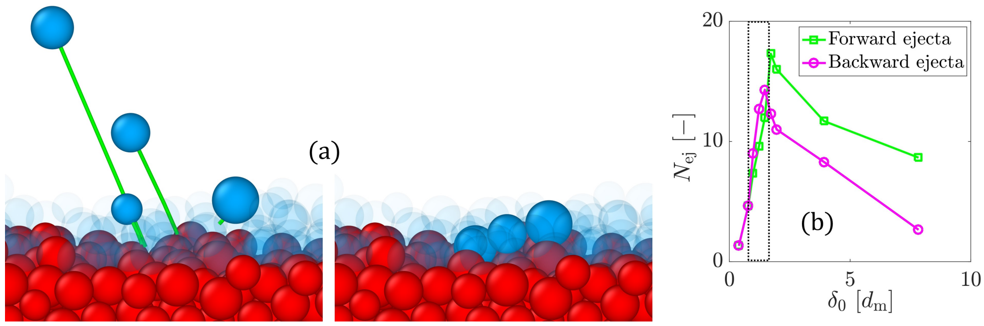

Figure 4.9: By means of granular splash numerical experiments with impact angles and velocities characteristic of wind-blown sand transport (a), we find that most ejected grains have negative horizontal lift-off velocity, when the value of the bed layer thickness is $\lesssim 2\,d_{\mathrm{m}}$, and positive otherwise (b). The snapshots correspond to a simulation using a bed layer thickness $\approx 2\,d_{\mathrm{m}}$. Most of the mobile (blue) particles lying on the rigid grains (red) have been rendered transparent for better visualization of the splashed particles.

ness associated with the minimum Q is independent of u_*, thus indicating that the anomaly reported here is purely a signature of the bed roughness and is not affected by the flow properties.

We note that, notwithstanding the strong decrease of N_{ej} with the bed thickness in the regime $\delta_0/d_{\mathrm{m}} \gtrsim 2$ (Fig. 4.9b), the steady-state sand flux Q in this regime is only weakly affected by the amount of mobile grains on the ground (Fig. 4.7a). Therefore, our simulation results are providing evidence in support of the hypothesis that the magnitude of Q is controlled by the rebound dynamics of sand grains during transport — as assumed, for instance, in a recent purely rebound-based model [Pähtz et al., 2021] — rather than by the splash process. Our results further help to elucidate the observation that cohesion, which affects mainly the splash process by enhancing particle-particle attractive interaction forces within the bed, has little impact on Q and the threshold for Aeolian transport cessation, as these are mainly controlled by rebound dynamics [Comola et al., 2019].

Our model reproduces the scaling laws of Q with u_* observed experimentally over fully erodible and rigid beds (Figs. 4.7 and 4.2). However, various ingredients that are essential to improve the quantitative assessment of Ae-

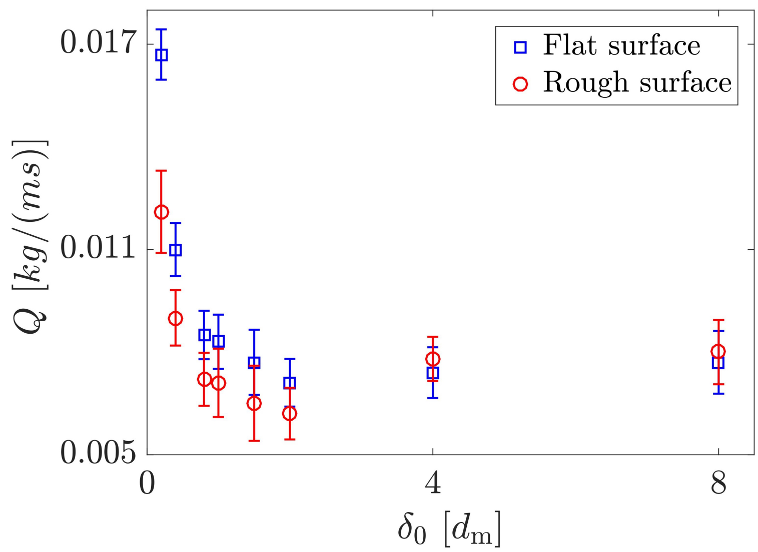

Figure 4.10: Sand flux Q as a function of δ_0, obtained with $u_* = 0.30\,\mathrm{m/s}$. We considered the non-erodible surface consisting of a smooth flat ground (blue) and immobile particles (red).

olian sand flux, such as complex particle geometric shapes and aerodynamic entrainment [Li et al., 2020], should be incorporated in future work. Furthermore, we have employed sand-sized non-erodible roughness elements, but natural soils encompass much broader particle size distributions, including gravels, pebbles and rocks. From our results, we expect that such coarser non-erodible elements have even larger impact on the sand flux scaling. Our model is paving the way toward a quantitative representation of sand availability conditions in larger scale models, such as regional Earth system simulations, by explicitly incorporating the information of local steady-state bed thickness in the parametrization of Aeolian sand transport rates.

Previous work developed continuum models for Aeolian flux that explicitly account for sand supply and spatio-temporal variations in bed surface properties, including moisture, shells, non-erodible elements and vegetation [De Vries et al., 2014, Hoonhout and Vries, 2016]. Furthermore, the particle-based simulations adopted in the present work provide a means to improve our understanding of the (microscopic) particle-scale mechanisms controlling the response of Aeolian transport processes to different types of soil and particle-bed interactions. Future research combining insights from both types of model could thus help to achieve improved numerical simulations of Aeolian soil morphodynamic processes at different scales [Werner, 1995, Kroy et al., 2002, Durán et al., 2010], by incorporating the effect of sediment availability on sediment flux and erosion/deposition rates.

In summary, this was one of the first attempts at a numerical model for wind-blown sand flux under low sand availability, by characterizing this flux as a function of the thickness of the mobile sediment layer available for transport on the ground. Specifically, it can be understood that the Aeolian sand flux scales with the excess shear stress multiplied by a coefficient that decreases with the mobile layer thickness covering the non-erodible ground, thereby yielding a model for Aeolian transport rates under intermediate bed erodibility conditions between the fully erodible and fully non-erodible scenarios. The model elucidates how the scaling of the Aeolian sand flux Q with the wind shear velocity u_* changes from quadratic to cubic as bed conditions change from fully erodible to fully non-erodible, respectively [Ho et al., 2011]. It was also found that the roughness elements on the rigid bed affect the sediment flux upon rigid bed exposure. It causes an anomaly in the behavior of Q with the bed layer thickness, with the occurrence of a minimum which is independent on the flow conditions. These findings will have an implication for the representation of non-erodible elements associated with different types of soil in future experimental and theoretical studies. We have established our sand transport models, not only validating existing scaling relations, but also providing new insights into the low-sand availability conditions. We jump down a scale in size to model dust, in the next chapters by including cohesion and few other critical features and study their interwoven roles in either inhibiting or enhancing dust emission.

Chapter 5

Modeling mineral dust

An interplay of cohesion and turbulence –

Dust, by definition represents the class of particles usually also called silt and clay, $\lessapprox$ 70 μm and below [Shao, 2008], and in undisturbed soils is usually found as forming clumps with particles of similar size to form bigger aggregates, or coated over a larger particle [Bullard et al., 2004] (Fig. 5.1). Once released from the bed by the breakage of cohesive bonds, can drift through large distance by both convective and turbulent transport. This idea of how the turbulent wind shear dominating the inter-particle cohesion, serves as the opening to this chapter. The terms aggregate, agglomerate, clump, and cluster if used interchangeably from here-on mean the same thing. To my best understanding from literature, this is a first attempt for a particle-based large-scale model to directly study the transport conditions for sand and dust, without any underlying assumptions or *splash functions* generally employed in previous studies [Kok and Renno, 2009]. On the other hand, this could motivate further works to carefully consider these additional phenomena in the splash functions. Thus, we first build a physical basis to model dust along with sand, to run large scale simulations of dust emission in a mixed bed comprising sand and dust grains to study the vertical emission flux in the next chapter. The open questions this chapter tries to address are as follows -

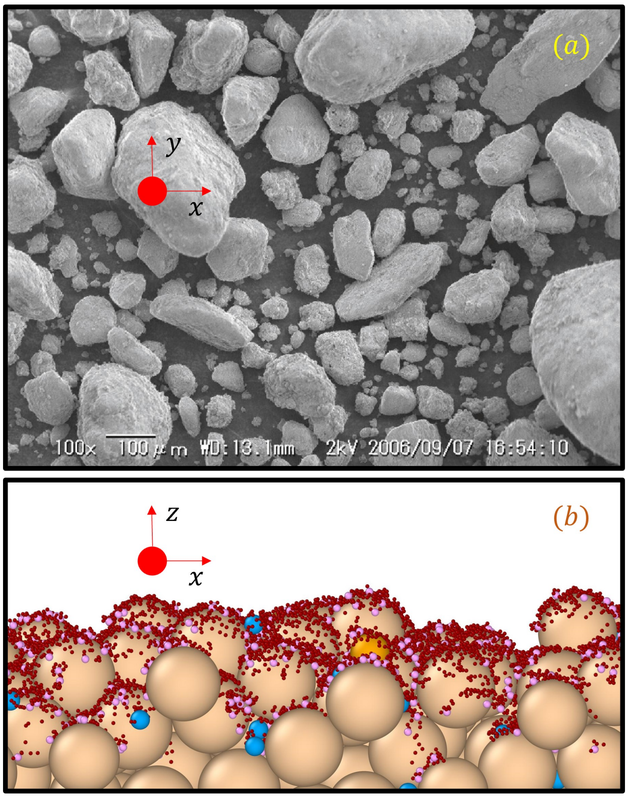

Figure 5.1: (a) Dust and sand sized particles seen through an electron microscope [Shao, 2008], and (b) A snapshot of our DEM simulation showing the clumpy behavior of smaller grains $d < 20$ μm coating larger sand grains ($d \approx 200$ μm)

- What additional external forces/factors which were neglected before need to be modeled now?
- How do we estimate contact and other force parameters, and can we validate them somehow?
- What can we say about the initiation of transport, that is what role does cohesion, lift and turbulence play on the fluid (dynamic) threshold?
- What is the role of surface roughness in aiding or impeding the entrainment?

[Pähtz et al., 2020] provides an extensive review on the current understanding of the grain initiation and entrainment. Let's take a close look at the three general mechanisms by which dust is ejected into the atmosphere [Shao, 2008].

5.1 Mechanisms for dust emission

The dust emission process is understood to occur through three major mechanisms, each associated with specific environmental conditions and surface characteristics of the soil bed.

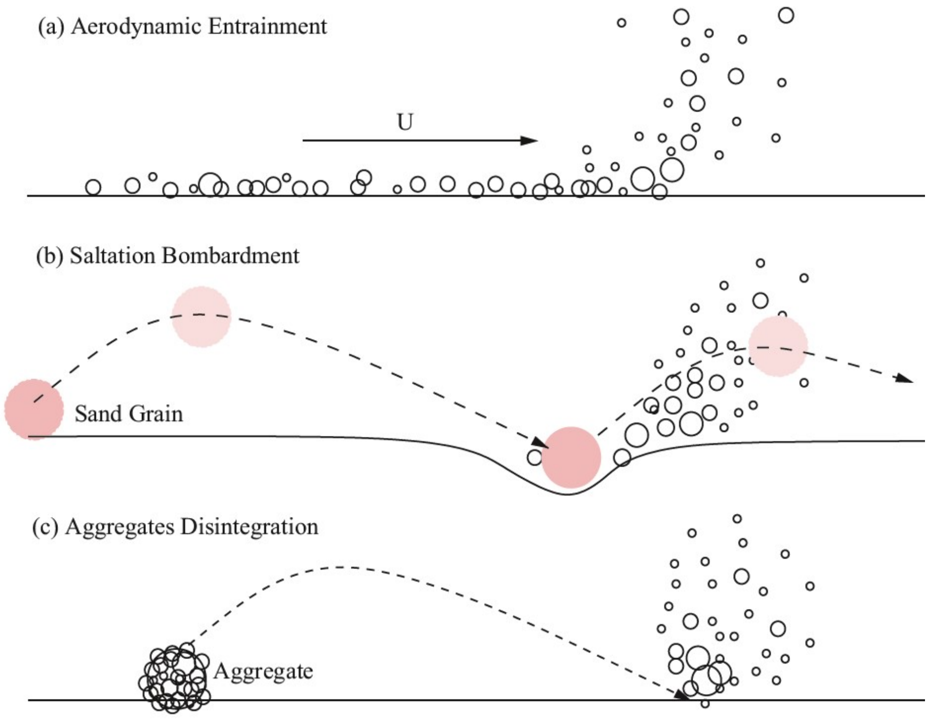

Figure 5.2: The general mechanisms for dust emission - (a) Aerodynamic entraiment, (b) Saltation bombardment, and (c) Aggregate disintegration [Shao, 2008]

(a) Aerodynamic entrainment - It is possible that the exposed dust grains are directly lifted by the wind [Loosmore and Hunt, 2000]. However, for smaller dust grains cohesion has a relatively stronger dominion over the other forces, making it hard for entrainment, hence inhibiting the emission. It will be shown later, this is not entirely true as the surface characteristics owing to the roughness and turbulent fluctuations arising in the wind field can aid in entrainment during the onset of transport. However, it is important to note that the once there is a steady transport of particles, it provides a negative feedback to lower the wind shear close to surface. We would later describe in Section (6.2.1) that direct entrainment holds significance for even PM_{10} grains under supply limited conditions.

(b) Saltation bombardment - As saltating sand grains hop along the bed, the impacts could provide sufficient energy to break the cohesion between grains and thus releasing dust [Gillette, 1974, Shao et al., 1993] freely available for turbulent diffusion. It is not clear, whether this leads to the emission of either distinct grains or smaller dust aggregates, or dust-coated-on-sand grains. This is the advantage of our DEM model where we could further distinguish these, and we address this behavior in the Section (6.1.1) where we define these grain clusters.

(c) Aggregate disintegration - This is similar to the previous mechanism, but differs in the saltating grain which here could be a dust-coated-on-sand grain or an aggregate made up of individual dust grains. Both the types of aggregates during a low erosion event might retain their structural integrity if initiated into transport or could eventually start losing particles over the hops. However during higher erosion events, they could straight-away disintegrate depending again on the surface characteristics.

5.2 Model extensions

To study the aforementioned processes, we add these additional modules into the existing CFD-DEM framework described in Section (2.3) - Cohesion, Rolling resistance and Turbulent fluctuations. Although it is evident to include cohesion and turbulent fluctuations when considering fine grains, the inclusion of rolling resistance is integral too for accurate validations of the model in general, and prediction of threshold conditions. I explain these new add-ons to the model in the upcoming sections (see Section (2.3.1) for the equations describing the van der Waals interaction in Eqn. (2.20)).
However, the current contact model which is based on a relatively less stiff material ($\mathcal{O}(10^{-4})$) than [Parteli et al., 2014b] would result in a larger deformations of the grains. This effect is compensated by scaling down the cohesion parameter γ_{s} [He et al., 2021]. This *"reduced-cohesion model"* [Washino et al., 2018] provides a scaling law with the appropriate consideration of the linear-spring contact model, and noting the independence of $\mathbf{F}^{\mathrm{c}}$ on the normal elastic constant k_{n} and δ_{n}.

5.2.1 Reduced cohesion model

The motion of the grains in the normal direction similar to Eqn. (3.1) is then described described by [Washino et al., 2018],

$$m\ddot{\mathbf{x}} + k_{\mathrm{n}}\delta_{\mathrm{n}} + \eta_{\mathrm{n}}\dot{\mathbf{x}} + \mathbf{F}_{\mathrm{c}} = 0 \tag{5.1}$$

Using the Eqn. (3.22) to replace the damping constant,

$$m\ddot{\mathbf{x}} + k_{\mathrm{n}}\delta_{\mathrm{n}} + \sqrt{\frac{4mk_{\mathrm{n}}}{1+\left(\pi/\ln\left(e_{\mathrm{r}}\right)\right)^2}}\dot{\mathbf{x}} + F^{\mathrm{c}} = 0 \tag{5.2}$$

$$\frac{\gamma_{\mathrm{s}}^{\mathrm{R}}}{\gamma_{\mathrm{s}}^{\mathrm{O}}} = \frac{A_H^{\mathrm{R}}}{A_H^{\mathrm{O}}} = \left(\frac{Y^{\mathrm{R}}}{Y^{\mathrm{O}}}\right)^{1/2} \tag{5.3}$$

where the superscripts R and O represent the reduced and original properties respectively. Eqn. (5.3) then results in a value of $\gamma_{\mathrm{s}} \approx 2 \times 10^{-4}$ J/m^2, which corresponds to $A_H \approx 4.1054 \times 10^{-22}$ J for use in the current contact model. The van der Waals force for grains in contact is linearly proportional to the effective diameter of the pair in contact. We define the Bond number (Bo) as the ratio of maximum cohesion to the gravitational force on the grain as, It is interesting to note here the dependency of Bo on the effective size of grains, that is,

$$\mathrm{Bo} = \frac{12\gamma_{\mathrm{s}} d_{\mathrm{eff}}}{\rho_{\mathrm{p}} g d^3} \tag{5.4}$$

For monodisperse system, a small d results in a higher Bo, which implies the prominence of cohesion over the weaker gravitation force. However, in polydisperse contacts,

$$\mathrm{Bo} = \frac{12\gamma_{\mathrm{s}}}{\rho_{\mathrm{p}} g d_1^2 \left(1 + d_1/d_2\right)} \tag{5.5}$$

where $d_1 <= d_2$. If $d_1 \ll d_2$, Bo $\propto (1/d_1^2)$ which is twice the quantity for monodisperse d_1 grains. Hence, it is easier for finer grains to be coated on larger grains owing to a larger Bo, than forming aggregates with similar sized grains.

5.2.2 Rolling resistance

As we noted earlier, for the sand simulations spherical grains experienced tangential forces and hence was only a case of pure rolling. However in reality, sand and dust grains are not perfectly spherical and there is a resistance to rolling motion, in the counter-direction. Previously neglecting rolling in simulating sand transport was acceptable, as we were mainly interested in the saltation phenomena. To capture the process of grain entrainment, especially in the dust size regime, the rolling resistance is crucial as we elaborate below. The rolling resistance is realized by considering an approach given by [Luding, 2008] as a *pseudo-force*, similar to the spring-dashpot-slider contact model in Section (3.1.2). The module in LAMMPS also considers the potential rolling

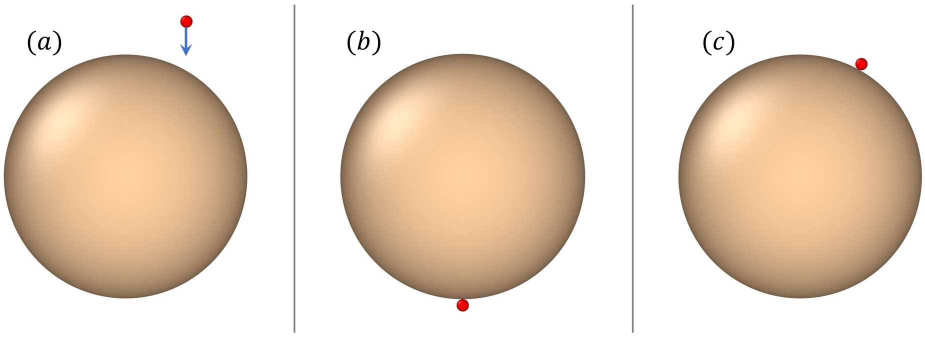

Figure 5.3: Rolling resistance is crucial to reproduce realistic rolling of finer dust grains and sand grains over each other. Hypothetical experiment with cohesion - (a) A dust grain of $d = 10$ μm is dropped over a frozen sand grain $d = 200$ μm, (b) state of the grain without rolling resistance, and (c) state of the grain with rolling resistance

displacements due to change in reference frames when 2 or more particles are in contact. The resistant force to rolling then is,

$$\mathbf{F}_{ij,\mathrm{r},0} = k_{ij,\mathrm{r}}\xi_\mathrm{r} - \gamma_{ij,\mathrm{r}}\mathbf{v}_{ij,\mathrm{roll}} \tag{5.6}$$

where $\mathbf{v}_{ij,\mathrm{roll}} = -R_\mathrm{eff}\left(\boldsymbol{\omega}_i - \boldsymbol{\omega}_j\right) \times \mathbf{n}$ is the relative rolling velocity [Wang et al., 2015, Luding, 2008], ξ_r is the rolling displacement which is the accumulated displacement in the contact duration $t_0 - t$ given by,

$$\xi_\mathrm{r} = \int_{t_0}^{t} \mathbf{v}_{ij,\mathrm{roll}}\left(\tau\right)\, d\tau \tag{5.7}$$

Using the Coulomb criterion, similar to that in the sliding friction model, the rolling force is limited if it surpasses a critical value:

$$\mathbf{F}_{ij,\mathrm{r}} = \min\left(\mu_\mathrm{r}\mathbf{F}_{\mathrm{n},0}, ||\mathbf{F}_{\mathrm{r},0}||\right)\mathbf{k} \tag{5.8}$$

where $\mathbf{k} = \mathbf{v}_\mathrm{roll}/||\mathbf{v}_\mathrm{roll}||$ is the direction of this force. This force thus is applied on particles in contact, to induce an equal and opposite torque on each of the pairs,

$$\tau_{\mathrm{r,i}} = R_\mathrm{eff}\mathbf{n} \times \mathbf{F}_\mathrm{roll} \tag{5.9}$$

$$\tau_{\mathrm{r,j}} = -\tau_{\mathrm{r,i}} \tag{5.10}$$

The rolling parameters corresponding for the elastic and damping characteristics $k_{ij,\mathrm{r}}$ and $\gamma_{ij,\mathrm{r}}$ are described in the below subsection.

Rolling parameters

A physical basis for estimating k_{r} as a fraction of k_{n} comes from [Santos et al., 2020],

$$\mathbf{F}_{\mathrm{r}} = \frac{8(2-\nu)(1-\nu^2)}{3(3-2\nu)} d \frac{G}{Y} \mathbf{F}_{\mathrm{n}} \theta_{\mathrm{r}} \tag{5.11}$$

where the shear modulus $G = Y/(2(1+\nu))$, the Poisson's ratio $\nu = 0.5$ while roughly considering $F_{\mathrm{r}} = k_{\mathrm{r}}\theta_{\mathrm{r}}$ and $F_{\mathrm{n}} = k_{\mathrm{n}}\delta_{\mathrm{n}}$. This results in,

$$k_{\mathrm{r}} = 0.5 k_{\mathrm{n}} \tag{5.12}$$

We consider a value of $\gamma_{\mathrm{r}} = 0.1\gamma_{\mathrm{n,p}}$, that is a fraction of the normal damping coefficient [Luding, 2008]. Using the full model with both cohesion and rolling resistance, the model parameters are validated using characteristic granular behavior, as to when grains are packed together and allowed to form a pile under gravity.

5.2.3 Model validation - granular packing problem

The granular packing problem involves understanding how particles, such as grains, powders, or beads, arrange themselves when packed together. The observation of either the packing fraction/density (ϕ) or the complement void fraction ($\beta = 1 - \phi$) and comparing with experiments leads to the affirmations regarding the material parameters. A random close packing of monodisperse, cohesionless, frictionless spheres results in a $\phi = 0.64$ [Bernal and Mason, 1960], and drops with increasing μ_{s} and μ_{r} to a value of ≈ 0.54 [Santos et al., 2020]. If d_{m} is the mean particle diameter, the effect of cohesion, particularly for $d_{\mathrm{m}} < 50\ \mu$m was previously shown to be of decreasing density [Parteli et al., 2014b] and is simulated here by comparing the same samples $[a - i]$, with the mean of particle size distributions ranging from $\approx 4\ \mu m - 50\ \mu$m. Fig. (5.4) showcases the peculiar behavior reported where with increasing Bo (Bond number), the chain-like structures become prevalent and thus increase the voids within the packing. Bond number by definition is the ratio of the cohesive force to the gravitational force and is given by Eqn. (5.4).

The simulations are carried out by randomly packing the size distributed grains of all the samples to an initial density $\phi = 0.2$, that is they are not touching each other and at $t = 0$ settled under gravity. The dimensions of the box are $L_x = L_y = 12d_{\mathrm{m}}$. L_z in the vertical direction is set large enough to generate a packing height $\approx 30d_{\mathrm{m}}$. Once the grains settle, and the kinetic energy dissipated, we can compute the packing fraction of the sediment bed as,

$$\phi = \frac{\sum_i \pi d_i^3}{6L_xL_y\left(H_u - H_l\right)} \tag{5.13}$$

where (H_u, H_l) are chosen to be $(0.3, 0.7)z_{\mathrm{max}}$, with z_{max} being the highest grain in the vertical bed. Fig. (5.5) shows the comparison between the experimental packing fractions and the ones obtained from our DEM simulations for the samples $[a - i]$. The simulations for monodisperse grains are also included for relevance. The packing fraction for larger grains converges to around $\phi \approx 0.55$ as predicted for frictional spherical grains, while the lowest value for $\phi(d_{\mathrm{m}} = 5\ \mu\mathrm{m}) \approx 0.30$. The results show reasonably good comparison, even using a linear Hooke's model in our model. This validates the parameters for cohesion, rolling friction and proceed to the pile problem validation using with the same parameters.

5.2.4 Model validation - granular pile problem

When particles are poured, they generally form a heap. The angle between the sloping side and the horizontal of a stable pile is usually referred to as

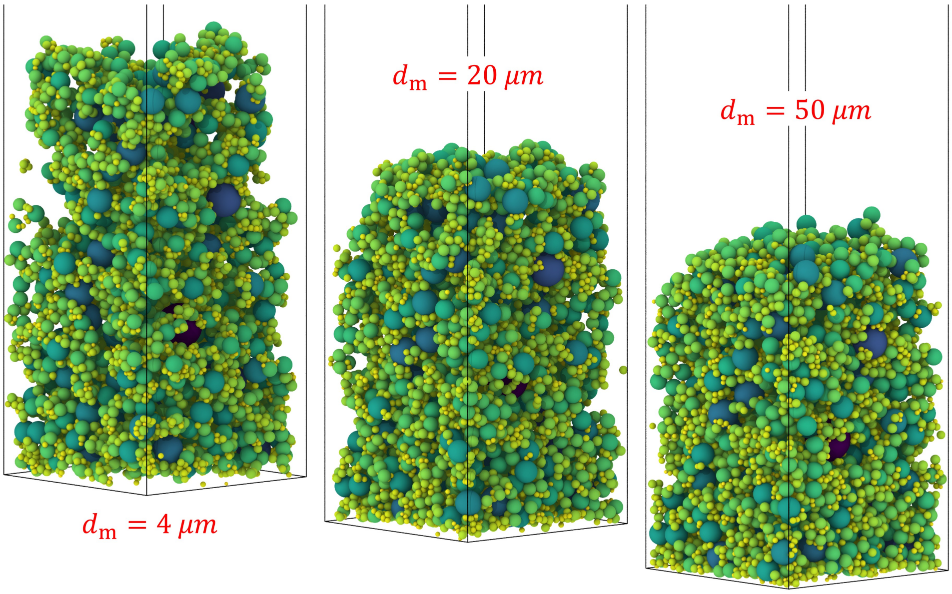

Figure 5.4: Packing behavior for various size ranges, with simulation box domain $L_x \times L_y = 12d_m \times 12d_m$. The effect of cohesion increases for smaller grains producing tree/chain-like structures.

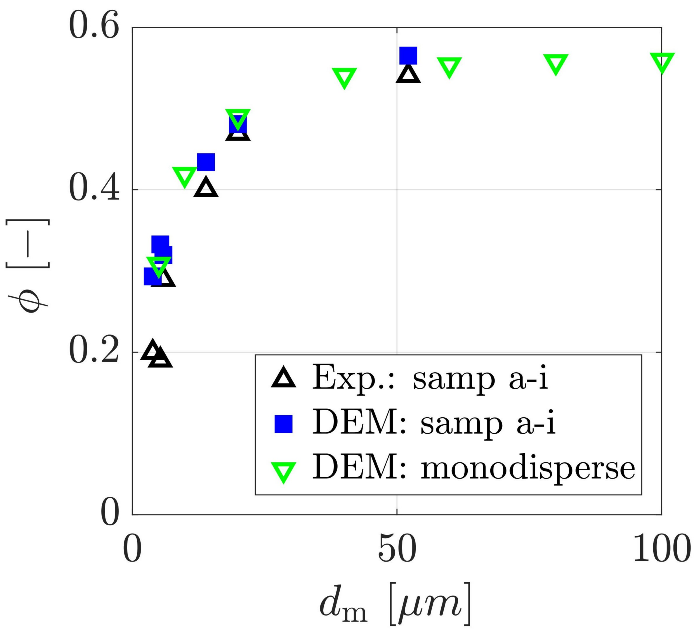

Figure 5.5: The packing fraction as a function of the mean particle diameter d_m, for both monodisperse and polydisperse systems and compared with experiments [Parteli et al., 2014b]

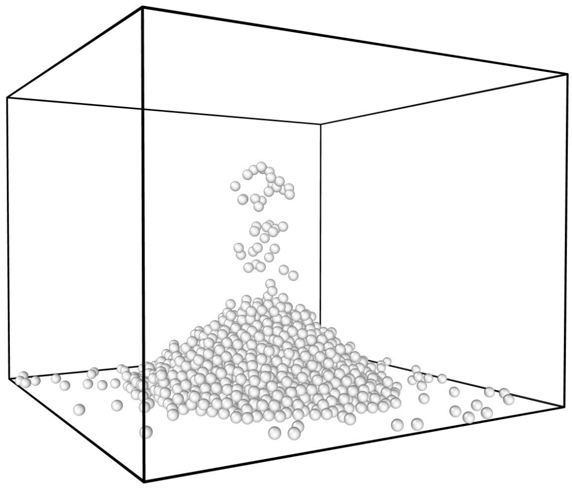

Figure 5.6: A granular pile in the DEM simulations formed by the systematic pouring of grains in an open-wall domain.

the *Angle of Repose* and is often used as a measure of the flowability of the granular material [Geldart et al., 2006]. The effect of cohesion and the rolling friction has been previously studied through numerical simulations, both aiding in steeper slope angles [Hassanzadeh et al., 2020, Elekes and Parteli, 2021]. Fig. (5.6) shows a granular pile forming under gravity, and about $N = 25000$ grains are poured from the top, where the particles are generated in a small volume. Once the pouring process is complete, we then measure θ_r over the 2D projection of the simulation, as described in [Elekes and Parteli, 2021].

Fig. (5.7) is recreated as in Fig. (2) of [Elekes and Parteli, 2021] using the data available from experiments. The major difference between the 2 studies are the way the contact model is described, with the linear Hooke model in our case, while[Elekes and Parteli, 2021] use a non-linear Hertzian model with the glass parameters. Albeit this difference with the right parametrizations, there is a good fit to their study, while noting the usual scatter that is seen in the experimental measurements [Wong, 2000, Chen et al., 2015].

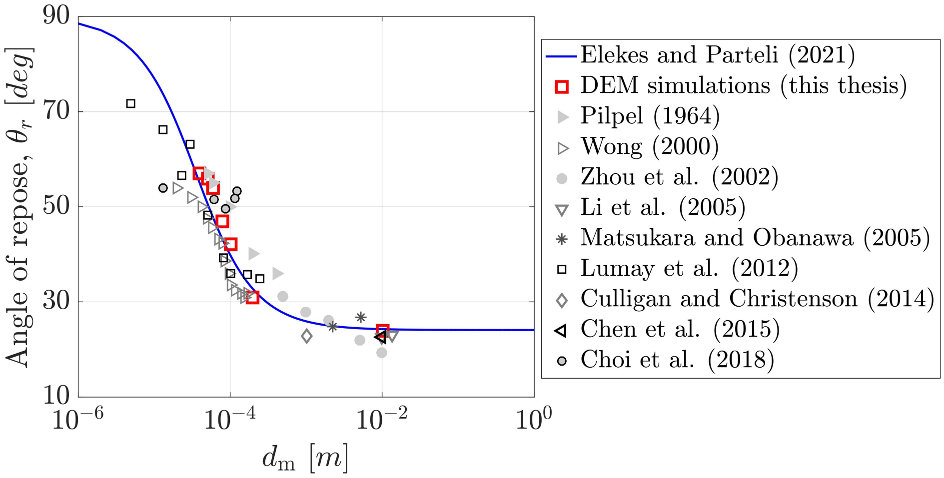

Figure 5.7: The angle of repose test using DEM simulation for monodisperse grains provides a trend in agreement with most experiments (data obtained from [Elekes and Parteli, 2021])

5.2.5 Turbulent fluctuations

Turbulent flow is a complex and chaotic phenomenon characterized by irregular and unpredictable motion of fluid elements. Turbulent fluctuations here, refer to the variations in velocity in all 3 directions within the flow field. We consider a *Lagrangian stochastic* model for turbulence studied previously by [Pope and Chen, 1990, Sawford, 1991, Reynolds, 2003]. The fluctuations were previously ignored for the sand simulations, but the susceptibility of finer dust to turbulent diffusion makes it a critical aspect. The grain trajectories are not deterministic any more, and follows the model which is built on a Markov process assumption [Wilson and Sawford, 1996].

Let $\bar{u}, \bar{v}, \bar{w}$, represent the time-averaged velocities in the x, y, z directions, and u', v', w' be the respective fluctuating components. The Reynolds Averaged Navier Stokes (RANS) equation can be written as,

$$\rho_f \bar{u}_j \frac{\partial \bar{u}_i}{\partial x_j} = \frac{\partial}{\partial x_j} \left[-\bar{p}\delta_{ij} + \mu \left(\frac{\partial \bar{u}_i}{\partial x_j} + \frac{\partial \bar{u}_j}{\partial x_i} \right) - \rho_f \overline{u_i' u_j'} \right] + \rho_f \bar{F}_i \tag{5.14}$$

where the new term $\left(\rho_f \overline{u_i' u_j'}\right)$ is referred to as the Reynolds stress, the ap-

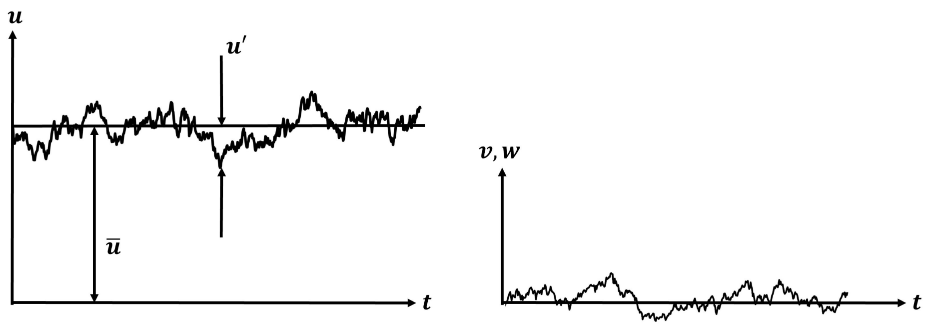

Figure 5.8: The temporal fluctuations arising in the measurements of the flow in x, y, z as u', v', w'

proximations of which give rise to the various turbulence closure methods. We can break down the fluid velocity into it's mean and fluctuating components,

$$u = (\overline{u} + u')\,;\ v = (\overline{v} + v')\,;\ w = (\overline{w} + w')\,; \tag{5.15}$$

Every particle that is exposed to the fluid flow is attached a *tracer* that stores information regarding the velocity fluctuation that it experiences (u', v', w') as a per-atom property. This helps us predict the turbulent components for the next time iteration using the following equations.

The mean part is what we computed in the mean description of the field in Section (2.4). The fluctuating component is given following [Van Dop et al., 1985, Wilson and Sawford, 1996, Nemoto and Nishimura, 2004, Kok and Renno, 2009] as,

$$u'\,(t + dt) = u'\,(t) - \frac{u'\,(t)}{T_{\mathrm{L}}}dt + n_{\mathrm{G}}\sigma_u\sqrt{2dt/T_{\mathrm{L}}} \tag{5.16}$$

with the discretized solution relevant to our DEM simulations as provided by [Kok and Renno, 2009],

$$u'\,(t + \Delta t) = u'\,(t)\exp\left(-\Delta t/T_{\mathrm{L}}\right) + n_{\mathrm{G}}\sigma_u\sqrt{2}\left[1 - \exp\left(-\sqrt{\Delta t/T_{\mathrm{L}}}\right)\right] \tag{5.17}$$

A similar equation also holds for v', w' with their respective parameters σ_v, σ_w which are the turbulence intensities in prescribed direction. Here, Δt is the

model time-step, T_{L} the Lagrangian timescale, n_{G} is a randomly generated Gaussian parameter with zero mean and unit standard deviation.
The assumption of a neutral surface layer for turbulence implies that the intensity is proportional to the friction velocity [Hunt and Weber, 1979, Shao, 1995],

$$\sigma_u = \sigma_v \approx 1.4u_* \tag{5.18}$$

while the turbulence intensity for the vertical fluctuations,

$$\sigma_w \approx 2.5u_* \tag{5.19}$$

The Lagrangian timescale T_L is given as,

$$T_{\mathrm{L}} = \frac{z}{2\sigma_w} = 0.4\frac{z}{u_*} \tag{5.20}$$

5.2.5.1 Fluctuations in the laminar sublayer

The turbulent fluctuations illustrated above is considered for the turbulent layer. But for the interpretation inside the viscous sublayer, no study in the past has given any special consideration. Following up with [Chkhetiani et al., 2012], we present a scheme for the turbulence intensity as below, If δ^{v} is the viscous sublayer thickness ($\approx 5\nu/u_*$),

$$\sigma_u = \sigma_v = \begin{cases} 1.4u_*, & \text{if } (z-h_0) > \delta^{\mathrm{v}} \\ 1.4u_*(z-h_0)/\delta^{\mathrm{v}}, & \text{if } (z-h_0) \leq \delta^{\mathrm{v}} \end{cases} \tag{5.21a}$$

$$\sigma_w = \begin{cases} 2.5u_*, & \text{if } (z-h_0) > \delta^{\mathrm{v}} \\ 2.5u_*\frac{(z-h_0)}{\delta^{\mathrm{v}}}, & \text{if } (z-h_0) \leq \delta^{\mathrm{v}} \end{cases} \tag{5.21b}$$

where z is the vertical height of the particle, h_0 the bed height. Eqn. (5.21) yields a continuous function for turbulence intensity, which increases linearly with z in the sublayer, while it is just proportional to u_* in the turbulent limit. For example, $z = h_0, \sigma_w = 0, z = \delta^{\mathrm{v}}, \sigma_w = 2.5u_*$, thus preserving the continuity.

5.3 The problem of initiation threshold

When a few grains are dislodged by the wind drag or turbulent fluctuations, very close to the threshold condition, they rock, roll and eventually available for transport. This initiation then potentially propagates itself to hop and splash further to kick-off saltation (particularly for $d > 50$ μm [Shao 2008]). On the other hand, for $d < 20$ μm we observe the suspension of grains. This problem has been previously explored for decades [Bagnold, 1941, Greeley and Iversen, 1987, Shao and Lu, 2000], and we start from the very fundamentals to understand the effects from the wind shear, cohesion, lift forces, turbulent fluctuations, the surface roughness, stochastic nature of forces. Finally we try to converge the story to realize Aerodynamic entrainment for some bi-disperse systems to include dust and sand, to understand what really initiates the emission transport and what sustains it, under varying surface characteristics. To this end, we first begin with a Quasi-2D set-up as shown in Fig. (5.10) so as to compare our observations with previous studies.

We use monodisperse grains of diameter d, radius R, with the bottom 10 grains frozen (like in Chapter 4), the system domain being $L_x \times L_y \times L_z = 10d \times 1d \times 50d$. The bed height by definition, $\phi(h_0) = \phi_b/2$ as before would mean $h_0 = 0.85d$. The configuration when viewed from a geometric point of view as in Fig. (5.11), can be then used to balance the forces to arrive at the Bagnold threshold.

Considering only the gravity $\mathbf{F}^g$ and the aerodynamic drag force $\mathbf{F}^d$, the net moment created when the moment of drag just exceeds that from gravity around the pivot point $\boldsymbol{P}$ initiates the initial rotation. This is followed by the climb over the grain, and the negative feedback to the flow, however small could inhibit the flow, thus generating a *rock-and-roll* regime.

$$r_d\mathbf{F}^{\mathrm{d}} - r_l\mathbf{F}^{\mathrm{g}} = 0 \tag{5.22}$$

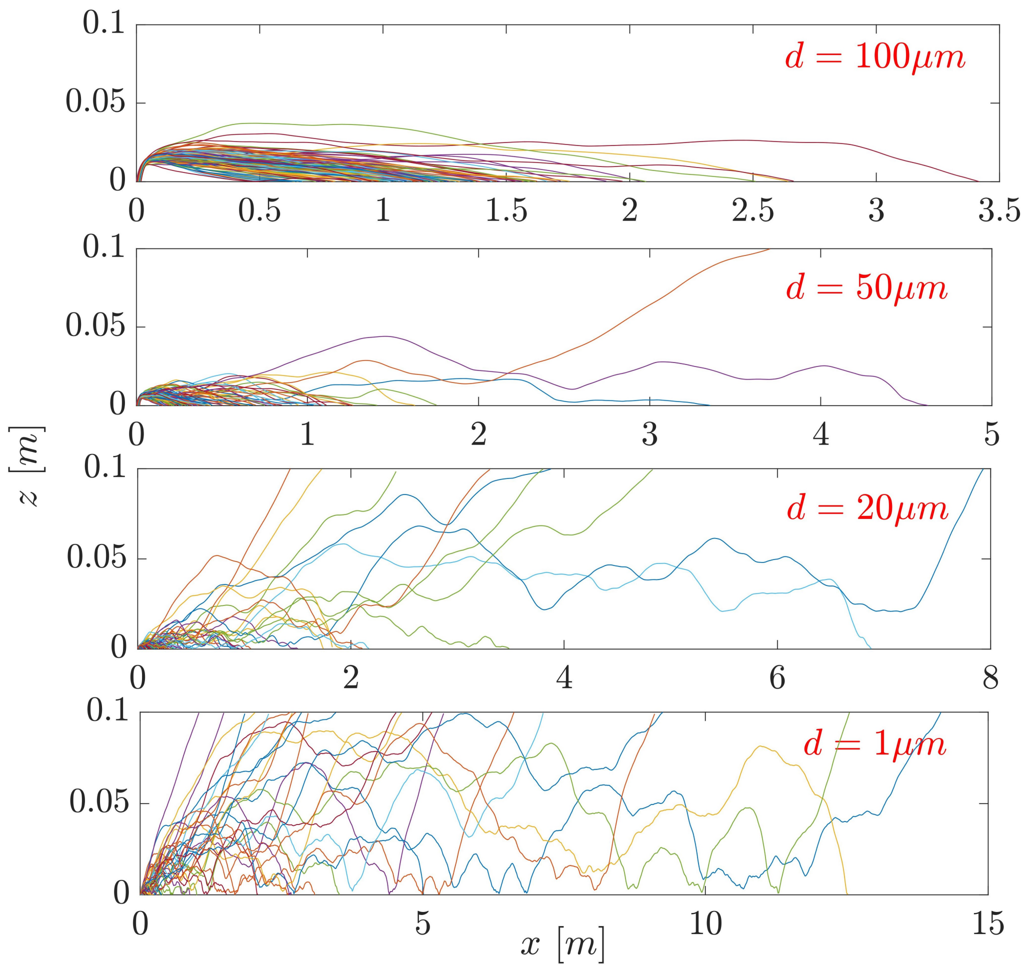

Figure 5.9: The trajectories for various grain diameters for $u_* = 0.30$ m/s demonstrate the fluctuating paths the finer grains take as compared to large sand grains

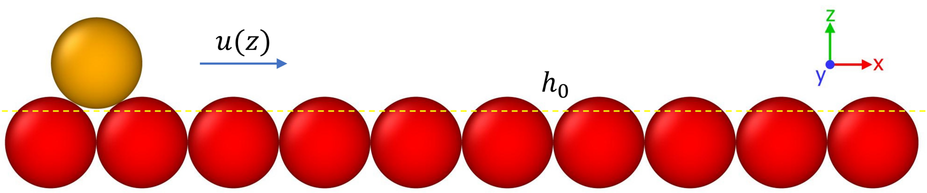

Figure 5.10: A simple Quasi-2D grain configuration with the wind in x, motion only in x, z, while it is locked in y

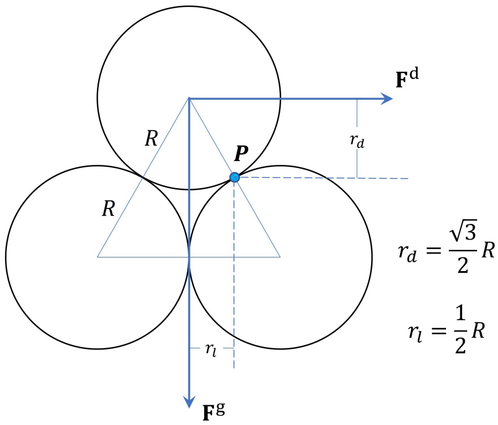

Figure 5.11: A simple Quasi-2D grain configuration with the wind in x, motion only in x, z, while it is locked in y

Rough regime

where r_d and r_l are the respective distance of the acting forces from the rotating axis. The equilateral triangle in Fig. (5.11), gives $r_d = \sqrt{3}R/2$ and $r_l = R/2$. If we consider U_s as the wind-speed acting at the center of the grain, thus expanding,

$$\left(\frac{\pi}{8}d^2\rho_f C^\mathrm{d} U_s^2\right)\frac{\sqrt{3}R}{2} = \left(\frac{\pi}{6}d^3\rho_\mathrm{p} g\right)\frac{R}{2} \tag{5.23}$$

$$U_\mathrm{s}^2 = \left(\frac{4}{3\sqrt{3}}\right)\sigma_\mathrm{p} g d \tag{5.24}$$

where σ_p is the ratio of the grain and air density. For large grains, a rough regime is developed near the grains, with negligible viscous effects. That is for $\mathrm{Re} \to \infty, C^{\mathrm{d}} \approx 1$ and the surface roughness is approximately $z_0 = d/30$, with a logarithmic wind profile. Thus, the fluid threshold friction velocity $u_{*,\mathrm{ft}}$ is given as,

$$u_{*,\mathrm{ft}} = \sqrt{\left(\frac{4}{3\sqrt{3}}\right) \sigma_{\mathrm{p}} g d \left(\frac{\kappa}{\ln 15}\right)^2} \tag{5.25}$$

Following previous notations,

$$u_{*,\mathrm{ft}} = A_{\mathrm{ft},\infty} \sqrt{\sigma_p g d} \tag{5.26}$$

where the constant $A_{\mathrm{ft},\infty} \approx 0.13$. Note that it is independent of the flow conditions Re, thus the Bagnold prediction works well for only large grains.

Smooth regime

Following up from Eqn. (5.24), the effect the Reynolds number is more pronounced for small grains, as $\mathrm{Re} \to 0, C^{\mathrm{d}} \to 32/\mathrm{Re}$ for the flow in Stokes regime. The transition is clearly seen in fig. (5.12), where for low Re,

$$z_0 = \frac{\nu}{9u_*} \tag{5.27}$$

The smooth regime, and the non-negligible viscous effects thus lead to an increase in the threshold velocity. This behavior is captured in Fig. (5.13) where the constant $A_{\mathrm{ft},\infty}$ increases for smaller Re, converging to a value of $A_{\mathrm{ft},0} \approx 0.20$. That is for very fine grains,

$$u_{*,\mathrm{ft}} = \sqrt{\left(\frac{4}{3\sqrt{3}}\right) \sigma_{\mathrm{p}} g d \; f\left(\mathrm{Re}\right)} \tag{5.28}$$

$$u_{*,\mathrm{ft}} = A_{\mathrm{ft},0} \sqrt{\sigma_{\mathrm{p}} g d} \tag{5.29}$$

Bagnold presumed this is the cause for the drastic increase in $u_{*,\mathrm{ft}}$ for dust [Bagnold, 1941], which we now know is because of cohesive forces, but let's

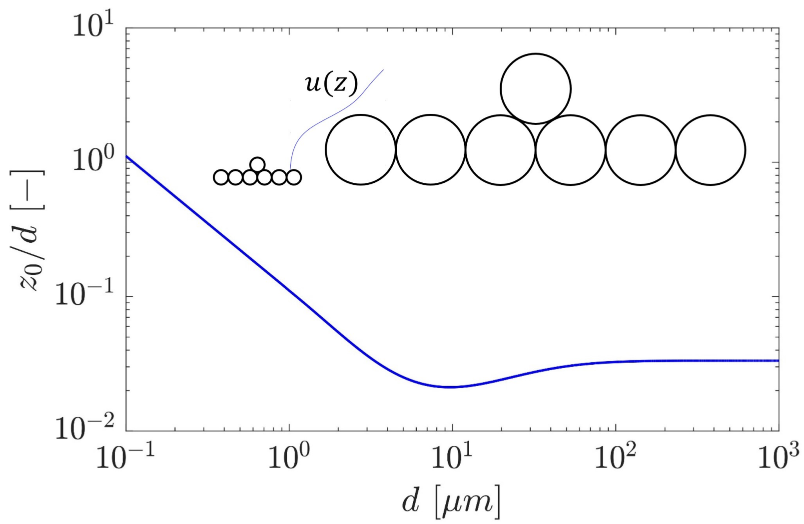

Figure 5.12: The hydrodynamic roughness as a function of the Reynolds number, or indirectly the grain diameter [Nikuradse, 1933, Cheng and Chiew, 1998].

get back to it later when we consider cohesive grains.

To close the discussion, involving the flow effects on the threshold, we see in a hypothetical situation when the viscous sublayer along with the choice of drag coefficient (C^{d}) has on the divergence from Bagnold curve. This shows the Bagnold condition is only held in the absence of a viscous sublayer, and when C^{d} is taken as in the turbulent limit of $\mathrm{Re} \to \infty$.

Lift and turbulent fluctuations

Building upon this, if we now add the lift forces as in Section (2.2),

$$\mathbf{F}_d r_d + (\mathbf{F}_l - \mathbf{F}_g)\, r_l = 0 \tag{5.30}$$

which using the similar expansion as above, results in a similar expression as Eqn. (5.24), but with a lowered $A_{ft,\infty} \approx 0.12$, and similar transition from rough to smooth regimes. This is elucidated in Fig. (5.15) along with the insignificant effects from turbulent fluctuations for small grains. The

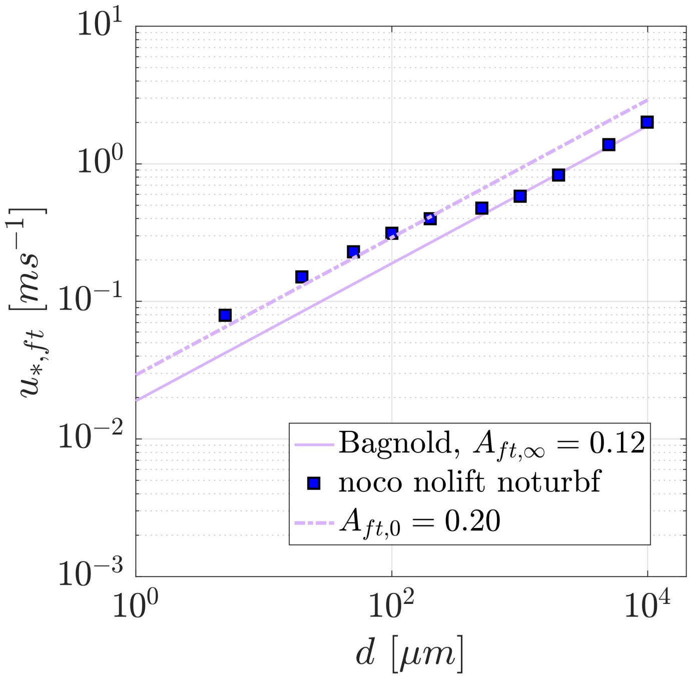

Figure 5.13: The threshold velocity shown for a range of non-cohesive grain sizes, diverging from the Bagnold formula when transitioning from rough to smooth regime

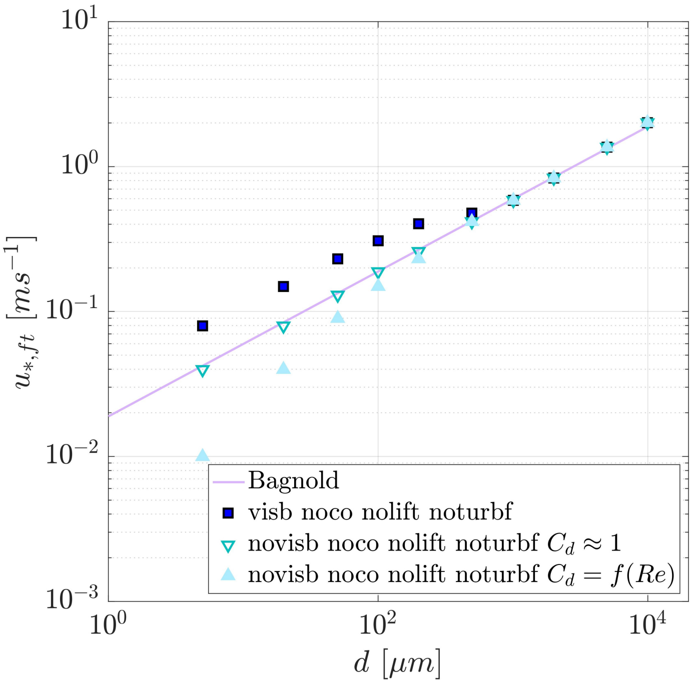

Figure 5.14: The threshold velocity dependency on the consideration of a viscous sublayer close to surface, and $C^{\mathrm{d}} = f(\mathrm{Re})$

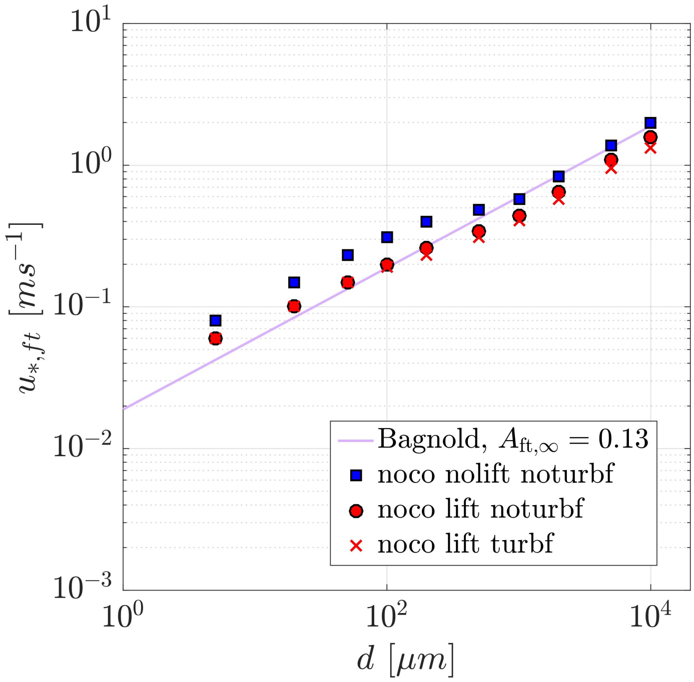

Figure 5.15: Enhanced effects of lift and turbulent fluctuations on the initiation of transport

fluctuation intensity is very small at threshold speeds for the fine grains, as well as the description in the viscous sublayer goes to 0 at very small heights.

Cohesion

As been noted multiple times before, presence of cohesive forces increase the transport threshold for fine dust grains. Due to limited experiments to test this behavior, we further expand our analysis to incorporate the van der Waals force as the only dominating means for cohesion. [Shao and Lu, 2000] gave an expression to describe it in theory,

$$u_{*,\mathrm{ft}} = A_{\mathrm{ft}} \sqrt{\left(\sigma_{\mathrm{p}} g d + \frac{\gamma_{\mathrm{shao}}}{gd} \right)} \tag{5.31}$$

where the constant $A_{\mathrm{ft}} \approx 0.11$.

The threshold values in Fig. (5.16) show a clear divergence for with and

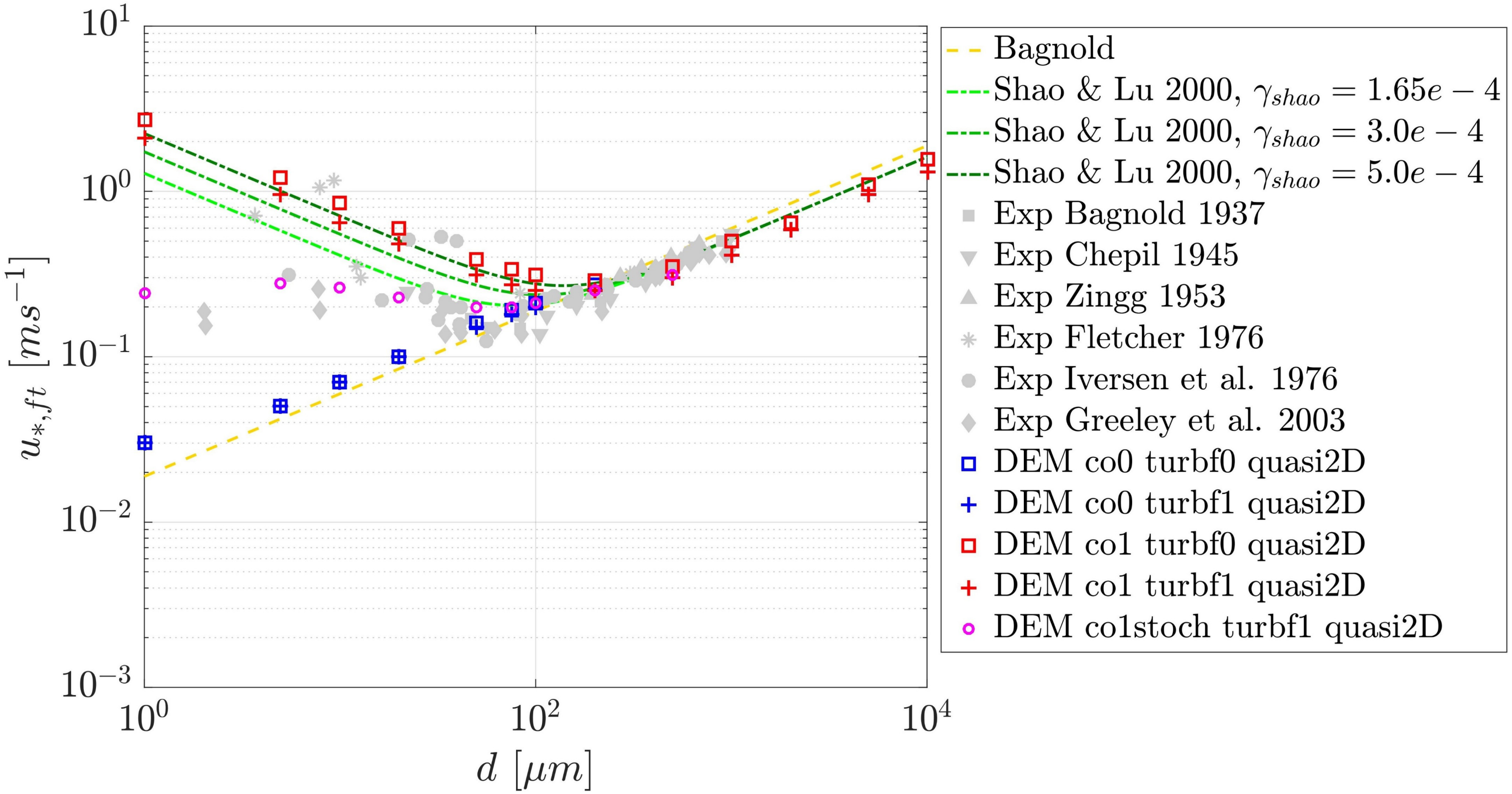

Figure 5.16: Effects on transport threshold due to cohesion and turbulence fluctuations, with the DEM results following the prediction by [Shao and Lu, 2000]. Also shown are cohesionless simulations and a special case of stochastic cohesion [Shao and Klose, 2016]. The minimum threshold is observed for around $d \approx 100$ μm

without cohesion around $d \approx 100\ \mu$m, thus confirming the prediction by [Shao and Lu, 2000]. The cohesionless grains follow the Bagnold trend quite well, that is for larger grains all the studies collapse due to the low effect from cohesion. Their study fitted a value of γ_{shao} between $1.65 \times 10^{-4} - 5.0 \times 10^{-4}$ kg/s^2. The DEM results with the full description of the flow (+) with the turbulent fluctuations fall well within this prediction (note here the turbulent description inside the viscous sublayer 5.21). However, the scatter from the experimental observations mainly arising from the difficulty in measuring aeolian thresholds for fine dust grains. [Fletcher, 1976, Iversen et al., 1976] are some of the measurements which are consistent with the results.

However, the cohesive forces are stochastic in nature as suggested by [Shao and Klose, 2016], which they based on the data from [Zimon, 2012]. Thus they speculated that there is always free dust available over the bed surface for emission. We follow a similar scheme where in our case F^c_{ij} follows a log-normal distribution,

$$p(\mathrm{F}^c_{ij}) = \frac{1}{\mathrm{F}^c_{ij}\sqrt{2\pi}\sigma_{\mathrm{c}}} \exp\left(-\frac{1}{2}\left[\frac{\log(\mathrm{F}^c_{ij}) - \mu_{\mathrm{c}}}{\sigma_{\mathrm{c}}}\right]^2\right) \tag{5.32}$$

where μ_{c} is the mean of $\log(\mathrm{F}^c_{ij})$ and σ_{c} is the variance. From Eqn. (2.20), for particles in contact $\delta_{ij,\mathrm{n}} > 0$ we can rewrite it as,

$$\mathrm{F}^{\mathrm{c}}_{ij} = 2\pi d_{\mathrm{eff}}\gamma_{\mathrm{s}} \tag{5.33}$$

Thus, the mean of the log-normal distribution is,

$$\mu_{\mathrm{c}} = \log(2\pi d_{\mathrm{eff}}\gamma_{\mathrm{s}}) \tag{5.34}$$

Fitting the data of [Zimon, 2012] for glass particles, the variance is approximated as,

$$\frac{\sigma_{\mathrm{c}}}{\sigma_{\mathrm{c}0}} = \left(\frac{d_0}{d}\right)^{b_{\mathrm{c}}} \tag{5.35}$$

where the constant $b_c \approx 0.33$, $d_0 = 100\ \mu m$ is a scaling diameter, $\sigma_{c0} \approx 1$ is the σ_c for d_0. The free-dust scenario then plays out at the lower limit of F^{c}_{ij} as,

$$\mathrm{F}^{c,low}_{ij} = 2\pi d_{\mathrm{eff}} \gamma_s \exp\left[-\sigma_{c0}\left(d_0/d\right)^{b_c}\right] \tag{5.36}$$

The (o) indicate the threshold values under the influence of stochastic cohesion, which reaffirm the predictions of [Shao and Klose, 2016]. This is particularly interesting to address the problem of aerodynamic entrainment in the absence of saltation as previously shown by [Shao et al., 1993, Loosmore and Hunt, 2000, Roney and White, 2004, Macpherson et al., 2008]. We conclude the study for monodisperse spheres, with a detailed study of the fluid threshold curve which has huge implications in understanding the different modes of saltation and dust emission which we see in Chapter (6).

5.4 Bidisperse systems - supply limited conditions

The nature of initiation as we saw earlier is easier to attribute for monodisperse grains than for a bidisperse or polydisperse sand-dust bed. Also, the scenario when a thick layer of dust is covering the sand bed as far as the transport initiation is sought, the behaviour would be exactly that of a monodisperse dust bed. The threshold conditions for such cases was already shown in Fig. (5.16). As can be seen in Fig. (5.17), the main attributes that lead to emission of dust grains over supply limited surfaces much below the *monodisperse threshold* are -

(i) The roughness element that increases the height the dust particle is exposed to the wind.

(ii) The exposed particles might not be part of the developing viscous sublayer, but protruding out of it and hence susceptible to increased turbulent fluctuations.

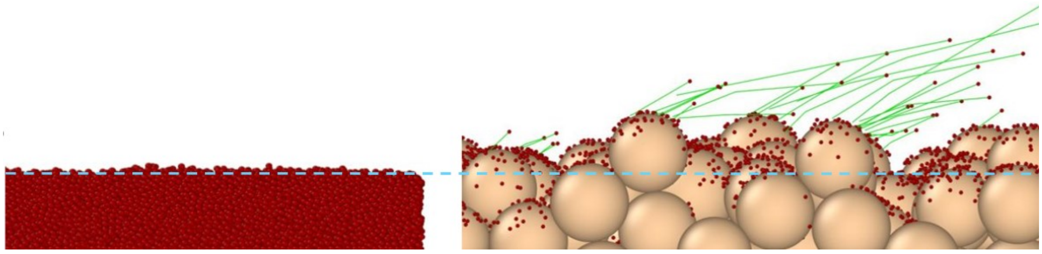

Figure 5.17: Monodisperse dust bed (d_{10}) as compared to limited dust over the sand (d_{200}) bed, individual dust grain emission is observed for $u_* \approx 0.30$ m/s.

Under similar wind conditions in Fig. (5.17), the exposed dust grains in the monodisperse are located at $z_{\rm mo}$, experiencing $u(z_{\rm mo}), \sigma_{\rm u,v,w} \propto (z_{\rm mo} - h_{\rm b})/\delta_s$. While in the bidisperse situation, the dust grains are coated on sand grains at higher heights that is, $z_{\rm bi} > z_{\rm mo}$, with $u(z_{\rm bi}), \sigma_{\rm u,v,w} \propto u_*$ with the grains potentially placed outside the viscous sublayer under certain wind conditions. This understanding leads us to inspect the limited conditions of dust availability, which necessarily that leads to particle transport at a significantly lower threshold. This very well depends on how the dust is dispersed over the sand, and would need further enquiry of such phenomena through field observations. This could also have geological implications on the early onset of stability of the loess formation [Tsoar and Pye, 1987] in semi-arid environments.

Fig. 5.17 shows the scenario for $u_* = 0.30$ m/s over a monodisperse (10 μm dust grains) and bidisperse bed (10 μm dust dispersed over 200 μm sand). The entrainment threshold for monodisperse 10 μm grains is ≈ 0.60 m/s, but dust entrainment is observed for the bidisperse case well below the threshold for monodisperse systems. Also to note is that, the viscous sublayer thickness for $u_* = 0.30$ m/s is around one sand grain diameter (200 μm) and the dust was still initially submerged in the viscous layer with minimal turbulent fluctuations. This would support the idea of emission of PM_{10} in semi-arid to arid environments below threshold conditions [Macpherson et al., 2008]. That is to add to the argument from [Shao and Klose, 2016], it is not just the availability of free dust that lowers the threshold, but also the limited availability of dust poses a significant effect which is not known yet. To this end, we take it up in the next chapter which is dedicated to studying the emission mechanisms under supply limited conditions.

To summarize, in this chapter we explored the additional modeling aspects of cohesion along with the concept of reduced cohesion model which gives us a significant computational edge in simulating fine dust grains. We also included the effects from stochastic turbulent fluctuations, rolling resistance and find their role to be crucial in modeling mineral dust. Through parametrization, followed by model validations we then showcased the various roles of the forces on the fluid threshold and finally observed that over supply limited surfaces, dust emission persists below the observed threshold for the monodisperse set-ups, thus needing a careful investigation in the next chapter.

Chapter 6

Dust emission mechanisms over supply limited surfaces

6.1 Direct aerodynamic entrainment or saltation bombardment?

It is currently a well accepted that the entrainment of dust (especially $<$ 20 μm grains) is mainly through saltation bombardment or aggregate disintegration phenomena [Gillette, 1974, Shao et al., 1993, Alfaro et al., 1997, Shao, 2008]. [Loosmore and Hunt, 2000] investigated the direction entrainment and concluded that although direct entrainment occurs at nominal wind speeds, it is insignificant to be considered as a major mechanism. However, recent studies have pointed to the role of direct entrainment and suspension even for PM_{10} grains. [Li et al., 2020] recently explained how turbulent fluctuations could enhance direct entrainment ($d > 40$ μm) but the process is not well understood for fine grains where there is an interplay between cohesion and the turbulent fluctuations.

[Kjelgaard et al., 2004, Sharratt and Lauer, 2006] provide evidence to the direct suspension of dust from loessial soils or agricultural fields. [Roney and White, 2004, Macpherson et al., 2008] point to the entrainment over dried lake soils, and desert surfaces well below the saltation thresholds, also supported by further studies [Sweeney and Mason, 2013, Újvári et al., 2016, Wu et al., 2018]. The effects of soil texture on the PM_{10} emission was inspected through wind tunnel simulations and showed how the emission efficiency is relatively higher for sandy-loam soils than loamy sand soils [Zuo et al., 2024]. [Du et al., 2024] goes further and observes that direct entrainment of $< PM_{10}$ grains is continuously seen even before the onset of saltation. However they also note that if the dust supply is limited on the surface, it should be entrained in a short span. But in natural environments, strong winds usually lead to surface renewal [Zhang et al., 2016] and thus providing a continuous supply of dust.

These raise some concerns regarding the reason for movement of fine grains, in the regime where cohesion results in strong inter-particle bonds. Thus we explore the case of low concentrations of dust available over the sand surface initially, as we described towards the end of Section (5.4) with no clear differentiation between the modes of transport. Although the three general mechanisms of emission that we explored in Section (5.1) are theoretically predicted, as per our knowledge thorough investigations through direct numerical simulations have not been attempted in the past.

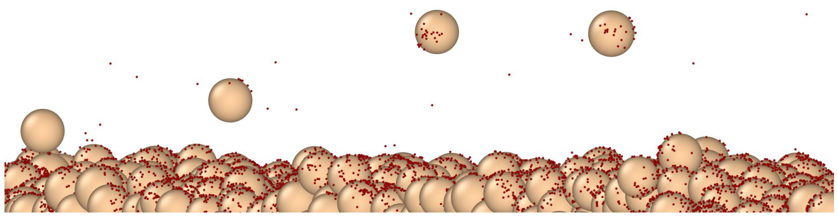

Figure 6.1: Supply limited case of dust settled over a sand bed, with the aggregates in motion after the cluster mapping is realized

Before we go further, we elucidate two additional features to the model, (i) Cluster mapping - which is necessary to realize the dust transport, the phenomena of aggregate formation/breakage; (ii) Shadow region mapping - the presence of bigger grains which diminish the wind drag for the downstream fine dust grains in direct contact.

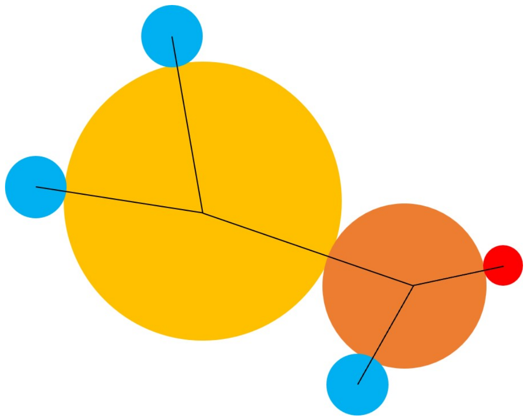

Figure 6.2: Cluster/chunk representation holds key in accurately modeling sand-dust systems

6.1.1 Cluster mapping

The grains due to the attractive cohesive forces can form aggregates, and we allow this by adapting the flow computations to include these clusters. A cluster by definition is a set of grains who form overlaps with atleast one grain in the cluster, or in other words, a set of grains who share a path without break between the centers. This is shown in Fig. (6.2).

However, it is to be noted that, by definition the largest cluster is the static bed itself, and so as a simplification they are considered as individual particles. A cluster is thus, which has broken away from the bed.

The following quantities are computed every iteration and stored as a per-atom quantity, as shown in the below table.

Id_{p}	Unique particle ID
Id_{c}	Cluster ID
Id_{b}	Cluster ID, but of the bed (identified with a flag)
N_{c}	Number of particles in a cluster

First, we define the group for which the cluster quantities are computed. The computational burden of the cluster mapping is greatly reduced by just defining a region for the group, which is a few particle diameters $\approx 3d_{\mathrm{m}}$) below the bed height. A single particle ejected from the bed is also by definition a cluster with $N_\mathrm{c} = 1$. The following *modules* are part of the cluster property computations pre-defined in LAMMPS.

Module: compute cluster/atom - Any 2 particles are said to be in a cluster if ,

$$|\mathbf{r}_i - \mathbf{r}_j| <= \frac{1}{2}(d_i + d_j) \tag{6.1}$$

Module: compute chunk/atom - It provides the integer cluster IDs (1,N_cmax). These per-atom cluster IDs are important, as they are further used by the other modules to gather relevant information about the cluster.

Module: compute property/chunk - Provides N_c and can compress the cluster IDs, so that they always increment by 1.

With these per-atom quantities identified, the wind profile is extracted just like before, but by considering a cluster as an individual grain with updated properties which are,

The diameter of the cluster (d_c) is found by computing the radius of gyration ($d_\mathrm{c} = 2R_\mathrm{g}$),

$$R_\mathrm{g}^2 = \frac{1}{m_\mathrm{c}} \sum_{i=1}^{N_\mathrm{c}} m_i (r_i - r_{com})^2 \tag{6.2}$$

where r_i the position of the grains in the cluster and r_{com} is the center of mass position of the cluster in whole.

The mass of the cluster (m_c) is pretty straight-forward, that is the sum of masses of all the particles in a cluster system.

Module: compute com/chunk The center of mass of the cluster is used instead of the particle coordinates, and is computed by the module as,

$$cm_x = \frac{m_1 x_1 + m_2 x_2 + ...}{m_\mathrm{c}} \tag{6.3}$$

It follows similarly for the y and z coordinates.

Module: compute vcm/chunk This provides the center-of-mass velocity for the defined clusters, which is used instead in the relative velocity between the wind and the grain.

Most significantly, to achieve a realistic cluster motion, the computation for hydrodynamics is conducted on the grain which has the least Id_{c}. As the above quantities are reiterated as per-atom values, any of the particles in the cluster can access the necessary quantities. The same procedure is followed for the turbulent fluctuations.

The fluid-particle interaction for the clusters follows,

$$\mathrm{Re} = \frac{v_r d_{\mathrm{c}}}{\nu} \tag{6.4}$$

$$\mathbf{F}^{\mathrm{d}} = -\frac{\pi}{8}(d_{\mathrm{c}}^2 \rho_{\mathrm{a}} C^{\mathrm{d}} v_r \mathbf{v_r} \frac{m_i}{m_{\mathrm{c}}}) \tag{6.5}$$

where m_{c} is the total mass of the chunk, N_{c} the number of grains in the chunk, m_i the mass of individual grains.

6.1.2 Shadow region mapping

This computation is applicable for only the grains that are part of the bed at every iteration. It is assumed that the fine grains residing in the downstream region of a larger grain, is not exposed to the wind and thus is said to be in *"shadow"*. An experimental investigation was previously conducted by [Taneda, 1956] on the effects of wakes behind spheres at low Reynolds number. This is computationally realized by defining a *shadflag* as a particle property, which marks the dust grains whenever the below condition is met.

$$\mathrm{shadflag}_j = \begin{cases} 1, & \text{if } d_i > d_j \ \& \ (x_i - x_j < 0) \ \& \ \left(\Delta y_{ij}^2 + \Delta z_{ij}^2\right) < r_i^2 \\ 0, & \text{otherwise} \end{cases}$$

where $d_{i,j}, r_{i,j}$ are the grain diameters and radii respectively, $x_{i,j}$ their horizontal positions in the along-wind direction, $\Delta y_{i,j} = y_i - y_j$ the difference between their cross-wind positions, and $\Delta z_{i,j} = z_i - z_j$ the relative difference in their vertical positions. Thus it follows, if $(\mathrm{shadflag_i} = 1) \implies u(z) = 0$, that is the grains are excluded from any wind computations.

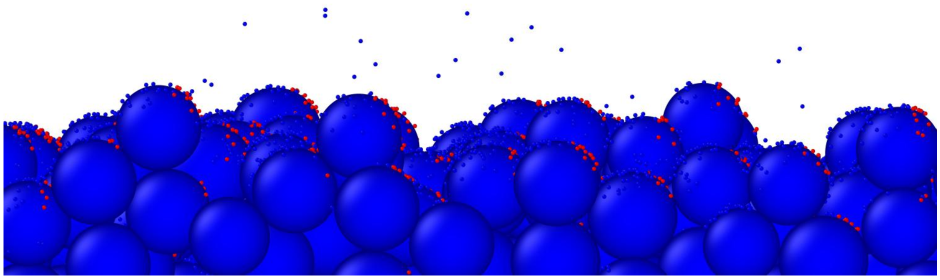

Figure 6.3: The red particles are said to be in shadow of the larger grain visualized in blue

6.2 Scaling the vertical dust flux

The DEM setup is initialized by settling 50,000 grains of dust of size $d = 10\ \mu m$ over the sand ($d = 200\ \mu m$) bed of lateral dimensions $(L_x \times L_y)/d_{200} = (100 \times 8)$. The dust grains are generated randomly over the bed with a packing fraction of 0.20, thus they are separated from each other. They are then settled under gravity and the viscous drag, with their initial downward velocities u_{z}^i equalling their respective precomputed terminal velocities. The simulation is started, and as the particles are entrained Fig. (6.1) then evolves with time and the vertical dust flux is computed, which is a quantitative indicator of the overall dust emission.

Estimates of the vertical dust flux F_{d} are amongst the largest uncertainty causes in climate models [Mahowald et al., 2014, Schepanski, 2018, Shao, 2008]. F_{d} is proportional to the wind velocity, with the scaling function often debated in literature. [Gillette and Walker, 1977] conducted extensive field experiments and observed a large scatter although observing a general increasing trend of the flux with u_*. [Nickling and Gillies, 1989, 1993] pointed out the importance of soil-surface textures and organized them to provide the scaling power $2.9 \leq n \leq 4.4$ [Shao, 2008].

$$F_d \propto u_*^n \tag{6.6}$$

the DEM simulations support $n \approx 4$, which will be seen later.

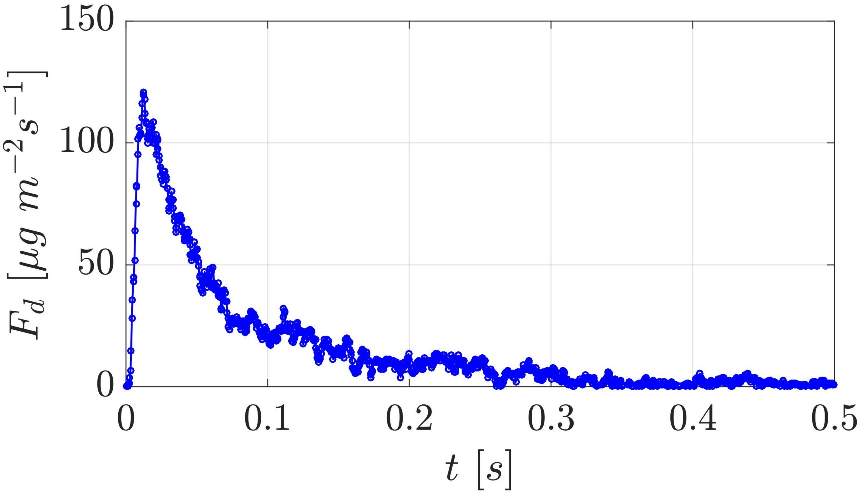

Figure 6.4: The dust emission as a result of an initial entrainment burst, hitting a peak and subsequently falling, as seen for $d_{10}d_{200}, u_* = 0.30\ m/s$

The vertical dust flux is computed using the scheme suggested by [Zhang et al., 2016] -

$$F_d = -K_p \frac{C(z_2) - C(z_1)}{z_2 - z_1} \tag{6.7}$$

where K_p is the turbulent diffusion coefficient approximated as,

$$K_p = u_* l_m \tag{6.8}$$

where l_m is the mixing length $\approx \kappa (z_1 + z_2)/2$.

Fig. (6.4) shows the initial burst of vertical flux, similar to those reported in [Zhang et al., 2016] and also [Shao et al., 1993, Loosmore and Hunt, 2000] also under limited supply of free dust. In the simulation, the cause was the direct entrainment of dust grains in the initial stages, followed much later by the saltating grains. Finally the source of dust in the bed was totally depleted, either blown away or a process we hereby call *"dust burial"*. We discuss this separately in the Section (6.2.2), as this has not been studied before.

Now we explain the role of direct entrainment when weighed with the role of saltating d_{200} grains in mobilizing dust (d_{10}). To this end, we further classify

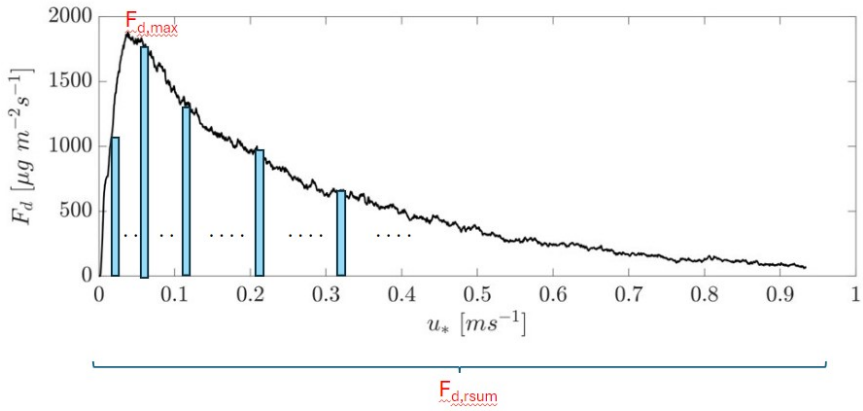

Figure 6.5: The peak emission flux and an cumulative flux calculated as a Riemann sum over the duration of emission are computed in every case

the experiments into -

(i) fr[1] - d_{200} grains are frozen (similar to the set-up in Section (4.3.1) of sediment availability)

(ii) fr[0] - all grains are mobile (nothing is frozen)

Although there exists no point of saturated state during emission with limited supply, we could extract two features from Fig. (6.4), a peak flux and an averaged flux over the duration of time, which is taken as a Riemann sum here. The peak emission flux is then given as,

$$F_{\mathrm{d,max}} = \max F_d(0, t_{\max}) \tag{6.9}$$

The Riemann sum,

$$F_{\mathrm{r,sum}} = \sum_{i=1}^{n} F_{\mathrm{d}}(t_i^*)\Delta t \tag{6.10}$$

where $\Delta t = t_i - t_{i-1}$ and $t_i^* \in [t_{i-1}, t_i]$.

6.2.1 Entrainment below saltation threshold

Fig. (6.6) reveals that the entrainment threshold for d_{10} is much below the usual *dynamic threshold* for the monodisperse as stressed already before.

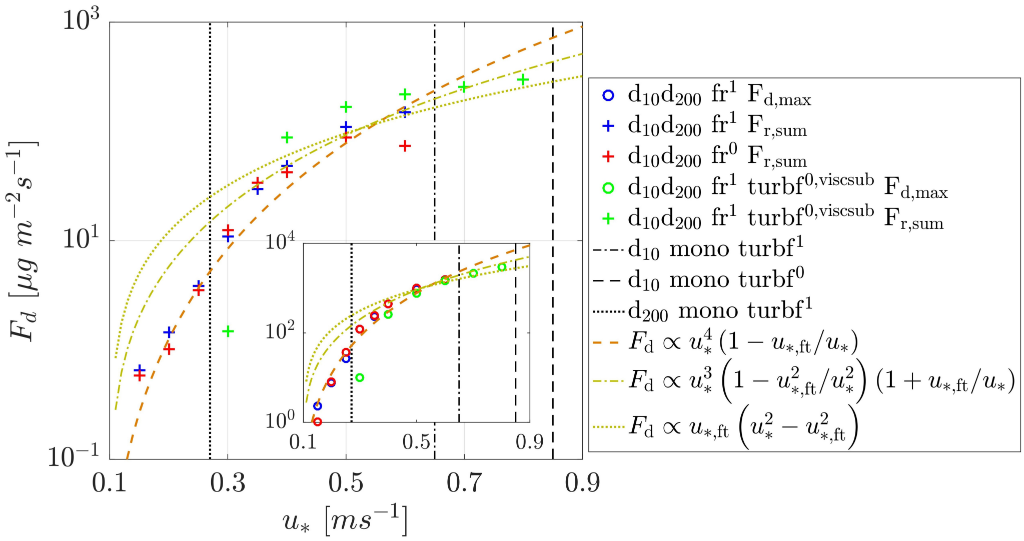

Figure 6.6: The vertical dust flux shown as a function of u_* with the averaged flux ($F_{\mathrm{r,sum}}$) in the main figure, while the peak values ($F_{\mathrm{d,max}}$) in the inset. $d_{10}d_{200}$ cases for fr^0, fr^0 as well including the special case with no turbulent fluctuations inside the viscous sublayer. The threshold shear velocities are marked for the monodisperse systems of d_{10} and d_{200}. The flux values fitted against Eqn. (6.11) provides a scaling law with an exponent value, $n = 4$. $u_{*,\mathrm{ft}} \approx 0.10\ ms^{-1}$ for 10 μm grains under supply-limited conditions.

This gives us an important insight into how in natural environments, particularly in semi-arid and arid areas with limited supply of dust, PM$_{10}$ grains are easily entrained for $u_* \approx 0.20\ m/s$ (although a small amount). This has been suspected by [Du et al., 2024] through field observations where the claim also is the direct entrainment of PM$_{10}$ grains much below the saltation threshold. [Zuo et al., 2024] also talks on a similar note, stressing on the primary emission during the initial stage of wind erosion.

Now the aspect with freezing the sand grains in Fig. (6.6) (fr^1 as blue points), does not significantly differ from that when all grains are erodible (fr^0 as red points). This further confirms the direct entrainment of the grains in the initial stage of simulation (before the peak) as the dominating mechanism. Although saltation picks up much later for fr^0, the dust source is depleted as well as buried through segregation. Interestingly for higher values of u_*,

$F_{\mathrm{r,sum}}$ is actually lower with the sand grains in the saltation regime. The scaling behavior for the supply limited condition, when fitted for $F_{\mathrm{r,sum}}$ values follow a fitted expression similar to [Gillette and Passi, 1988], with the fluid threshold (under the current limited supply condition), $u_{*,\mathrm{ft}} = 0.10\ ms^{-1}$ for 10 μm grains.

$$F_{\mathrm{d}} = C_{\mathrm{em}} u_*^4 \left(1 - \frac{u_{*,\mathrm{ft}}}{u_*}\right) \tag{6.11}$$

where $C_{\mathrm{em}} = 1565\ [\mu g\ m^{-6} s^3]$ is the emission proportionality constant which will depend on the initial concentration of dust available for emission. We further also tried other expressions as suggested by [Kok et al., 2012] in their Eqns.(4.13,4.15) inspired by prior literature [Shao et al., 1993, Gillett and Morales, 1979, Kawamura, 1951, Marticorena and Bergametti, 1995, Zender et al., 2003].

$$F_{\mathrm{d}} = C_{\mathrm{F}} \rho_{\mathrm{a}} u_{*,\mathrm{ft}} \left(u_*^2 - u_{*,\mathrm{ft}}^2\right) \tag{6.12a}$$

$$F_{\mathrm{d}} = C_{\mathrm{K}} \frac{\rho_{\mathrm{a}}}{g} u_*^3 \left(1 - \frac{u_{*,\mathrm{ft}}^2}{u_*^2}\right) \left(1 + \frac{u_{*,\mathrm{ft}}}{u_*}\right) \tag{6.12b}$$

However, as can be seen from Fig. (6.6) these fits are not great, as compared to the fitted curve in Eqn. (6.11). [Lu and Shao, 1999] suggested a similar law with u_*^4 for erodible soils, while u_*^3 for less erodible soils. In the limiting case of dust availability, the dominating mechanism being direct entrainment we can conclude that the scaling law in Eqn. (6.11) captures the emission trend reasonably well.

Viscous sublayer

The nature of turbulent fluctuations inside the laminar layer which was previously described in Eqn. (5.21a), and it's role in the emission process is inspected. It is already conveyed many times before in the thesis, the indispensable part of describing the both the viscous layer and the turbulent characteristics in it when studying the transport close to threshold conditions. We thus simulate a special case where we switch off the turbulent fluctuations inside the viscous layer to observe any difference. In Fig. (6.6) this is conveyed by the green points, significantly lowered for lower wind speeds as the thickness of the layer is atleast $> 1\ d_{200}$. However, it is not differing much for higher wind speeds, albeit with slightly larger values.

6.2.2 Dust burial

This brings us to the investigation, where the vertical flux progression is compared with the horizontal flux (q_{200}) of the saltating sand grains, as well as the center of mass position in the vertical direction of the dust grains ($cm_{z,d_{10}}$) still part of the bed configuration. Fig. (6.7a) gives an insight into the role of saltation on the seepage of dust into the layers below, rarely noticed in observations of the past. However, [Louge et al., 2010] notices the dust entrapment beneath the surface of barchan dunes, only mobilized later with high wind conditions. The final state in the simulation is visualized in Fig. (6.7b), noting the unavailability of further dust sources at the surface. It also raises concerns regarding the conventional emission parametrizations, and if indeed this is observed for large polydisperse sand-dust beds. This is treated as a future scope, and is worth investigating. This would mean in such a case scenario that, the overall dust budget could be fractionally reduced that could have large implications.

6.3 Cohesion induced mechanism

6.3.1 Saltation bombardment

It has been shown through numerous theoretical studies starting with [Shao et al., 1993] on saltation bombardment being the major dynamics for the emission process especially for dusty surfaces. Although Fig. (5.16) shows the effect of cohesion increasing for $d_{\mathrm{m}} < 100\ \mu m$, it was not clear what is the emission regime due to aerodynamic entrainment, and when does it

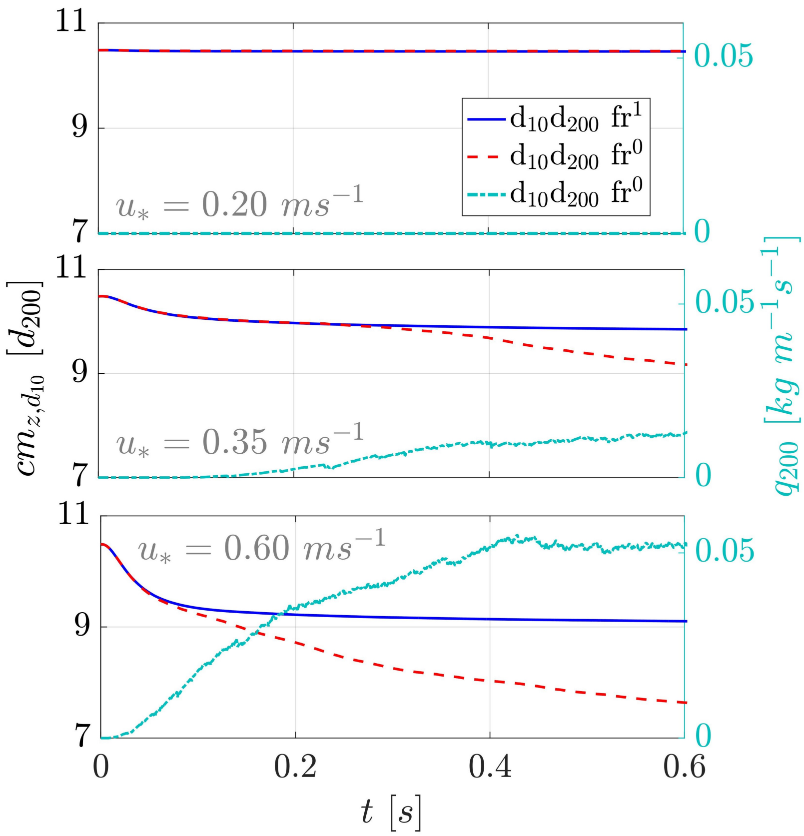

(a) Dust is not just blown away, but a fraction of it seeps into the sandy layer below. This image clearly shows the role of sand bombardment as the q_{200} flux corresponds to the lowering of the center of mass of the d_{10} grains.

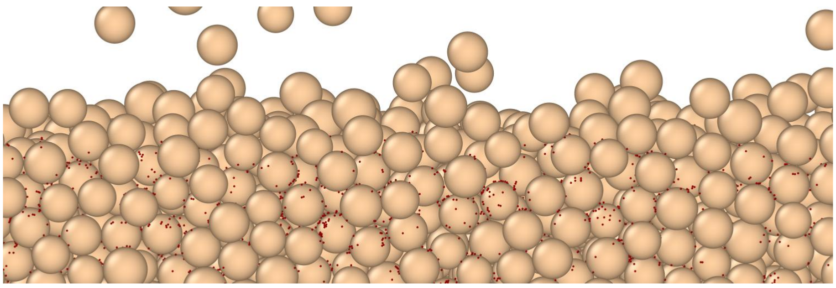

(b) Dust seepage shown in the DEM simulation for $d_{10}d_{200}, u_* = 0.60\ m/s$ at the final state.

Figure 6.7: Dust is buried due to the vibrations-induced by saltating sand grains

transition into that caused by saltation bombardment. Therefore, we set up new experiments albeit the much larger computational effort for smaller grains. To this end, we make realistic assumptions that a 100 μm grain would behave similarly to that of a 200 μm grain (similar threshold behavior in Fig. (5.16)). Also, the effect of cohesion between the dust grains and either d_{200} or d_{100} would be of the same order, thus not disrupting the cluster properties. The dimensions of the domain now are $(L_x \times L_y)/d_{100} = (100 \times 8)$, with again $N = 50k$ grains initially settled over the sand bed.

This figure can be further broken down into what is plotted in Figs. (6.9 - 6.11), the cases $d_{10}d_{100}, d_5d_{100}$ and $d_{2.5}d_{100}$ respectively. We assess the role of saltation, entrainment and the cluster disintegration in more detail, by plotting along with F_{d}, the number of grains emitted as distinct single grains, that which are coated on the d_{100} grains, and those which are present as pure dust clusters.

In Fig. (6.9a), that is for 10 μm grains at $u_* = 0.30\ ms^{-1}$, we as well observe two peaks similar to 5 μm simulations, which the bottom plot suggests about the cluster make-up. The 10 μm grains seem to entrain initially (first peak) and subsequently exhibiting an increase in emission again due to the saltation (flux in grey), and also due to the disintegration of the clusters as the simulation progresses. This is however not observed for 10 μm grains at $u_* = 0.60\ ms^{-1}$ (Fig. (6.9b)) due to the initial burst of entrainment, which keeps the breakage of sand-dust as well as dust-dust clusters to a bare minimum.

On the contrary, in Fig. (6.10a) for 5 μm at $u_* = 0.30\ ms^{-1}$ the first peak is delayed until the onset of saltation, which enhances the emission. Here, we also observe from $t \approx 0.2 - 0.4\ s$ the ejected grains are predominantly present in the coated clusters, and for $t > 0.5\ s$ the disintegration of the clusters commences, thus we see the propagation of the vertical flux over time. Also, see the presence of dust-dust clusters which are present, albeit the limited supply of dust initially. In Fig. (6.10b), at $u_* = 0.60\ ms^{-1}$ still exhibits a predominant secondary peak, which confirms the dominant

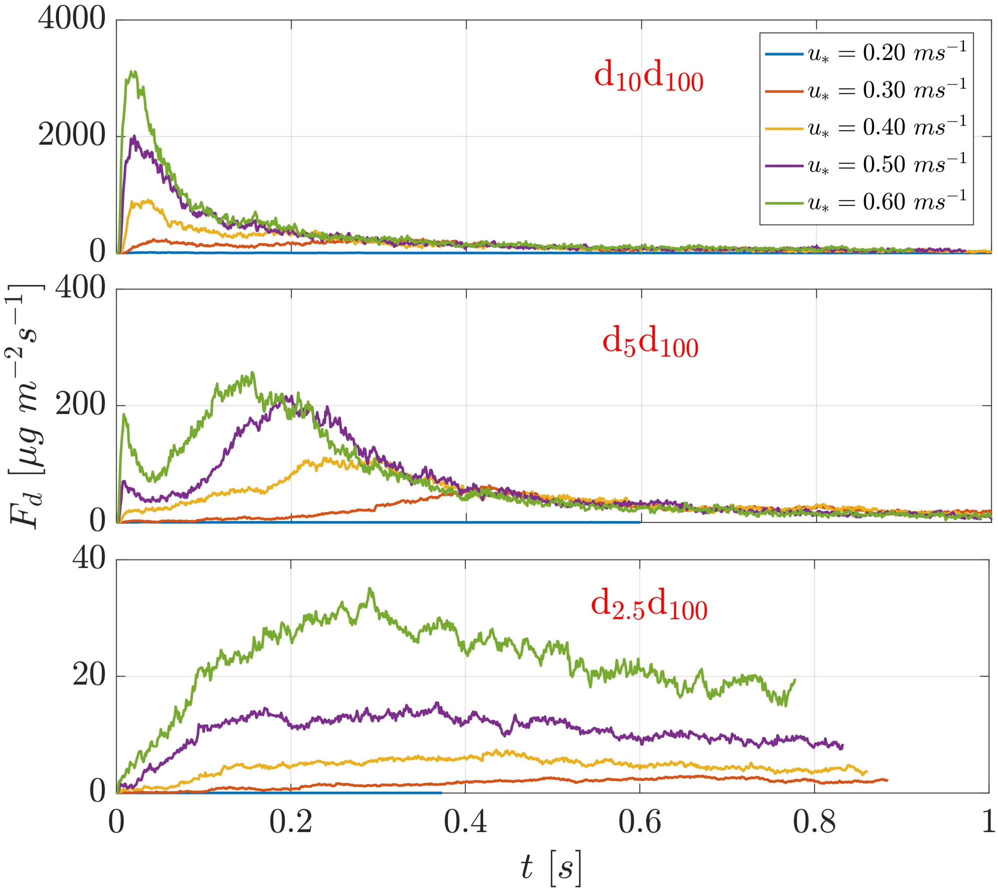

Figure 6.8: The vertical flux evolution for $d_{10}d_{100}, d_5d_{100}\&d_{2.5}d_{100}$. The main difference is in the lag/delay in reaching peak emission, and the observance of a secondary peak for the case of d_5d_{100}. The first attributed to direct entrainment, while the secondary dominant peak refers to the emission due to saltaion.

mechanism to be the emission due to saltation bombardment.

Finally in both Fig. (6.11a) and Fig. (6.11b), for 2.5 μm grains at $u_* = 0.30\ ms^{-1}$ and $u_* = 0.60\ ms^{-1}$ respectively, we see this effect getting amplified with less grains ejected individually, and most of them contained in the clusters acting as a constraint for continuous emission.

We could then state the regime for emission mechanisms for bi-disperse systems, under supply limited conditions as follows. The aerodynamic entrainment is still the major mechanism for $>=$ PM_{10} grains, while the major mechanisms for $<$ PM_{10} grains is the saltation bombardment aided by the cluster disintegrations. Although this provides a fresh perspective, what essentially lies in the scope of future work is to understand the same for larger systems, and also with polydispersity.

6.3.2 Cluster distribution

The cluster properties previously showcased in Fig. (6.9a - 6.11b) can be statistically organized to compare the proportion of grains present either as a single/cluster state throughout the simulations. This is achieved by defining a *Cluster fraction index* ($\Psi_{\mathrm{s,sdc,dc}}$) representing the fractions present individually, as dust-coated-on-sand clusters, and as dust-dust clusters.

$$\Psi_k = \frac{\int_0^\infty N_{\mathrm{dust,k}} dt}{\int_0^\infty \sum_{k=s,sdc,dc} N_{\mathrm{dust,k}} dt} \tag{6.13}$$

[Bullard et al., 2004] suggested the occurrence of $<$ PM_{20} grains mostly as coatings on sand grains, or as dust aggregates [Alfaro et al., 1997, Shao, 2001, 2008]. The low number of individual dust aggregates in our simulations is mainly due to the lower concentrations of dust that is initially available, but we still observe dimers and trimers at the early stage of emission. The larger supply of dust would definitely increase them, and can be explored as a future scope.

Fig. (6.12a) shows the distribution of cluster sizes, for $d_{10}d_{100}, d_5d_{100}, d_{2.5}d_{100}$ systems. The emission in $d_{10}d_{100}$ is dominated by single grains, however

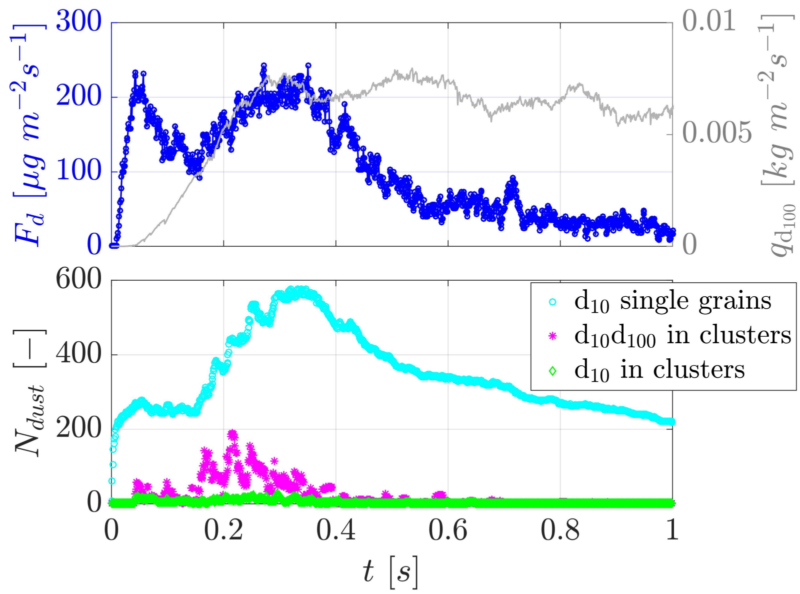

(a) Case $d_{10}d_{100}$ for $u_* = 0.30\ ms^{-1}$

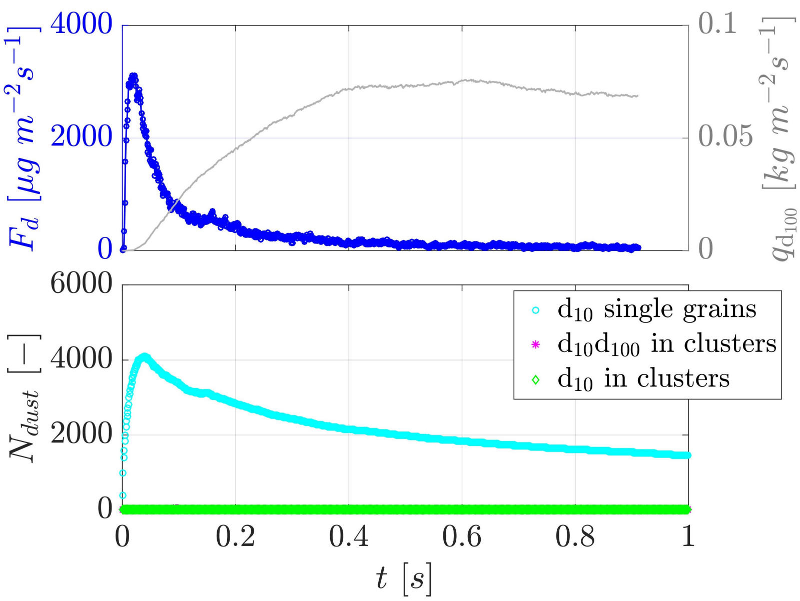

(b) Case $d_{10}d_{100}$ for $u_* = 0.60\ ms^{-1}$

Figure 6.9: Cluster properties for $d_{10}d_{100}$

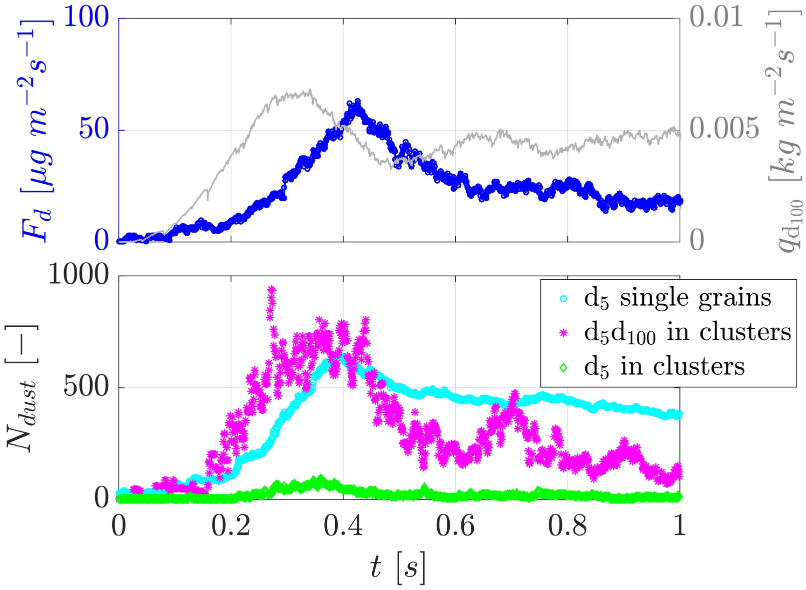

(a) Case d_5d_{100} for $u_* = 0.30\ ms^{-1}$

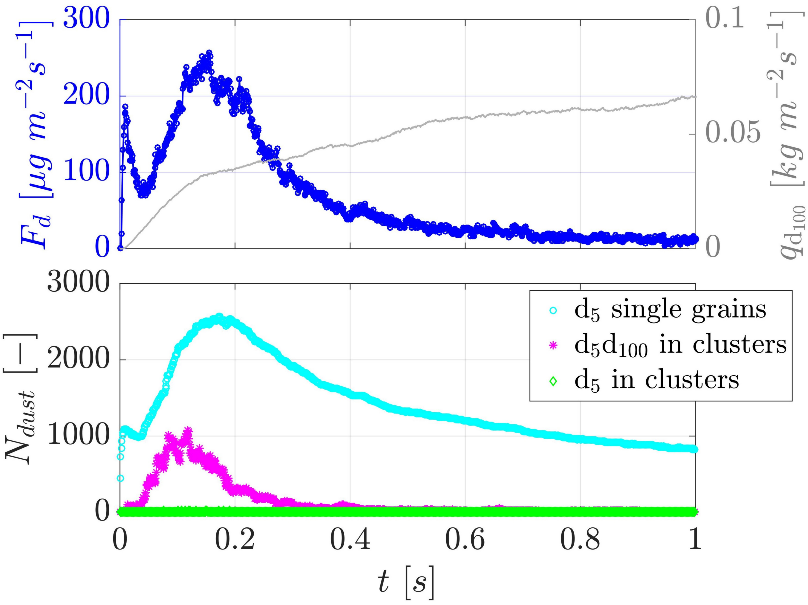

(b) Case d_5d_{100} for $u_* = 0.60\ ms^{-1}$

Figure 6.10: Cluster properties for d_5d_{100}

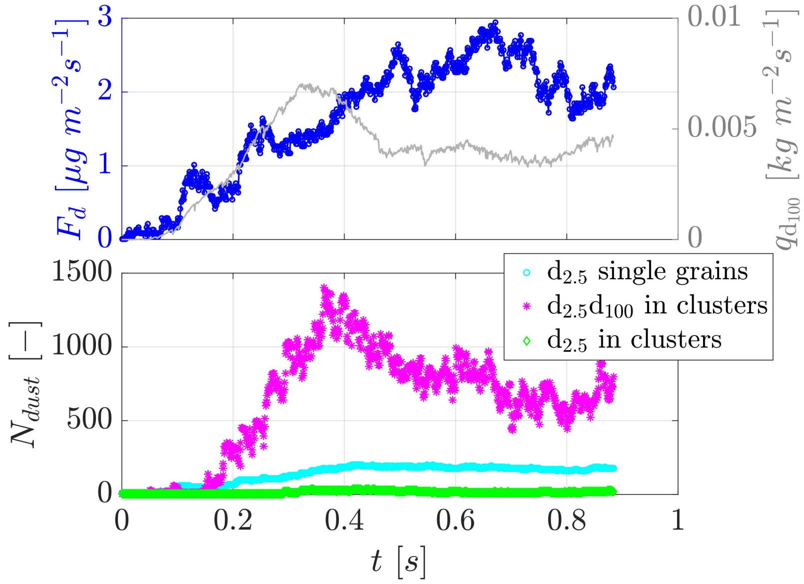

(a) Case $d_{2.5}d_{100}$ for $u_* = 0.30\ ms^{-1}$

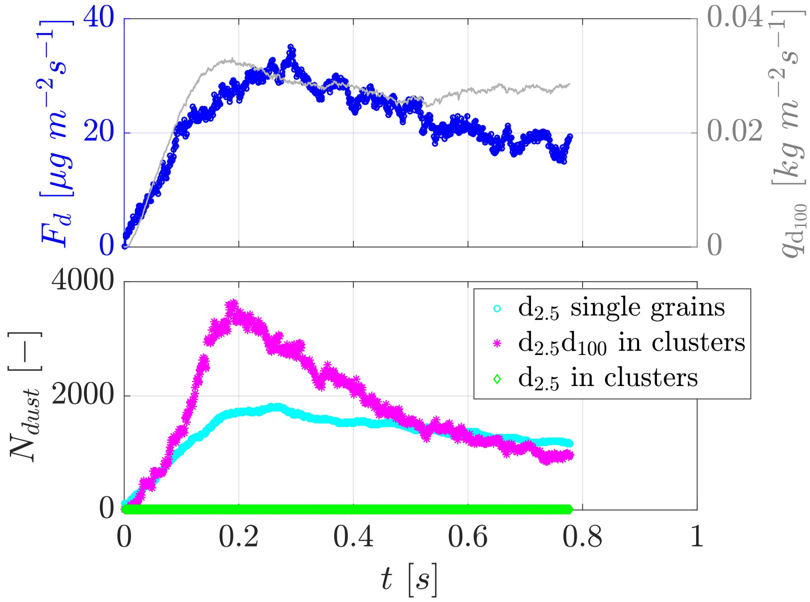

(b) Case $d_{2.5}d_{100}$ for $u_* = 0.60\ ms^{-1}$

Figure 6.11: Cluster properties for $d_{2.5}d_{100}$

we note a small fraction of it in the aggregates for lower wind speed ($u_* = 0.30\ ms^{-1}$). The cluster indexes for $\Psi_{\mathrm{sdc}}, \Psi_{\mathrm{dc}}$ increases significantly for 5 μm and 2.5 μm grains, which is the reason for the delayed emission peaks in Fig. (6.8) as the dust is trapped in the clusters.

In Fig. (6.12b) we plot the difference between $\Psi_{\mathrm{s}} - (\Psi_{\mathrm{sdc}} + \Psi_{\mathrm{dc}})$, a value of 1 indicating 100% emission as distinct grains, while -1 would suggest their presence in clusters.

Thus, in this chapter we conclude that the role of aerodynamic entrainment, is enhanced by turbulent fluctuations and roughness elements. However direct entrainment was harder for grains $<$ 10 μm, and dust was mostly ejected as coated to larger grains or as individual clusters. Most importantly, the scaling of F_{d} with u_* was found to be a quartic relation ($F_{\mathrm{d}} \propto u_*^4$). This would need further analysis to observe the same for larger polydisperse systems, as well including the stochastic cohesion talked about in Chapter (5).

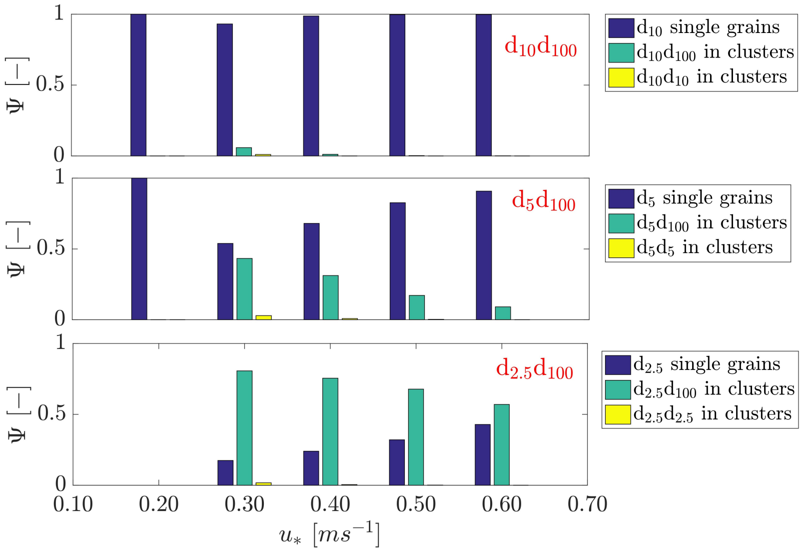

(a) Ψ as a function of u_*, it is more evident that the majority of grains are ejected as clusters for $d \leq 5\ \mu m$

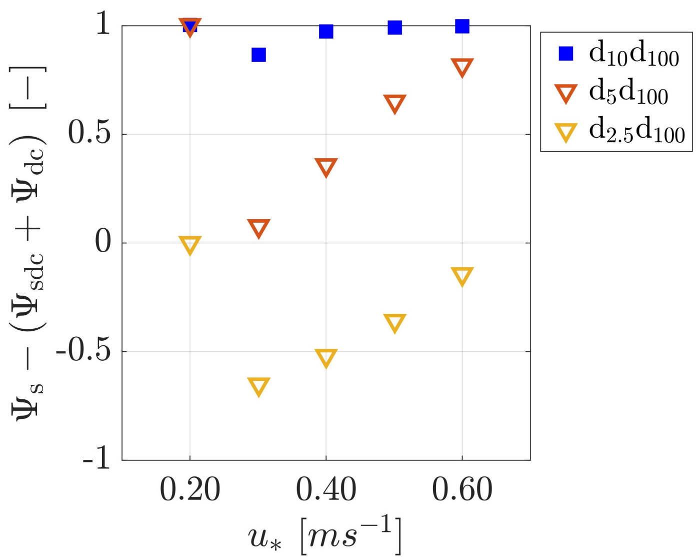

(b) Index difference which portrays the dominant state of the dust grains as single or in clusters.

Figure 6.12: Statistical representation of the cluster fraction index (Ψ) for the various bi-disperse particle systems

Chapter 7

Outlook and future scopes

We presented a robust numerical software to simulate large-scale process of sand saltation and dust emission. In Chapter (1), we introduced the need for such models, as dust is considered to be the one resulting in largest uncertainties in climate models. The various effects of wind-blown sand and dust on the planet's ecosystems and the feedback mechanisms between various components of the Earth's climate systems were discussed. In Chapter (2), we introduced the physics of aeolian erosion and the fluid dynamics aspects sourced from existing models and literature [Kok et al., 2012, Durán et al., 2012, Carneiro et al., 2015] that went into the model. The numerical framework with the DEM model was presented in Chapter (3), along with the parametrizations to validate the model for sand mass flux (Q) relations with u_*. We confirmed the existence of a quadratic scaling of Q with u_* or a linear relation with Θ, the Shields number.

This also allowed us in Chapter 4 to provide scaling laws for a special case of low-sediment availability where we observed a scaling transition from quadratic in erodible conditions to a cubic relation over rigid surfaces [Ho et al., 2011].

In Chapter (5), dust was modeled by adding new modules for describing cohesion, turbulent fluctuations and rolling resistance. We found the relations for the threshold velocities, compared with experiments and previous studies [Shao and Lu, 2000] to be increasing for fine grains. This means the difficulty in entraining grains directly from the bed source, although the stochastic description of cohesion allowed for lowering this threshold. Finally the questions regarding the emission mechanisms of dust were delved into in Chapter 7, where we observed that for PM_{10} grains, direct entrainment was possible for supply-limited conditions even without the onset of saltation. We further found that the vertical dust flux F_{d} scales with u_*^4. with implications to include in future climate models. The aspects relating the cluster distributions to the grain size, we concluded that for grains larger than 10 μm, dust was mostly emitted as individual grains. For grains smaller than 5 μm, dust was mostly coated on the sand grains and was only ejected after consistent bombardment on the surface due to saltation long suspected by [Shao et al., 1993].

As for future research scopes with this software, aspects of particle shape could be incorporated which could have implications on the sand transport phenomena [Jensen et al., 2001, Parteli and Pöschel, 2016]. We considered spherical grains for simplification, but with advancement in computational algorithms this could be easily realized.

The effect of electrostatic forces was not considered, but recent theories and experiments [Krupp, 1967, Kok and Lacks, 2009] have attracted attention to study this in detail. The charged grains which are on the surface, produce a long-range electric field which could either enhance or inhibit entrainment and saltation. The triboelectrification is a relatively new topic of research, is the process by which materials become electrically charged through frictional contact, significantly impacting the dynamics of aeolian sediment transport. When grains collide or slide against each other, they can transfer electrons, leading to the accumulation of opposite charges on different grains [Lacks and Shinbrot, 2019]. This definitely would be a path worth exploring.

Another important feature is the presence of moisture in sand, the formation of liquid water bridges leads to net attractive forces [Herminghaus*, 2005, Nickling and Neuman, 2009]. This could be important in modeling the natural soils in human habitat, with implications on soil run-off impacting agriculture.

Advances in DEM methods, emphasis to coarse-graining methods [Weinhart et al., 2012], GPU accelerated computing [Gan et al., 2016], and machine-learning integrations [Liu and Wu, 2019] are revolutionizing the scope of our simulation ability.

Appendix A

Extracting bed height from the packing fraction profile

The packing fraction in the bed is computed every iteration, which is essential to have an accurate description of the bed height h_b also defined as h_0 in the main chapters. That is, by definition,

$$\phi\left(z = h_b\right) = \phi_b/2 \tag{A.1}$$

Our numerical set-up consists of horizontal grids of thickness, $z_h = 0.1d_m$, which are uniformly placed inside the bed as well as a few diameters above. To compute the packing fraction, we evaluate the volume held by each grain in these thin slices of thickness z_h. To this end, the first step is to identify the location of the center, top and bottom points of each grain among the grids as can be seen in Fig. (A.1). It is implied that the top and bottom of a grain with center z_i and radius r_i are,

$$z_{ti} = z_i + r_i; \quad z_{bi} = z_i - r_i \tag{A.2}$$

The grid identifier n_z for the centers, top and bottom are the given as,

$$n_{zi} = \lfloor z_i/z_h \rfloor;\ n_{zti} = \lfloor z_{ti}/z_h \rfloor;\ n_{zbi} = \lfloor z_{bi}/z_h \rfloor; \tag{A.3}$$

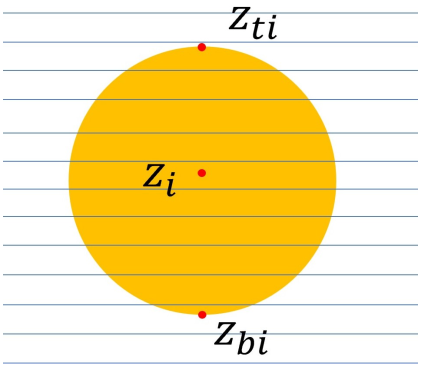

Figure A.1: Identifying the grids in which the particle center z_i, top z_{ti}, and bottom z_{bi} occupy.

For each grain, the volume segments lying in each horizontal slice is calculated as follows, noting the 3 possible configurations as in Fig. (A.2).

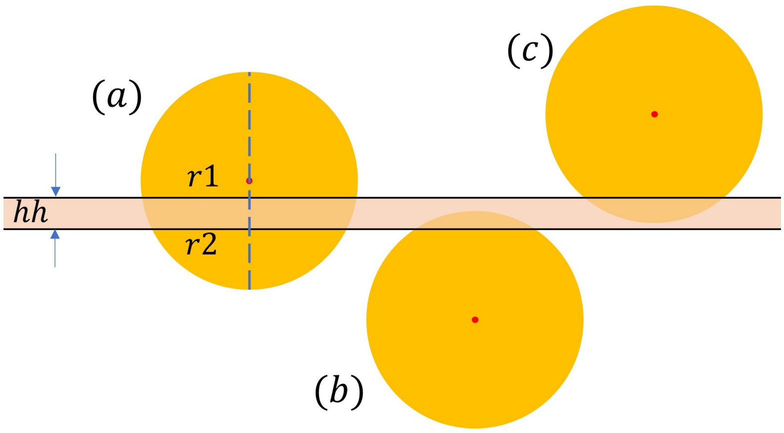

Figure A.2: Possible configurations for the volume slices with varying hh, $r1$ and $r2$.

With this initial identification of the respective locations of the three points in space for each grain, we start the volume computation from n_{zbi} through n_{zi} to n_{zti}. The volume of a spherical segment is,

$$V_i^k = \frac{\pi}{6} hh \left(3\left(r_1^2 + r_2^2\right) + hh^2\right) \tag{A.4}$$

The volume of each segment thus requires the calculation of three parameters hh, r_1 and r_2. As can be seen in Fig. (A.2), the slices represented in (a) would always be $hh = z_h$, whereas r_1, r_2 are derived as a part of a Pythagorean triplet. For example for the slice in (a),

$$r_2 = \sqrt{r_i^2 - (n_{zi} - kz_h)^2} \tag{A.5}$$

$$r_1 = \sqrt{r_i^2 - (n_{zi} - (k+1)z_h)^2} \tag{A.6}$$

for the kth horizontal grid.

On the other hand for the slices in (b) and (c), where the computation is now on what is known as a spherical cap. Note that, the thickness of the cap $hh \leq z_h$ and r_1, r_2 are computed as before. As an example, for the top slice in (b),

$$hh = n_{zti} - kz_h \tag{A.7}$$

Similarly, for the bottom slice in (c),

$$hh = (k+1)\, z_h - n_{zbi} \tag{A.8}$$

The volume in the kth grid is,

$$V^k = \sum_{n=1}^{N} \left(\frac{\pi}{6} hh_n \left(3 \left(r_{1,n}^2 + r_{2,n}^2 \right) + hh_n^2 \right) \right) \tag{A.9}$$

Following this procedure, the packing fraction profile is then obtained for the entire bed with horizontal dimensions l_x, l_y as,

$$\phi^k = \frac{V^k}{l_x l_y z_h} \tag{A.10}$$

For a bed made of non-cohesive grains of size $d_m \approx 200\ \mu m$, this is shown in Fig. (A.3), this computation at the start of each iteration provides the value of the bed height as well as the packing fraction profile very close the bed.

For the numerical methodology in our model, we need not start from the very bottom of the simulation domain, but 5 particle diameters deep below

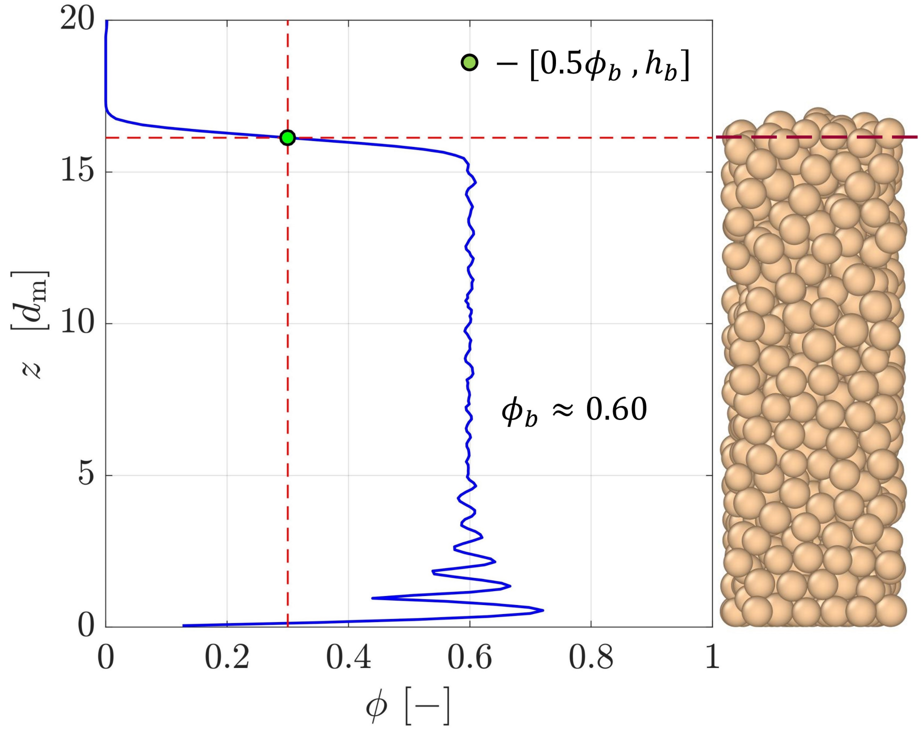

Figure A.3: The packing fraction profile $\phi(z)$ for $d_m = 200\ \mu m$, shows the flat bed effect at the bottom which diminishes for $z > 5d_m$ converging to a value of $\phi = 0.60$ which is a classical behavior of loose granular random packing. The bed height is then interpolated at a point where $phi(h_b) = 0.30$, where the bed height h_b is estimated.

the initial bed height from the visual inspection is sufficient.

Appendix B

Numerical approach by 4th order Runge-Kutta

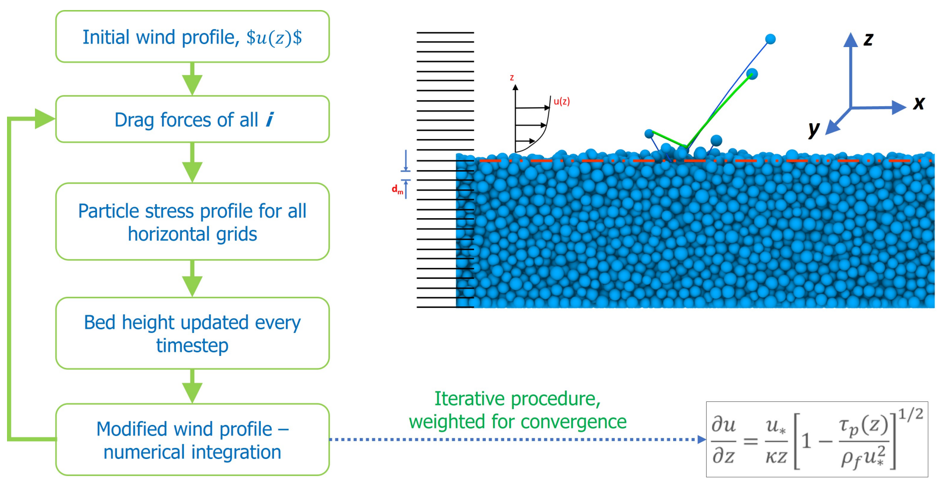

Figure B.1: The general flowchart describing the wind modification arising due to the grain shear stress

As can be seen in Fig. (B.1) it describes the methodology for estimating the wind profile above the bed every iteration. This appendix explains the last step of the numerical integration to compute $u(z)$, which follows from Section (2.4.1), Eqns. (2.36,2.37).

If l_m is the mixing length, u is the wind velocity, $U = \partial u/\partial z$ is a substitution variable, then,

$$
\begin{aligned}
u^{k+1} &= u^k + \frac{1}{6}\left(k_0 + 2(k_1 + k_2) + k_3\right) \\
l_m^{k+1} &= l_m^k + \frac{1}{6}\left(l_0 + 2(l_1 + l_2) + l_3\right) \\
U^{k+1} &= U^k + \frac{1}{6}\left(m_0 + 2(m_1 + m_2) + m_3\right)
\end{aligned}
\tag{B.1}
$$

where $k_{0,1,2,3}, l_{0,1,2,3}, m_{0,1,2,3}$ are the 4th order Runge-Kutta parameters for the resulting set of first-order differential equations.

Bibliography

Stéphane C Alfaro, Annie Gaudichet, Laurent Gomes, and Michel Maillé. Modeling the size distribution of a soil aerosol produced by sandblasting. *Journal of Geophysical Research: Atmospheres*, 102(D10):11239–11249, 1997.

Murilo P Almeida, Eric JR Parteli, José S Andrade Jr, and Hans J Herrmann. Giant saltation on mars. *Proceedings of the National Academy of Sciences*, 105(17):6222–6226, 2008.

Raz Amir, Shai Kinast, Haim Tsoar, Hezi Yizhaq, Eli Zaady, and Yosef Ashkenazy. The effect of wind and precipitation on vegetation and biogenic crust covers in the sde-hallamish sand dunes. *Journal of Geophysical Research: Earth Surface*, 119(3):437–450, 2014.

R. S. Anderson and P. K. Haff. Simulation of grain-transport dynamics on dunes. *Science*, 241(4870):820–823, 1988. doi: 10.1126/science.241.4870.820.

R S Anderson and PK Haff. Wind modification and bed response during saltation of sand in air. In *Aeolian Grain Transport 1: Mechanics*, pages 21–51. Springer, 1991.

Bruno Andreotti. A two-species model of aeolian sand transport. *Journal of Fluid Mechanics*, 510:47–70, 2004.

R. A. Bagnold. *The Physics of Blown Sand and Desert Dunes*. Methuen, New York, 1941.

Ralph A Bagnold. The transport of sand by wind. *The Geographical Journal*, 89(5):409–438, 1937.

SE Bauer, MI Mishchenko, AA Lacis, S Zhang, Ja Perlwitz, and SM Metzger. Do sulfate and nitrate coatings on mineral dust have important effects on radiative properties and climate modeling? *Journal of Geophysical Research: Atmospheres*, 112(D6), 2007.

Djaoued Beladjine, Madani Ammi, Luc Oger, and Alexandre Valance. Collision process between an incident bead and a three-dimensional granular packing. *Physical Review E—Statistical, Nonlinear, and Soft Matter Physics*, 75(6):061305, 2007.

John Desmond Bernal and J_ Mason. Packing of spheres: co-ordination of randomly packed spheres. *Nature*, 188(4754):910–911, 1960.

Nikolai V Brilliantov, Frank Spahn, Jan-Martin Hertzsch, and Thorsten Pöschel. Model for collisions in granular gases. *Physical review E*, 53 (5):5382, 1996.

Joanna E Bullard, Grant H McTainsh, and Christa Pudmenzky. Aeolian abrasion and modes of fine particle production from natural red dune sands: an experimental study. *Sedimentology*, 51(5):1103–1125, 2004.

Joanna E Bullard, Matthew Baddock, Tom Bradwell, John Crusius, Eleanor Darlington, Diego Gaiero, Santiago Gassó, Gudrun Gisladottir, Richard Hodgkins, Robert McCulloch, et al. High-latitude dust in the earth system. *Reviews of Geophysics*, 54(2):447–485, 2016.

Marcus V Carneiro, Nuno AM Araújo, Thomas Pähtz, and Hans J Herrmann. Midair collisions enhance saltation. *Physical review letters*, 111(5):058001, 2013.

Marcus V Carneiro, Keld R Rasmussen, and Hans J Herrmann. Bursts in discontinuous aeolian saltation. *Scientific Reports*, 5(1):11109, 2015.

MV Carneiro, T Pähtz, and HJ Herrmann. Jump at the onset of saltation. *Physical Review Letters*, 107(9):098001, 2011.

Hui Chen, YL Liu, XQ Zhao, YG Xiao, and Y Liu. Numerical investigation on angle of repose and force network from granular pile in variable gravitational environments. *Powder technology*, 283:607–617, 2015.

Nian-Sheng Cheng. Simplified settling velocity formula for sediment particle. *Journal of hydraulic engineering*, 123(2):149–152, 1997.

Nian-Sheng Cheng and Yee-Meng Chiew. Modified logarithmic law for velocity distribution subjected to upward seepage. *Journal of Hydraulic Engineering*, 124(12):1235–1241, 1998.

Filippo Chiodi, Philippe Claudin, and Bruno Andreotti. A two-phase flow model of sediment transport: transition from bedload to suspended load. *Journal of Fluid Mechanics*, 755:561–581, 2014.

OG Chkhetiani, EB Gledzer, MS Artamonova, and MA Iordanskii. Dust resuspension under weak wind conditions: direct observations and model. *Atmospheric Chemistry and Physics*, 12(11):5147–5162, 2012.

Francesco Comola, Johan Gaume, JF Kok, and M Lehning. Cohesion-induced enhancement of aeolian saltation. *Geophysical Research Letters*, 46(10):5566–5574, 2019.

Francesco Comola, Jasper F Kok, Juan M Lora, Kaylie Cohanim, Xinting Yu, Chao He, Patricia McGuiggan, Sarah M Hörst, and Francis Turney. Titan's prevailing circulation might drive highly intermittent, yet significant sediment transport. *Geophysical Research Letters*, 49(7):e2022GL097913, 2022.

Mathieu Creyssels, Pascal Dupont, A Ould El Moctar, Alexandre Valance, Isabelle Cantat, James Thomas Jenkins, José Miguel Pasini, and Keld Rømer Rasmussen. Saltating particles in a turbulent boundary layer: experiment and theory. *Journal of Fluid Mechanics*, 625:47–74, 2009.

P. A. Cundall and O. D. L. Strack. A discrete element method model for granular assemblies. *Geotechnique*, 29(1):47–65, 1979. doi: 10.1680/geot.1979.29.1.47.

S De Vries, JSM van Thiel de Vries, LC Van Rijn, SM Arens, and RWM-RJB Ranasinghe. Aeolian sediment transport in supply limited situations. *Aeolian Research*, 12:75–85, 2014.

Alberto Di Renzo and Francesco Paolo Di Maio. Comparison of contact-force models for the simulation of collisions in dem-based granular flow codes. *Chemical engineering science*, 59(3):525–541, 2004.

Heqiang Du, Xinlei Liu, Ruiqiang Ding, Yawei Fan, and Xiufan Liu. New insights into dust emission mechanism in natural environments based on a series of field observations. *Science of The Total Environment*, 914:169888, 2024.

Jason P Dunion and Christopher S Velden. The impact of the saharan air layer on atlantic tropical cyclone activity. *Bulletin of the American Meteorological Society*, 85(3):353–366, 2004.

Orencio Durán, Eric JR Parteli, and Hans J Herrmann. A continuous model for sand dunes: Review, new developments and application to barchan dunes and barchan dune fields. *Earth Surface Processes and Landforms*, 35(13):1591–1600, 2010.

Orencio Durán, Philippe Claudin, and Bruno Andreotti. On aeolian transport: Grain-scale interactions, dynamical mechanisms and scaling laws. *Aeolian Research*, 3(3):243–270, 2011.

Orencio Durán, Bruno Andreotti, and Philippe Claudin. Numerical simulation of turbulent sediment transport, from bed load to saltation. *Physics of Fluids*, 24(10), 2012.

Orencio Durán, Philippe Claudin, and Bruno Andreotti. Direct numerical simulations of aeolian sand ripples. *Proceedings of the National Academy of Sciences*, 111(44):15665–15668, 2014.

Igor Ekhiel'evich Dzyaloshinskii, Efrat M Lifshitz, and Lev P Pitaevskii. The general theory of van der waals forces. *Advances in Physics*, 10(38): 165–209, 1961.

Paolo D'Odorico, Abinash Bhattachan, Kyle F Davis, Sujith Ravi, and Christiane W Runyan. Global desertification: Drivers and feedbacks. *Advances in water resources*, 51:326–344, 2013.

Hans Albert Einstein and El-Sayed Ahmed El-Samni. Hydrodynamic forces on a rough wall. *Reviews of modern physics*, 21(3):520, 1949.

Filip Elekes and Eric JR Parteli. An expression for the angle of repose of dry cohesive granular materials on earth and in planetary environments. *Proceedings of the National Academy of Sciences*, 118(38):e2107965118, 2021.

Burak Adnan Erkorkmaz, Daniella Gat, and Yinon Rudich. Aerial transport of bacteria by dust plumes in the eastern mediterranean revealed by complementary rrna/rrna-gene sequencing. *Communications earth & environment*, 4(1):24, 2023.

Fengxian Fan, Eric JR Parteli, and Thorsten Pöschel. Origin of granular capillarity revealed by particle-based simulations. *Physical Review Letters*, 118(21):218001, 2017.

RI Ferguson and M Church. A simple universal equation for grain settling velocity. *Journal of sedimentary Research*, 74(6):933–937, 2004.

B Fletcher. The incipient motion of granular materials. *Journal of Physics D: Applied Physics*, 9(17):2471, 1976.

Steven G Fryberger, ABDULKADER M AL-SARI, Thomas J Clisham, Syed AR Rizvi, and KHATTAB G AL-HINAI. Wind sedimentation in the jafurah sand sea, saudi arabia. *Sedimentology*, 31(3):413–431, 1984.

JQ Gan, ZY Zhou, and AB Yu. A gpu-based dem approach for modelling of particulate systems. *Powder Technology*, 301:1172–1182, 2016.

Derek Geldart, EC Abdullah, A Hassanpour, LC Nwoke, and IJCP Wouters. Characterization of powder flowability using measurement of angle of repose. *China Particuology*, 4(3-4):104–107, 2006.

D Gillett and C Morales. Environmental factors affecting dust emission by wind erosion. *Saharan dust*, pages 71–94, 1979.

Dale A Gillette. On the production of soil wind erosion aerosols having the potential for long range transport. 1974.

Dale A Gillette and Ranjit Passi. Modeling dust emission caused by wind erosion. *Journal of Geophysical Research: Atmospheres*, 93(D11):14233–14242, 1988.

Dale A Gillette and Theodore R Walker. Characteristics of airborne particles produced by wind erosion of sandy soil, high plains of west texas. *Soil Science*, 123(2):97–110, 1977.

Martin Götzinger and Wolfgang Peukert. Dispersive forces of particle–surface interactions: direct afm measurements and modelling. *Powder Technology*, 130(1-3):102–109, 2003.

Andrew S Goudie. Dust storms: Recent developments. *Journal of environmental management*, 90(1):89–94, 2009.

Ronald Greeley and James D Iversen. *Wind as a geological process: on Earth, Mars, Venus and Titan*. Number 4. CUP Archive, 1987.

Dale W Griffin. Atmospheric movement of microorganisms in clouds of desert dust and implications for human health. *Clinical microbiology reviews*, 20 (3):459–477, 2007.

Hugo C Hamaker. The london—van der waals attraction between spherical particles. *physica*, 4(10):1058–1072, 1937.

Vahid Hassanzadeh, Chris M Wensrich, and Roberto Moreno-Atanasio. Elucidation of the role of cohesion in the macroscopic behaviour of coarse particulate systems using dem. *Powder technology*, 361:374–388, 2020.

Yi He, Ali Hassanpour, Mohammadreza Alizadeh Behjani, and Andrew E Bayly. A novel stiffness scaling methodology for discrete element modelling of cohesive fine powders. *Applied Mathematical Modelling*, 90:817–844, 2021.

Stephan Herminghaus*. Dynamics of wet granular matter. *Advances in physics*, 54(3):221–261, 2005.

Tuan Duc Ho, Alexandre Valance, Pascal Dupont, and A Ould El Moctar. Scaling laws in aeolian sand transport. *Physical Review Letters*, 106(9): 094501, 2011.

Bas M Hoonhout and Sierd de Vries. A process-based model for aeolian sediment transport and spatiotemporal varying sediment availability. *Journal of Geophysical Research: Earth Surface*, 121(8):1555–1575, 2016.

JCR Hunt and AH Weber. A lagrangian statistical analysis of diffusion from a ground-level source in a turbulent boundary layer. *Quarterly Journal of the Royal Meteorological Society*, 105(444):423–443, 1979.

IPCC. Third assessment report (tar) of the intergovernmental panel on climate change. Technical report, Intergovernmental Panel on Climate Change, Geneva, 2001. URL `https://www.ipcc.ch/report/ar3/`. Contributions from Working Groups I, II, and III.

IPCC. Climate change 2021: The physical science basis. Technical report, Intergovernmental Panel on Climate Change, Cambridge, 2021. URL `https://doi.org/10.1017/9781009157896`. Contribution of Working Group I to the Sixth Assessment Report.

J. Israelachvili. *Intermolecular & Surface Forces*. Academic Press, London, 1998.

JD Iversen, James B Pollack, Ronald Greeley, and Bruce R White. Saltation threshold on mars: The effect of interparticle force, surface roughness, and low atmospheric density. *Icarus*, 29(3):381–393, 1976.

Richard P Jensen, Tuncer B Edil, Peter J Bosscher, Michael E Plesha, and Nabil Ben Kahla. Effect of particle shape on interface behavior of dem-simulated granular materials. *International Journal of Geomechanics*, 1 (1):1–19, 2001.

Shibu Jose. *Agroforestry for ecosystem services and environmental benefits: an overview*. Springer, 2009.

Sandesh Kamath and Eric Parteli. Toward a large-scale particle-based parallel simulator of aeolian sand transport, including a model for mobile sand availability. In *EPJ Web of Conferences*, volume 249, page 13004. EDP Sciences, 2021.

Sandesh Kamath, Yaping Shao, and Eric JR Parteli. Scaling laws in aeolian sand transport under low sand availability. *Geophysical Research Letters*, 49(11):e2022GL097767, 2022.

Ryuma Kawamura. Study on sand movement by wind. *Report*, 5(3):95–112, 1951.

JF Kjelgaard, DG Chandler, and KE Saxton. Evidence for direct suspension of loessial soils on the columbia plateau. *Earth Surface Processes and Landforms*, 29(2):221–236, 2004.

François Kneib, Frédéric Dufour, and Mohamed Naaim. Forces experienced by the walls of a granular lid-driven cavity. In *CFM 2015-22ème Congrès Français de Mécanique*. AFM, Maison de la Mécanique, 39/41 rue Louis Blanc-92400 Courbevoie, 2015.

Jasper F Kok and Daniel J Lacks. Electrification of granular systems of identical insulators. *Physical Review E—Statistical, Nonlinear, and Soft Matter Physics*, 79(5):051304, 2009.

Jasper F Kok and Nilton O Renno. A comprehensive numerical model of steady state saltation (comsalt). *Journal of Geophysical Research: Atmospheres*, 114(D17), 2009.

Jasper F Kok, Eric JR Parteli, Timothy I Michaels, and Diana Bou Karam. The physics of wind-blown sand and dust. *Reports on progress in Physics*, 75(10):106901, 2012.

Jasper F Kok, Daniel S Ward, Natalie M Mahowald, and Amato T Evan. Global and regional importance of the direct dust-climate feedback. *Nature communications*, 9(1):241, 2018.

Jasper F Kok, Trude Storelvmo, Vlassis A Karydis, Adeyemi A Adebiyi, Natalie M Mahowald, Amato T Evan, Cenlin He, and Danny M Leung. Mineral dust aerosol impacts on global climate and climate change. *Nature Reviews Earth & Environment*, 4(2):71–86, 2023.

Andrey Nikolaevich Kolmogorov. The local structure of turbulence in incompressible viscous fluid for very large reynolds. *Numbers. In Dokl. Akad. Nauk SSSR*, 30:301, 1941.

Klaus Kroy, Gerd Sauermann, and Hans J Herrmann. Minimal model for aeolian sand dunes. *Physical Review E*, 66(3):031302, 2002.

Harald Kruggel-Emden, Erdem Simsek, Stefan Rickelt, Siegmar Wirtz, and Viktor Scherer. Review and extension of normal force models for the discrete element method. *Powder Technology*, 171(3):157–173, 2007.

Helmar Krupp. Particle adhesion theory and experiment. *Advan. Colloid Interface Sci.*, 1:111–239, 1967.

Daniel J Lacks and Troy Shinbrot. Long-standing and unresolved issues in triboelectric charging. *Nature Reviews Chemistry*, 3(8):465–476, 2019.

Marc Lämmel, Daniel Rings, and Klaus Kroy. A two-species continuum model for aeolian sand transport. *New Journal of Physics*, 14(9):093037, 2012.

Katharina Lettau. Experimental and micrometeorological field studies of dune migration. *Exploring in the World's driest climate*, pages 110–147, 1978.

G Li, J Zhang, HJ Herrmann, Y Shao, and N Huang. Study of aerodynamic grain entrainment in aeolian transport. *Geophysical Research Letters*, 47 (11):e2019GL086574, 2020.

Zeliang Liu and CT Wu. Exploring the 3d architectures of deep material network in data-driven multiscale mechanics. *Journal of the Mechanics and Physics of Solids*, 127:20–46, 2019.

Gwen A Loosmore and James R Hunt. Dust resuspension without saltation. *Journal of Geophysical Research: Atmospheres*, 105(D16):20663–20671, 2000.

Michel Yves Louge, Alexandre Valance, H Mint Babah, J-C Moreau-Trouvé, A Ould el Moctar, Pascal Dupont, and D Ould Ahmedou. Seepage-induced penetration of water vapor and dust beneath ripples and dunes. *Journal of Geophysical Research: Earth Surface*, 115(F2), 2010.

Hua Lu and Yaping Shao. A new model for dust emission by saltation bombardment. *Journal of Geophysical Research: Atmospheres*, 104(D14): 16827–16842, 1999.

Stefan Luding. Collisions & contacts between two particles. In *Physics of dry granular media*, pages 285–304. Springer, 1998.

Stefan Luding. Cohesive, frictional powders: contact models for tension. *Granular matter*, 10(4):235–246, 2008.

Margarida Machado, Pedro Moreira, Paulo Flores, and Hamid M Lankarani. Compliant contact force models in multibody dynamics: Evolution of the hertz contact theory. *Mechanism and machine theory*, 53:99–121, 2012.

Torin Macpherson, William G Nickling, John A Gillies, and Vicken Etyemezian. Dust emissions from undisturbed and disturbed supply-limited desert surfaces. *Journal of Geophysical Research: Earth Surface*, 113(F2), 2008.

Natalie Mahowald, Samuel Albani, Jasper F Kok, Sebastian Engelstaeder, Rachel Scanza, Daniel S Ward, and Mark G Flanner. The size distribution of desert dust aerosols and its impact on the earth system. *Aeolian Research*, 15:53–71, 2014.

Beatrice Marticorena and Gilles Bergametti. Modeling the atmospheric dust cycle: 1. design of a soil-derived dust emission scheme. *Journal of geophysical research: atmospheres*, 100(D8):16415–16430, 1995.

Raleigh L Martin and Jasper F Kok. Wind-invariant saltation heights imply linear scaling of aeolian saltation flux with shear stress. *Science advances*, 3(6):e1602569, 2017.

Nicos S Martys and Raymond D Mountain. Velocity verlet algorithm for dissipative-particle-dynamics-based models of suspensions. *Physical Review E*, 59(3):3733, 1999.

Nicholas J Middleton and Andrew S Goudie. Saharan dust: sources and trajectories. *Transactions of the Institute of British Geographers*, 26(2): 165–181, 2001.

AM Mollinger and FTM Nieuwstadt. Measurement of the lift force on a particle fixed to the wall in the viscous sublayer of a fully developed turbulent boundary layer. *Journal of Fluid Mechanics*, 316:285–306, 1996.

Steven L Namikas. Field measurement and numerical modelling of aeolian mass flux distributions on a sandy beach. *Sedimentology*, 50(2):303–326, 2003.

M Nemoto and K Nishimura. Numerical simulation of snow saltation and suspension in a turbulent boundary layer. *Journal of Geophysical Research: Atmospheres*, 109(D18), 2004.

WG Nickling and JA Gillies. Emission of fine-grained particulates from desert soils. In *Paleoclimatology and Paleometeorology: modern and past patterns of global atmospheric transport*, pages 133–165. Springer, 1989.

WG Nickling and JA Gillies. Dust emission and transport in mali, west africa. *Sedimentology*, 40(5):859–868, 1993.

William G Nickling and Cheryl McKenna Neuman. Aeolian sediment transport. In *Geomorphology of desert environments*, pages 517–555. Springer, 2009.

Johann Nikuradse. Stromungsgesetze in rauhen rohren. *vdi-forschungsheft*, 361:1, 1933.

Vitaliy Ogarko and Stefan Luding. A fast multilevel algorithm for contact detection of arbitrarily polydisperse objects. *Computer physics communications*, 183(4):931–936, 2012.

Luc Oger, Madani Ammi, Alexandre Valance, and Djaoued Beladjine. Study of the collision of one rapid sphere on 3d packings: Experimental and numerical results. *Computers & Mathematics with Applications*, 55(2): 132–148, 2008.

Gregory S Okin, Natalie Mahowald, Oliver A Chadwick, and Paulo Artaxo. Impact of desert dust on the biogeochemistry of phosphorus in terrestrial ecosystems. *Global Biogeochemical Cycles*, 18(2), 2004.

P Rr Owen. Saltation of uniform grains in air. *Journal of Fluid Mechanics*, 20(2):225–242, 1964.

Thomas Pähtz and Orencio Durán. Unification of aeolian and fluvial sediment transport rate from granular physics. *Physical Review Letters*, 124(16): 168001, 2020.

Thomas Pähtz and Orencio Durán. Scaling laws for planetary sediment transport from dem-rans numerical simulations. *Journal of Fluid Mechanics*, 963:A20, 2023.

Thomas Pähtz, Jasper F Kok, and Hans J Herrmann. The apparent roughness of a sand surface blown by wind from an analytical model of saltation. *New Journal of Physics*, 14(4):043035, 2012.

Thomas Pähtz, A Omerad˘, Marcus V Carneiro, NM Ara, and Hans J Herrmann. Which length scale dominates saturation of aeolian sand transport? *Geophys. Res. Lett*, (2), 2014a.

Thomas Pähtz, Eric JR Parteli, Jasper F Kok, and Hans J Herrmann. Analytical model for flux saturation in sediment transport. *Physical Review E*, 89(5):052213, 2014b.

Thomas Pähtz, Amir Omeradžić, Marcus V Carneiro, Nuno AM Araújo, and Hans J Herrmann. Discrete element method simulations of the saturation of aeolian sand transport. *Geophysical Research Letters*, 42(6):2063–2070, 2015.

Thomas Pähtz, Abram H Clark, Manousos Valyrakis, and Orencio Durán. The physics of sediment transport initiation, cessation, and entrainment across aeolian and fluvial environments. *Reviews of Geophysics*, 58(1): e2019RG000679, 2020.

Thomas Pähtz, Yonghui Liu, Yuezhang Xia, Peng Hu, Zhiguo He, and Katharina Tholen. Unified model of sediment transport threshold and rate across weak and intense subaqueous bedload, windblown sand, and windblown snow. *Journal of Geophysical Research: Earth Surface*, 126(4): e2020JF005859, 2021.

Thomas H Painter, S McKenzie Skiles, Jeffrey S Deems, Ann C Bryant, and Christopher C Landry. Dust radiative forcing in snow of the upper colorado river basin: 1. a 6 year record of energy balance, radiation, and dust concentrations. *Water Resources Research*, 48(7), 2012.

Eric J. R. Parteli. Physics and modeling of wind-blown sand landscapes. 2022a.

Eric JR Parteli. Predicted expansion of sand deserts. *nature climate change*, 12(11):967–968, 2022b.

Eric JR Parteli and Thorsten Pöschel. Particle-based simulation of powder application in additive manufacturing. *Powder Technology*, 288:96–102, 2016.

Eric JR Parteli, Orencio Duran, and Hans J Herrmann. Minimal size of a barchan dune. *Physical Review E—Statistical, Nonlinear, and Soft Matter Physics*, 75(1):011301, 2007.

Eric JR Parteli, Klaus Kroy, Haim Tsoar, José S Andrade Jr, and Thorsten Pöschel. Morphodynamic modeling of aeolian dunes: Review and future plans. *The European Physical Journal Special Topics*, 223(11):2269–2283, 2014a.

Eric JR Parteli, Jochen Schmidt, Christina Blümel, Karl-Ernst Wirth, Wolfgang Peukert, and Thorsten Pöschel. Attractive particle interaction forces and packing density of fine glass powders. *Scientific reports*, 4(1):6227, 2014b.

Jorge Pey, Xavier Querol, Andrés Alastuey, F Forastiere, and M Stafoggia. African dust outbreaks over the mediterranean basin during 2001–2011: Pm 10 concentrations, phenomenology and trends, and its relation with synoptic and mesoscale meteorology. *Atmospheric Chemistry and Physics*, 13(3):1395–1410, 2013.

SB Pope and YL Chen. The velocity-dissipation probability density function model for turbulent flows. *Physics of Fluids A: Fluid Dynamics*, 2(8): 1437–1449, 1990.

Thorsten Pöschel and Thomas Schwager. *Computational granular dynamics: models and algorithms*. Springer Science & Business Media, 2005.

Ludwig Prandtl. 7. bericht über untersuchungen zur ausgebildeten turbulenz. *ZAMM-Journal of Applied Mathematics and Mechanics/Zeitschrift für Angewandte Mathematik und Mechanik*, 5(2):136–139, 1925.

Joseph M Prospero, Paul Ginoux, Omar Torres, Sharon E Nicholson, and Thomas E Gill. Environmental characterization of global sources of atmospheric soil dust identified with the nimbus 7 total ozone mapping spectrometer (toms) absorbing aerosol product. *Reviews of geophysics*, 40(1): 2–1, 2002.

JL Ralaiarisoa, Jean-Baptiste Besnard, B Furieri, P Dupont, A Ould El Moctar, F Naaim-Bouvet, and Alexandre Valance. Transition from saltation to collisional regime in windblown sand. *Physical Review Letters*, 124(19): 198501, 2020.

AM Reynolds. Superstatistical mechanics of tracer-particle motions in turbulence. *Physical review letters*, 91(8):084503, 2003.

Lewis F Richardson. *Weather prediction by numerical process*. University Press, 1922.

Leo C van Rijn. Principles of fluid flow and surface waves in rivers, estuaries, seas, and oceans. *(No Title)*, 1990.

Jason A Roney and Bruce R White. Definition and measurement of dust aeolian thresholds. *Journal of Geophysical Research: Earth Surface*, 109 (F1), 2004.

Carl Sagan. Windblown dust on venus. *Journal of Atmospheric Sciences*, 32 (6):1079–1083, 1975.

Andrew Pablo Santos, Dan S Bolintineanu, Gary S Grest, Jeremy B Lechman, Steven J Plimpton, Ishan Srivastava, and Leonardo E Silbert. Granular packings with sliding, rolling, and twisting friction. *Physical Review E*, 102(3):032903, 2020.

Gerd Sauermann, Klaus Kroy, and Hans J Herrmann. Continuum saltation model for sand dunes. *Physical Review E*, 64(3):031305, 2001.

BL Sawford. Reynolds number effects in lagrangian stochastic models of turbulent dispersion. *Physics of Fluids A: Fluid Dynamics*, 3(6):1577–1586, 1991.

Kerstin Schepanski. Transport of mineral dust and its impact on climate. *Geosciences*, 8(5):151, 2018.

D S Schmidt, R A Schmidt, and JD Dent. Electrostatic force on saltating sand. *Journal of Geophysical Research: Atmospheres*, 103(D8):8997–9001, 1998.

Jochen Schmidt, Eric JR Parteli, Norman Uhlmann, Norbert Woerlein, Karl-Ernst Wirth, Thorsten Poeschel, and Wolfgang Peukert. Packings of micron-sized spherical particles–insights from bulk density determination, x-ray microtomography and discrete element simulations. *Advanced Powder Technology*, 31(6):2293–2304, 2020.

J Shäfer, S Dippel, and DE Wolf. Force schemes in simulations of granular materials. *Journal de physique I*, 6(1):5–20, 1996.

Y-P Shao. A lagrangian stochastic model for nonpassive particle diffusion in turbulent flows. *Mathematical and computer modelling*, 21(9):31–37, 1995.

Yaping Shao. A model for mineral dust emission. *Journal of Geophysical Research: Atmospheres*, 106(D17):20239–20254, 2001.

Yaping Shao. *Physics and modelling of wind erosion*. Springer, 2008.

Yaping Shao and Martina Klose. A note on the stochastic nature of particle cohesive force and implications to threshold friction velocity for aerodynamic dust entrainment. *Aeolian Research*, 22:123–125, 2016.

Yaping Shao and An Li. Numerical modelling of saltation in the atmospheric surface layer. *Boundary-Layer Meteorology*, 91:199–225, 1999.

Yaping Shao and Hua Lu. A simple expression for wind erosion threshold friction velocity. *Journal of Geophysical Research: Atmospheres*, 105(D17): 22437–22443, 2000.

Yaping Shao, MR Raupach, and PA Findlater. Effect of saltation bombardment on the entrainment of dust by wind. *Journal of Geophysical Research: Atmospheres*, 98(D7):12719–12726, 1993.

Yaping Shao, Karl-Heinz Wyrwoll, Adrian Chappell, Jianping Huang, Zhaohui Lin, Grant H McTainsh, Masao Mikami, Taichu Y Tanaka, Xulong Wang, and Soonchang Yoon. Dust cycle: An emerging core theme in earth system science. *Aeolian Research*, 2(4):181–204, 2011.

BS Sharratt and DAVID Lauer. Particulate matter concentration and air quality affected by windblown dust in the columbia plateau. *Journal of environmental quality*, 35(6):2011–2016, 2006.

Yaping Shen, Chunlai Zhang, Rende Wang, Xuesong Wang, Songbo Cen, and Qing Li. Spatial heterogeneity of surface sediment grain size and aeolian activity in the gobi desert region of northwest china. *Catena*, 188:104469, 2020.

Tom Shire, Kevin J Hanley, and Kevin Stratford. Dem simulations of polydisperse media: efficient contact detection applied to investigate the quasi-static limit. *Computational Particle Mechanics*, 8(4):653–663, 2021.

Leonardo E Silbert, Deniz Ertaş, Gary S Grest, Thomas C Halsey, Dov Levine, and Steven J Plimpton. Granular flow down an inclined plane: Bagnold scaling and rheology. *Physical Review E*, 64(5):051302, 2001.

Michael Sørensen. On the rate of aeolian sand transport. *Geomorphology*, 59 (1-4):53–62, 2004.

Roland B Stull. *An introduction to boundary layer meteorology*, volume 13. Springer Science & Business Media, 2012.

R Sullivan, D Banfield, James F Bell III, W Calvin, D Fike, M Golombek, Ronald Greeley, J Grotzinger, K Herkenhoff, D Jerolmack, et al. Aeolian processes at the mars exploration rover meridiani planum landing site. *Nature*, 436(7047):58–61, 2005.

Mark R Sweeney and Joseph A Mason. Mechanisms of dust emission from pleistocene loess deposits, nebraska, usa. *Journal of Geophysical Research: Earth Surface*, 118(3):1460–1471, 2013.

Sadatoshi Taneda. Experimental investigation of the wakes behind cylinders and plates at low reynolds numbers. *Journal of the Physical Society of Japan*, 11(3):302–307, 1956.

Matt W Telfer, Eric JR Parteli, Jani Radebaugh, Ross A Beyer, Tanguy Bertrand, François Forget, Francis Nimmo, Will M Grundy, Jeffrey M Moore, S Alan Stern, et al. Dunes on pluto. *Science*, 360(6392):992–997, 2018.

Katharina Tholen, Thomas Pähtz, Sandesh Kamath, Eric JR Parteli, and Klaus Kroy. Anomalous scaling of aeolian sand transport reveals coupling to bed rheology. *Physical Review Letters*, 130(5):058204, 2023.

Aidan P Thompson, H Metin Aktulga, Richard Berger, Dan S Bolintineanu, W Michael Brown, Paul S Crozier, Pieter J In't Veld, Axel Kohlmeyer, Stan G Moore, Trung Dac Nguyen, et al. Lammps-a flexible simulation tool for particle-based materials modeling at the atomic, meso, and continuum scales. *Computer Physics Communications*, 271:108171, 2022.

H Tsoar and K Pye. Dust transport and the question of desert loess formation. *sedimentology*, 34(1):139–153, 1987.

Sean Twomey. The influence of pollution on the shortwave albedo of clouds. *Journal of the atmospheric sciences*, 34(7):1149–1152, 1977.

Gábor Újvári, Jasper F Kok, György Varga, and János Kovács. The physics of wind-blown loess: Implications for grain size proxy interpretations in quaternary paleoclimate studies. *Earth-Science Reviews*, 154:247–278, 2016.

UNCCD. Global land outlook. Technical report, UN Convention to Combat Desertification, Bonn, Germany, 2017. URL `https://www.unccd.int/resources/publications/global-land-outlook-1st-edition`. Accessed: 2024-09-01.

J E Ungar and PK Haff. Steady state saltation in air. *Sedimentology*, 34(2):289–299, 1987.

Alexandre Valance, Keld Rømer Rasmussen, Ahmed Ould El Moctar, and Pascal Dupont. The physics of aeolian sand transport. *Comptes Rendus. Physique*, 16(1):105–117, 2015.

Marcel GA Van Der Heijden, Richard D Bardgett, and Nico M Van Straalen. The unseen majority: soil microbes as drivers of plant diversity and productivity in terrestrial ecosystems. *Ecology letters*, 11(3):296–310, 2008.

H Van Dop, FTM Nieuwstadt, and JCR Hunt. Random walk models for particle displacements in inhomogeneous unsteady turbulent flows. *The Physics of fluids*, 28(6):1639–1653, 1985.

Qiaoqiao Wang, Jianwei Gu, and Xurong Wang. The impact of sahara dust on air quality and public health in european countries. *Atmospheric Environment*, 241:117771, 2020.

Yucang Wang, Fernando Alonso-Marroquin, and William W Guo. Rolling and sliding in 3-d discrete element models. *Particuology*, 23:49–55, 2015.

Kimiaki Washino, Ei L Chan, and Toshitsugu Tanaka. Dem with attraction forces using reduced particle stiffness. *Powder Technology*, 325:202–208, 2018.

Thomas Weinhart, Anthony R Thornton, Stefan Luding, and Onno Bokhove. From discrete particles to continuum fields near a boundary. *Granular Matter*, 14:289–294, 2012.

Thomas Weinhart, Luca Orefice, Mitchel Post, Marnix P van Schrojenstein Lantman, Irana FC Denissen, Deepak R Tunuguntla, JMF Tsang, Hongyang Cheng, Mohamad Yousef Shaheen, Hao Shi, et al. Fast, flexible particle simulations—an introduction to mercurydpm. *Computer physics communications*, 249:107129, 2020.

BT Werner. Eolian dunes: computer simulations and attractor interpretation. *Geology*, 23(12):1107–1110, 1995.

Bruce R White. Soil transport by winds on mars. *Journal of Geophysical Research: Solid Earth*, 84(B9):4643–4651, 1979.

Bruce R White and Jan C Schulz. Magnus effect in saltation. *Journal of Fluid Mechanics*, 81(3):497–512, 1977.

John D Wilson and Brian L Sawford. Review of lagrangian stochastic models for trajectories in the turbulent atmosphere. *Boundary-layer meteorology*, 78:191–210, 1996.

Anthony Chi-Ying Wong. Characterisation of the flowability of glass beads by bulk densities ratio. *Chemical Engineering Science*, 55(18):3855–3859, 2000.

Wei Wu, Ping Yan, Yong Wang, Miao Dong, Xiaonan Meng, and Xinran Ji. Wind tunnel experiments on dust emissions from different landform types. *Journal of Arid Land*, 10:548–560, 2018.

Hezi Yizhaq, Yosef Ashkenazy, and Haim Tsoar. Sand dune dynamics and climate change: A modeling approach. *Journal of Geophysical Research: Earth Surface*, 114(F1), 2009.

Hongbin Yu, Qian Tan, Mian Chin, Lorraine A Remer, Ralph A Kahn, Huisheng Bian, Dongchul Kim, Zhibo Zhang, Tianle Yuan, Ali H Omar, et al. Estimates of african dust deposition along the trans-atlantic transit using the decadelong record of aerosol measurements from caliop, modis, misr, and iasi. *Journal of Geophysical Research: Atmospheres*, 124(14): 7975–7996, 2019.

Charles S Zender, Huisheng Bian, and David Newman. Mineral dust entrainment and deposition (dead) model: Description and 1990s dust climatology. *Journal of Geophysical Research: Atmospheres*, 108(D14), 2003.

Jie Zhang, Zhenjiao Teng, Ning Huang, Lei Guo, and Yaping Shao. Surface renewal as a significant mechanism for dust emission. *Atmospheric Chemistry and Physics*, 16(24):15517–15528, 2016.

Jie Zhang, Guang Li, Li Shi, Ning Huang, and Yaping Shao. Impact of turbulence on aeolian particle entrainment: results from wind-tunnel experiments. *Atmospheric Chemistry and Physics*, 22(14):9525–9535, 2022.

Anatolii D Zimon. *Adhesion of dust and powder*. Springer Science & Business Media, 2012.

Xiaofeng Zuo, Chunlai Zhang, Xiaoyu Zhang, Rende Wang, Jiaqi Zhao, and Wenping Li. Wind tunnel simulation of wind erosion and dust emission processes, and the influences of soil texture. *International Soil and Water Conservation Research*, 12(2):455–466, 2024.

Eidesstattliche Erklärung

“Hiermit versichere ich an Eides statt, dass ich die vorliegende Dissertation selbstständig und ohne die Benutzung anderer als der angegebenen Hilfsmittel und Literatur angefertigt habe. Alle Stellen, die wörtlich oder sinngemäß aus veröffentlichten und nicht veröffentlichten Werken dem Wortlaut oder dem Sinn nach entnommen wurden, sind als solche kenntlich gemacht. Ich versichere an Eides statt, dass diese Dissertation noch keiner anderen Fakultät oder Universität zur Prüfung vorgelegen hat; dass sie - abgesehen von unten angegebenen Teilpublikationen und eingebundenen Artikeln und Manuskripten - noch nicht veröffentlicht worden ist sowie, dass ich eine Veröffentlichung der Dissertation vor Abschluss der Promotion nicht ohne Genehmigung des Promotionsausschusses vornehmen werde. Die Bestimmungen dieser Ordnung sind mir bekannt. Darüber hinaus erkläre ich hiermit, dass ich die Ordnung zur Sicherung guter wissenschaftlicher Praxis und zum Umgang mit wissenschaftlichem Fehlverhalten der Universität zu Köln gelesen und sie bei der Durchführung der Dissertation zugrundeliegenden Arbeiten und der schriftlich verfassten Dissertation beachtet habe und verpflichte mich hiermit, die dort genannten Vorgaben bei allen wissenschaftlichen Tätigkeiten zu beachten und umzusetzen. Ich versichere, dass die eingereichte elektronische Fassung der eingereichten Druckfassung vollständig entspricht.”

Köln, 02. September 2024
Sandesh Haleangady Kamath

Acknowledgements

I would like to express my heartfelt gratitude to Dr. Eric Parteli for providing me with the opportunity to work in the field of sediment transport. This thesis has taken shape under your expert guidance, and your curiosity and passion for science has profoundly influenced the researcher I am today. I am also deeply thankful to Prof. Dr. Yaping Shao, whose extensive expertise in Aeolian processes helped shape the problem statement for this work and resolve the key aspects of the model. Thank you both for welcoming me into your research groups at the University of Cologne and the University of Duisburg-Essen.

I am grateful to Prof. Dr. Gerhard Wurm for serving on my doctoral committee and for your valuable insights throughout this journey. A special thanks to Prof. Dr. Bülent Tezkan and Dr. Christian Wegener for joining my defense committee on such short notice. I also extend my appreciation to Prof. Dr. Roel Neggers and Dr. Jan Chylik, whose expertise in *Atmospheric Boundary Layer* theory helped me grasp key aspects of turbulence research.

I sincerely thank the German Research Foundation (DFG) for funding this project through grant 348617785, as well as the HPC facilities at the University of Cologne (CHEOPS) and the University of Duisburg (magnitUDE) for the essential computational support. I am also grateful to the Graduate School at Cologne (GSGS), led by Dr. Karin Boessenkool, for their continuous support throughout my doctoral studies.

A warm thanks to my ex-colleagues at the University of Cologne — Mateusz Kryger, Dr. Qian Xia, Dr. Cong Jiang, and Dr. Xin Yin for the stimulating discussions on our research and everything in between. I am especially grateful to Dr. Jasper Kok for generously providing his COMSALT code, which was invaluable during the early stages of developing this numerical tool. My sincere thanks also go to Dr. Thomas Pähtz for the enriching interactions through our collaborative work which was a great learning experience. I thoroughly enjoyed my time in Duisburg and the insightful discussions with students there.

I would also like to acknowledge my former mentors at the National Chemical Laboratory (NCL Pune, India) — Dr. Ashish V. Orpe, Dr. Pankaj Doshi, and Amit Kunte, who introduced me to the world of Discrete Element Method (DEM) and set the foundation for my journey into computational modeling.

I am eternally grateful to my parents and my brother, who have been my constant anchors throughout life. I also extend my gratitude to my parents-in-law, whose unwavering support carried me through the final years of my PhD. My heartfelt thanks go to all my friends, especially Vishnu, Hans and Birgit, who made my time in Germany all the more memorable.

I would also like to take a moment to thank all the teachers I have had the privilege of learning from throughout my life. A special acknowledgement to Sadhguru, whose wisdom has been a guiding force, and for his global efforts in raising awareness on soil degradation through the Save Soil movement.

Finally, none of this would have been possible without my wife, Mahalakshmi Hari. Thank you for your boundless love, patience and unwavering support ever since the day we began our journey together. Your resilience, intellect, and kindness have shaped me in more ways than I can express, making me who I am today. I love you, from the depths of my heart — to infinity and beyond!

***